Nonlinear Two-Line Shoreline Model with Refraction

by

Satoshi Nagashima

and

Robert A. Dalrymple

RESEARCH REPORT NO. CACR-97-07

August, 1997

Center for Applied Coastal Research
Ocean Engineering Laboratory
University of Delaware
Newark, DE 19716
U.S.A.

ACKNOWLEDGMENTS

This work was originally submitted by Satoshi Nagashima in the Fall of 1997 as a thesis to the Faculty of the University of Delaware in partial fulfillment of the requirements for the degree of Master of Civil Engineering.

This work was sponsored by Kajima Corporation during his stay at the University of Delaware.

TABLE OF CONTENTS

LIST OF FIGURES

LIST OF TABLES

ABSTRACT

The nonlinear two-line shoreline model has been developed to expand the linear two-line shoreline model developed by Dalrymple (1997). The purpose of this study is to explain the migration of sand waves that have been observed in the field. To this date, there is no satisfactory physical explanation of this phenomenon. The above two-line models account for the effects of wave refraction, which was not considered in the original two-line model developed by Bakker (1968b). In the nonlinear model, the wave focusing effect will also be considered under the assumption of straight wave rays.

Extensive physical model tests were performed in a spiral wave basin to verify numerical results. Test results are included for the case of a single beach fill and three beach fills. By conducting bathymetry surveys of complete sets of three dimensional data for both cases were acquired. In order to measure the rate of longshore transport, the single groin method was used to trap all sediment moving along the shoreline. The wave period, the root-mean-square wave height, and the incident wave angle with respect to the radial direction were measured using two wave gauges.

Numerical results for the nonlinear model were verified using the experimental results, the linear model, and field observation data. For each comparison, a variety of sensitivity analyses were examined. These included using a range of incident angles, different inshore and offshore depths, different beach slopes, and

different types of initial contours. For the initial contours in this study, the solitary sand wave, a single trapezoidal beach fill, and periodic beach were adopted. Finally, the nonlinear model was applied to the simulation of the case of sand hump migration at San Onofre, California.

Chapter 1

INTRODUCTION

The shoreline represents the boundary between the ocean and land, and it is changing position constantly. Considerable erosion due to both the long term effects of normal wave conditions and short term effects, such as hurricanes and storms, occasionally threatens people's lives along the coast, whereas accretion sometimes causes either functional problems for coastal structures or navigational problems due to the change of the water depth. Frequently, the effects from artificial modifications to the shore provide unexpected erosion or accretion, altering people's property. It is extremely important to predict shoreline changes beforehand in order to avoid both physical and economical damage. For instance, the estimation of the lifetime of the project is critical for beach nourishment. In the past, there have been numerous studies of this issue; however, due to difficulties of predicting the sediment dynamics in the surf zone,the shoreline prediction models lag far behind the models for wave propagation problems.

The term "sand wave" has been used to describe a changing shoreline with wave-like motions usually resulting from some perturbations in the longshore direction. Any unbalance of profiles in both cross-shore and longshore directions will cause sand movement to return them to the equilibrium profile. One might observe wave-like motions of sand during these processes. In this chapter, some

observations of sand waves in the field will be introduced. Then, existing contour models will be briefly reviewed. Finally, the object of this study will be summarized.

1.1 Previous Related Studies

1.1.1 Observation of Sand Waves

Some observations of migrating sand waves have been reported. There are two types of sand waves: persistent waves and a single wave. Persistent sand waves have been observed at very long beaches. They are possibly caused by a periodic sand supply, like periodic sand bypassing. The other type of sand waves can be seen at artificial shoreline modifications such as beach fills.

Bruun (1954) observed large undulations in the shoreline position migrating along the shore in the direction of the littoral drift on the Danish North Sea coast. Wavelengths of those sand waves were between 0.5-2 km and wave heights were 60-80 m. Bakker (1968a) observed a kind of sand wave with a period of about 60 years that seemed to be migrating with a velocity of about 1/6 to 1/3 km/year. Verhagen (1989) defined sand waves as longshore wave-like movements of shoreline measured in a horizontal plane. He found that they had a celerity of 50-200 m/yr, a period of 50-150 years, and an amplitude of 30-500 m along the Dutch shoreline. There is one more recent example for this type of sand waves in Southhampton Beach, Long Island, New York. Eleven longshore sand waves have been identified along Southhampton Beach and have an average length of 0.75 km and an amplitude of 40 m (Thevenot and Kraus, 1995).

On the other hand, there is some evidence of cases of accretion and erosion waves. For instance, the removal of the laydown pad at the San Onofre Nuclear

Generating Station in Southern California in late December 1984 gave coastal engineers an opportunity to investigate a massive sediment injection on a smooth shoreline (Grove and Sonu and Dykstra, 1987). They observed erosional and accretional changes of profiles at some fixed locations at downcoast. They noted that the changes in the profiles seemed to strongly depend on the distance from the site. Furthermore, they stated that the speed of migration of the crest of the hump was extremely slow, averaging only about 2 m/day or less than a kilometer a year, and the decay of the size of the crest was extremely rapid, diminishing by one half every 300 days. Inman (1987) found the diffusion coefficient for the accretion wave at San Onofre to be 2 $\times 10^{-4} m^2/\text{sec}$, and velocities to range from 0.6 to 1.1 km/yr. To this data, no satisfactory explanation for the propagation of sand waves exists.

1.1.2 Existing Contour Models

There are two general types of shoreline models that exist. Contour model follow the movement of shoreline contours, and grid models examine the change of bathymetry in various types of grids. The one-line model is the first and simplest contour model and was presented by Pelnard-Considere (1956). It is also most widely used for practical beach projects since it is relatively easy to handle. The one-line model is a simple diffusion equation which describes the time history of the shoreline position along a coast:

$$\frac{\partial y}{\partial t} = G\frac{\partial^2 y}{\partial x^2}$$

where G is the shoreline diffusivity, y is the shoreline position in the offshore direction measured from the instant baseline, x is the longshore position and t is time.

Solutions to the diffusion equation are both mathematically and physically well-established, so that after providing appropriate initial conditions, boundary conditions and some physical parameters, it is easily solved either numerically or analytically. For instance, Le Mehaute and Brebner (1961, cited in Dean and Dalrymple, 1997) obtained periodical solutions with the initial shoreline, $y(x,0) = B\cos\lambda x$. Here λ is the longshore wave number of sand waves and B is the initial amplitude of the sand waves. Assuming the periodic solution in x to be:

$$y(x,t) = f(t)\cos\lambda x,$$

They obtained the following solution:

$$y(x,t) = Be^{-G\lambda^2 t}\cos\lambda x$$

This solution, which has a periodic shape in the longshore direction, however, just represents a temporally decaying solution.

One of the other solutions was a progressive wave solution examined by Bakker (1968a). His solution was:

$$y(x,t) = Ae^{-\sqrt{\frac{\sigma}{2G}}x}\cos(\sqrt{\frac{\sigma}{2G}}x - \sigma t)$$

where σ is the sand wave frequency and A is the initial amplitude of the sand waves. This solution describes propagating waves with decaying amplitude. Unfortunately, the decay of the waves is extremely rapid compared to their very slow propagation. The waves almost disappear after propagating approximately one wavelength. Therefore, this solution also can not explain migrating sand waves.

The one-line model describes only one of the contours and assumes uniform equilibrium profiles along the coast. Several additional assumptions were made in the model such as no current, constant wave direction, small angles of wave incidence, and a linear relationship between the angle of wave direction and the alongshore transport rate.

The two-line shoreline model was originally introduced by Bakker (1968b) to overcome some weak points of the one-line model. One of the assumptions for the one-line model was a uniform equilibrium profile along the coast. In other words, Pelnard-Considere assumed that subaqueous profiles always remain in their equilibrium state. Therefore, he only had to follow the one line, the shoreline, and still be able to predict the position of all others. However, in practice, profiles are not always uniform along the coast, especially in the vicinity of coastal structures such as groins, jetties and breakwaters. Beaches upcoast and downcoast usually have different profiles, that is to say, steeper profiles upcoast and milder profiles downcoast. Most of sediments ideally trapped by groins are accumulated on the upcoast side of the groin, while most of the erosion occurs on the downcoast side of the groin. The assumption of equilibrium profiles gives us a progression of

the shoreline at upcoast locations and a recession at downcoast locations. The contours of these profiles are assumed parallel to each other in the one-line model; however, in the real world, the bathymetries do not change at offshore locations beyond certain depth. This depth is usually called the depth of closure. As a result, the upcoast profiles develop a steeper slope than their natural equilibrium and the downcoast profiles develop flatter bathymetries. This kind of bathymetry can be generally found around coastal structures and is not explained by the one-line contour model due to the assumption of parallel contours. Further, other hydrodynamic system can cause even more complicated bathymetry.

Bakker's two-line model improved some of the one-line model's limitations, introducing two contour lines at the inshore and offshore rather than just one contour line and allowing his model to take into account cross-shore sediment transport between the two contours. He defined the depths of the two contours as D_1 and $D_1 + D_2$, respectively, and made two sections. Due to the cross-shore sediment transport between the two contours, the two mass conservation equations from each section were coupled together. Taking the x-axis as the shoreline, positive in the downstream direction, and with the positive y-axis in the offshore direction, he defined the distance of the inshore and offshore contours from an arbitrary baseline as y_1 and y_2' , respectively.

These are Bakker's governing equations of two-line model:

$$D_1 \frac{\partial y_1}{\partial t} = -q_y - \frac{\partial Q_1}{\partial x}$$
$$D_2 \frac{\partial y_2}{\partial t} = q_y - \frac{\partial Q_2}{\partial x}$$

where Q_1 and Q_2 are the longshore transport at each section and q_y is the cross-shore transport. Notice that y_2 in these equations is different from y_2'. The two are related by $y_2 = y_2' - w$ where w is the horizontal distance between the two depth positions D_1 and $D_1 + D_2$ at equilibrium.

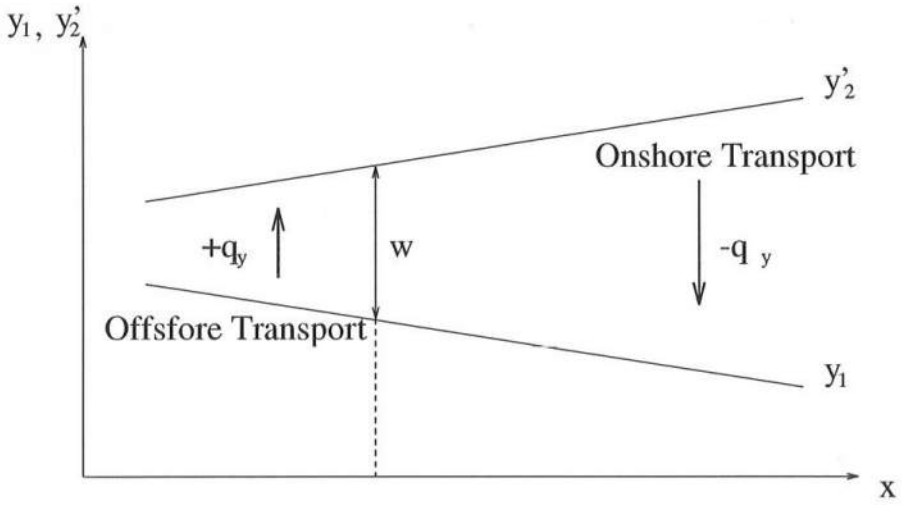

Figure 1.1: Definitions of Bakker's model

In addition to these equations, an equation for the cross-shore transport, q_y is needed. The basic idea for Bakker's approach is that any perturbation in the spacing between the two contour lines from their equilibrium separation, w, is countered by a tendency to recover the equilibrium spacing. Bakker also assumed that cross-shore transport was linearly related to the difference between the spacing of two contours and the equilibrium distance by the dimensional transport constant C_y, which is specified at each site.

$$q_y = C_y(y_1 - y_2' + w) \tag{1.1}$$

Offshore transport occurs if $y_1 - y_2' < w$ and onshore transport occurs if $y_1 - y_2' > w$.

Next, longshore transport can be written as follows:

$$\begin{aligned} Q_1 &= Q_{1_o} - q_1 \frac{\partial y_1}{\partial x} \\ Q_2 &= Q_{2_o} - q_2 \frac{\partial y_2}{\partial x} \end{aligned}$$

where Q_{1_o} and Q_{2_o} are background transport rates for shorelines where the angles of the shoreline normal with respect to y-axis, γ_1 and γ_2, are zero, and the second term represents the transport induced by the alongshore slope of the shoreline assuming a linear relation between them, as assumed by Pelnard-Considere. The terms q_1 and q_2 are linear constants which are determined by the site or field conditions.

Substituting Q_1, Q_2 and q_y into the original governing equations, he obtained:

$$\begin{aligned} D_1 \frac{\partial y_1}{\partial t} &= -C_y(y_1 - y_2) + q_1 \frac{\partial^2 y_1}{\partial x^2} \\ D_2 \frac{\partial y_2}{\partial t} &= C_y(y_1 - y_2) + q_2 \frac{\partial^2 y_2}{\partial x^2} \end{aligned}$$

Bakker introduced new variables as follows:

$$\begin{aligned} y &= (D_1 y_1 + D_2 y_2)/D \\ y_e &= (y_1 - y_2) \exp\left(\frac{C_y D t}{D_1 D_2}\right) \end{aligned}$$

where $D = D_1 + D_2$.

Assuming further that $\frac{q_1}{D_1} = \frac{q_2}{D_2}$, which means that contours with the same curvature will be filled at the same rate and the relative profiles will not change, he finally obtained these two simple diffusion equations:

$$\begin{aligned} \frac{\partial y}{\partial t} &= G \frac{\partial^2 y}{\partial x^2} \\ \frac{\partial y_e}{\partial t} &= G \frac{\partial^2 y_e}{\partial x^2} \end{aligned}$$

with $G = (q_1 + q_2)/D$.

Bakker (1968b) solved these equations numerically with boundary conditions for a single groin and for several groins. Hulsbergen, Bakker and Bochove

(1976) verified Bakker's results by conducting a laboratory experiment, and obtaining quite good agreement under a well defined wave field. On the other hand, for some cases which had more complicated wave fields, Bakker's model didn't show good results. They reported that it would be neccesary to include the effects of refraction, diffraction and rip-currents in order to improve the applicability of the model.

1.2 Object of the Present Study

In the nearshore zone, effects of bathymetry on wave fields can be tremendous and can cause extremely complicated sediment dynamics. One of the physical phenomena, which can introduce changes in wave fields, is wave refraction. Since longshore transport rates are strongly related to angles of incident waves, wave refraction can cause dramatic changes in sediment dynamics.

In this study, effects of wave refractions will be added to Bakker's two-line shoreline model. This study consists of two parts : a laboratory experiment and a numerical analysis. In Chapter 2 the development of the theory of both the linear and the nonlinear two-line model with refraction will be explained. Procedures and results of the experiment will be discussed in Chapter 3. The goal of the experiment was to determine if the numerical model was giving reasonable results. Since there are not so many sources of field data regarding sand waves, the laboratory experiment was very important. Then in Chapter 4 results from the numerical model will be examined by using the experimental data and some field data.

To summarize, the main goal of this study is to develop a nonlinear two-line shoreline model that has more applicability to general situations with fewer assumptions and to verify its results by conducting a laboratory experiment and examining some recent field data.

Chapter 2

DEVELOPMENT OF THE TWO-LINE MODEL WITH REFRACTION

The two-line shoreline model developed by Bakker does not account for any water wave refraction; however one might argue that wave refraction can change wave directions dramatically between two contours. In this chapter the theories of both the linear and the nonlinear two-line shoreline model with refraction are explained and the dimensional analysis of the linear model is performed to verify the importance of each parameter.

2.1 Definition of the Geometry

Figure 2.1 shows the definition of the geometry in this model. One can choose two arbitrary depths D_1 and D_2 so that y_1 and y_2 contours can be defined which correspond to D_1 and $D_1 + D_2$, respectively by using the concept of equilibrium profiles. Figure 2.2 shows the definition of the angles used for the theory. As in Bakker's model the (x, y) rectangular coordinate system is adopted. δ is the angle of wave incidence at offshore with respect to the y axis, and γ is the angle of the shoreline normal with respect to y-axis. Consequently, $\delta - \gamma$ represents the wave angle with respect to the shoreline normal.

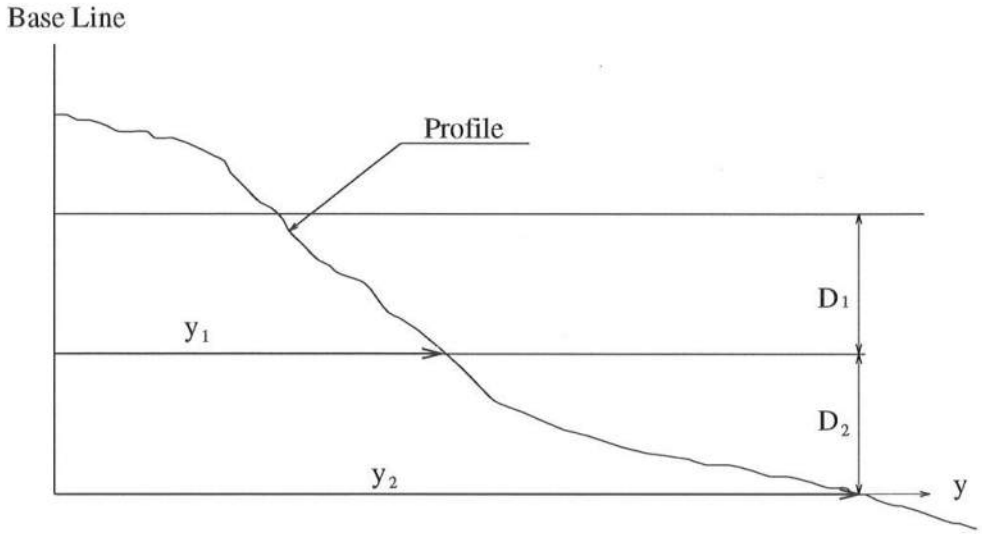

Figure 2.1: Definition of profile parameters

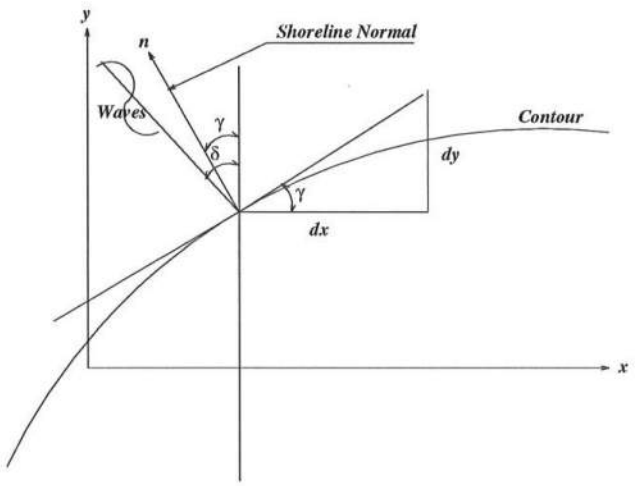

Figure 2.2: Definition of angles, plan view

Let's define the wave number at an offshore location as k_o and the wave numbers at the y_2 and y_1 contour are k_2 and k_1, respectively. Also, define the offshore angle of wave incidence with respect to the y-axis as δ_o, that at the y_2 contour as μ_2 and that at the y_1 contour as μ_1, as shown in Figure 2.3. Assuming that the y_1 and y_2 contours are locally straight, one can apply Snell's law across the y_1 and y_2 contours:

$$k_2 \sin(\mu_2 - \gamma_1) = k_1 \sin(\mu_1 - \gamma_1) \tag{2.1}$$

$$k_o \sin(\delta_o - \gamma_2) = k_2 \sin(\mu_2 - \gamma_2) \tag{2.2}$$

These equations can be interpreted using the refraction diagram shown in Figure 2.4. δ_1 is the wave angle at the y_2 contour which becomes μ_1 as the wave passes over the y_1 contour. In Figure 2.3 $\delta_1(x)$ is written as $\mu_2(x-\Delta\xi)$. Assuming that the only known wave angle is δ_o and it is uniform in the longshore direction, one can obtain $\mu_2(x)$ using Snell's law. However, it is still necessary to find the spatial lag $\Delta\xi$ in the spatial argument of μ_2 to obtain $\mu_1(x)$ from $\mu_2(x)$. In other words, the angles obtained by Snell's law along the same wave ray both at y_1 and at y_2 usually do not have same spatial argument due to their oblique incidence. Therefore, it is important to take into account this spatial lag.

Using trigonometry, γ_2 can be expressed as follows:

$$\tan\gamma_2 = \frac{dy}{dx}$$

$$\sin\gamma_2(x) = \frac{dy}{\sqrt{dx^2+dy^2}} = \frac{\frac{\partial y_2}{\partial x}}{\sqrt{1+(\frac{\partial y_2}{\partial x})^2}}$$

or,

$$\gamma_2(x) = \arcsin\left(\frac{\frac{\partial y_2}{\partial x}}{\sqrt{1+(\frac{\partial y_2}{\partial x})^2}}\right) \tag{2.3}$$

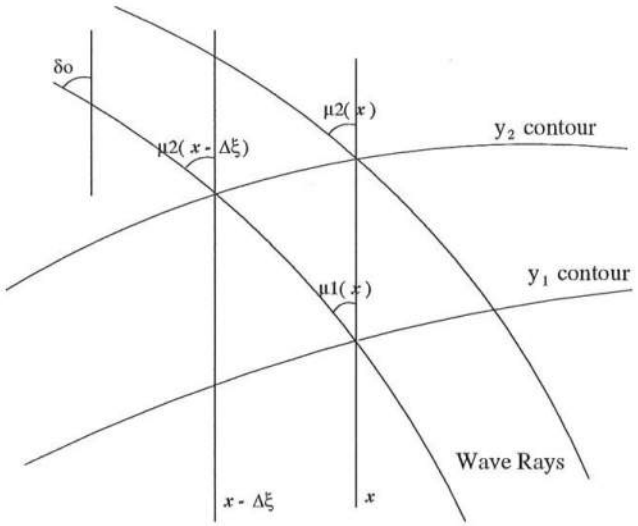

Figure 2.3: Wave rays and angles

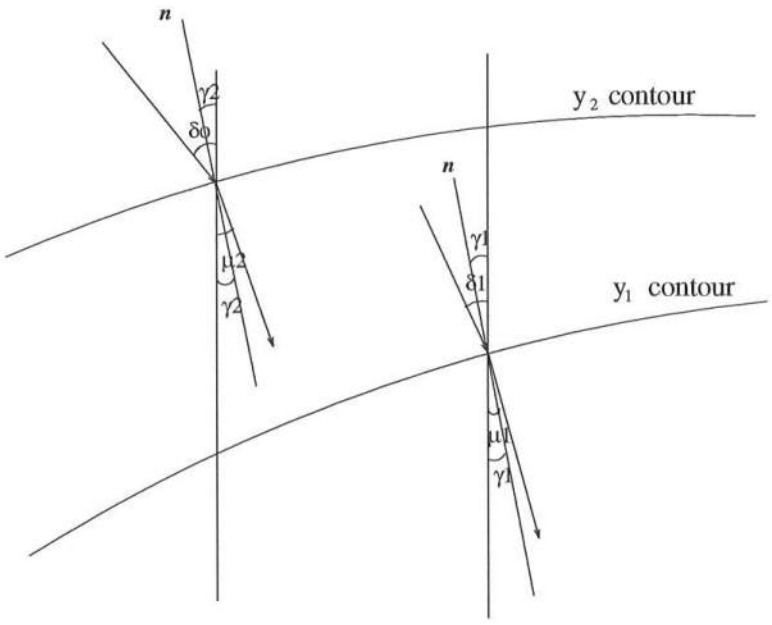

Figure 2.4: Refraction diagram

Likewise, for the y_1 contour

$$\gamma_1(x) = \arcsin\left(\frac{\frac{\partial y_1}{\partial x}}{\sqrt{1+(\frac{\partial y_1}{\partial x})^2}}\right) \tag{2.4}$$

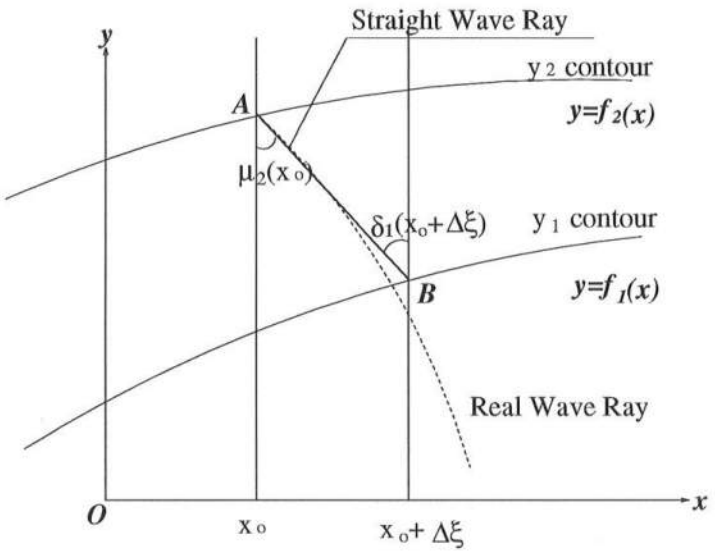

Figure 2.5: Straight wave ray assumption

As mentioned before, it is very important to determine the relationship between μ_2 and μ_1. However, the geometries between two contours are unfortunately usually unknown or only partially known. Therefore, assuming a very mild change in the bathymetry, one might assume a straight wave ray from the y_2 to the y_1 contour. By making this assumption, one can derive the next relation.

$$\delta_1(x_o + \Delta\xi) = \mu_2(x_o)$$

Since the waves are traveling obliquely, there is a spatial lag $\Delta\xi$ in the longshore direction. So, the next question is how to obtain the $\Delta\xi$. First, the (x, y) rectangular coordinate system is adopted with the instantaneous origin O as

shown in Figure 2.5. Next, let A be the intersection of the ray with the y_2 contour and let B be the intersection of the ray with the y_1 contour. Also, suppose the two contours are expressed as the functions: $y_1 = f_1(x)$, $y_2 = f_2(x)$. The x values at A and B are x_o and $x_o + \Delta\xi$, respectively. The angle of the wave ray line passing through both A and B with respect to the y axis is $\mu_2(x_o)$.

From the geometry,

$$\frac{dx}{dy} = -\tan \mu_2(x_o)$$

Integrating this equation with respect to y,

$$x = -\tan \mu_2(x_o)y + C$$

Using one known point, A $(x_o, f_2(x_o))$, evaluate the real constant C:

$$C = x_o + \tan \mu_2(x_o) f_2(x_o)$$

Back substituting this into the original equation and rearranging, one can get Eq. 2.5. This is the equation for the straight wave ray.

$$x = \tan \mu_2(x_o)\{f_2(x_o) - y\} + x_o \tag{2.5}$$

Finally, substituting the values at $B(x_o + \Delta\xi\ ,\ f_1(x_o + \Delta\xi))$ into Eq. 2.5, the next implicit equation for $\Delta\xi$ can be obtained.

$$\Delta\xi = \tan \mu_2(x_o)\{f_2(x_o) - f_1(x_o + \Delta\xi)\} \tag{2.6}$$

To solve this implicit equation numerically, an iterative technique such as Newton-Raphson technique can be used, as long as $f_1'(x)$ exists.

After obtaining the relationship between μ_2 and δ_1, the implicit relationship between μ_1 and μ_2 will be established by applying Snell's law from y_2 contour to y_1 contour as shown in Eq. 2.1.

2.2 Cross-shore Sediment Transport

The following cross-shore sediment transport equation was first proposed by Moore (1982) and later modified by Kriebel (1983), and Kriebel and Dean (1985), which is based on the disequilibrium of the energy dissipation within the surf zone:

$$Q_y = K(D - D_*)$$

where Q_y is the cross-shore sediment transport, K is the transport rate coefficient, D is the actual energy dissipation per unit volume, and D_* is the equilibrium energy dissipation. This equation implies that, if $D > D_*$, then destructive forces act more strongly than equilibrium forces so that erosion occurs and sediment moves offshore. Positive Q_y means offshore transport, while negative Q_y is onshore transport. D can be calculated by expressing the energy dissipated by the control volume, which can be taken over the depth with unit width in the longshore direction and cross-shore distance Δx, as the net energy flux from the control volume:

$$D = \frac{\mathcal{F}(x + \Delta x) - \mathcal{F}(x)}{\bar{h}\Delta x}$$

where $\bar{h}$ is the average water depth over the distance Δx. Taking a limit of this equation, one can obtain:

$$D = \frac{1}{\bar{h}} \frac{\partial \mathcal{F}}{\partial x}$$

Using linear wave theory one can obtain:

$$D = \frac{5}{16} \gamma \kappa^2 g^{\frac{1}{2}} \bar{h}^{\frac{1}{2}} \frac{\partial h}{\partial x}$$

where γ is the specific gravity of water, κ is the dimensionless breaking index, g is the acceleration of gravity and h is the depth of water. To calculate D_*, the equilibrium energy dissipation, one can use the equilibrium beach slope for $\frac{\partial h}{\partial x}$.

Moore (1982) determined the value for K empirically by performing curve fitting between a numerical equilibrium beach profile model based on this equation and the results from both large scale laboratory tests and field data. He found the best-fit value for K would be $2.2 \times 10^{-6} m^4/N$.

2.3 Longshore Sediment Transport

The waves with incident angles different from zero can cause longshore sediment transport due to the longshore component of their energy flux. The energy flux per unit length in the longshore direction can be written as Eq. 2.7 using geometric relations (Dean and Dalrymple, 1997) .

$$P_\ell = (EC_g)_b \sin\theta_b \cos\theta_b = \frac{1}{16}\rho g H_b^2 C_g \sin 2\theta_b \tag{2.7}$$

Here $(EC_g)_b$ is the energy flux passing between two wave rays that have a unit spacing at the breakerline, H_b is the breaking wave height and θ_b is the wave incident angle at the breakerline.

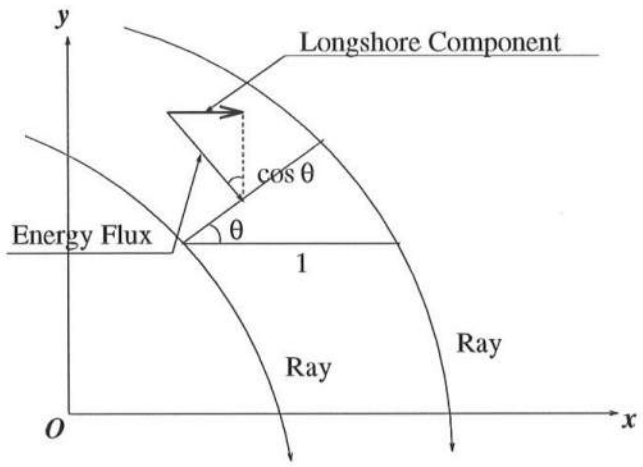

Figure 2.6: Longshore component of energy flux

In a similar manner, the longshore sediment transport rate can be written as follows:

$$Q = \frac{\mathcal{K} P_\ell}{\rho(s-1)g(1-p)} \tag{2.8}$$

where $p\,(\sim 0.3\ or\ 0.4)$ is the porosity of the sediment, $s\,(\sim 2.65)$ is the specific gravity of sand, and $\mathcal{K}$ is defined as the longshore transport coefficient ranging from 0.2 (Kraus, 1980) to 2.2 (Caldwell, 1956, cited in Dean and Dalrymple, 1997). The determinations of the values for $\mathcal{K}$ were all empirical. Further the shallow water approximation is taken as $C_g = \sqrt{gh_b}$ and the relationship between the breaking wave height and the water depth at the breakerline is assumed to be $H_b = \kappa h_b$. Here h_b is the water depth at the breakerline and κ is the breaking index usually taken as 0.78. Substituting Eq. 2.7 into Eq. 2.8, one can obtain a new expression for Q as in Eq. 2.9.

$$Q = \frac{\mathcal{K}\sqrt{g/\kappa} H_b^{2.5}}{16(s-1)(1-p)} \sin 2\theta_b \tag{2.9}$$

Letting the coefficient of $\sin 2\theta_b$ in Eq. 2.9 be C_q and introducing angles δ and γ from Section 2.1, Q may be written as,

$$Q = C_q \sin 2(\delta - \gamma) \tag{2.10}$$

with

$$C_q = \frac{\mathcal{K}\sqrt{g/\kappa} H_b^{2.5}}{16(s-1)(1-p)}$$

where δ is once again the wave angle with respect to the y-axis and γ is the angle between the shoreline normal and the y-axis, which is same as the slope of the shoreline.

2.3.1 Conservation of Mass

In this theory the conservation of sand was applied to two sections, each with a longshore width of Δx, and they are encompassed by the two contours and the shoreline. Figure 2.7 shows idealized control boxes and the instant sediment flows. The next set of equations represents the conservation of sand for the control boxes.

$$\begin{aligned} \Delta x D_1 \frac{\partial y_1}{\partial t} &= Q_1 - (Q_1 + \frac{\partial Q_1}{\partial x}\Delta x) - Q_y \Delta x \\ \Delta x D_2 \frac{\partial y_2}{\partial t} &= Q_2 - (Q_2 + \frac{\partial Q_2}{\partial x}\Delta x) + Q_y \Delta x \end{aligned} \tag{2.11}$$

Rearranging Eq. 2.11,

$$\begin{aligned} D_1 \frac{\partial y_1}{\partial t} &= -Q_y - \frac{\partial Q_1}{\partial x} \\ D_2 \frac{\partial y_2}{\partial t} &= Q_y - \frac{\partial Q_2}{\partial x} \end{aligned} \tag{2.12}$$

where

$$\begin{aligned} Q_y &= K(D - D_*) \\ Q_1 &= C_q \sin 2(\mu_1 - \gamma_1) \\ Q_2 &= C_q \sin 2(\mu_2 - \gamma_2) \end{aligned}$$

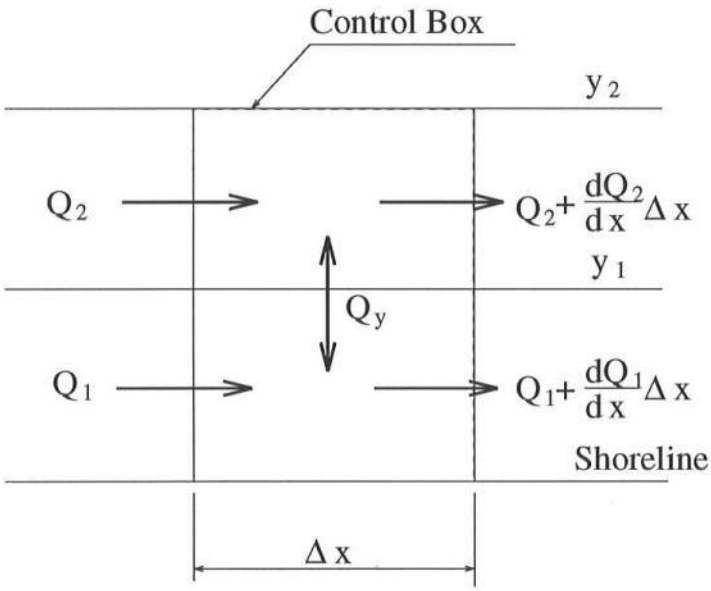

Figure 2.7: Planform view of idealized control boxes and the instantaneous sediment flows

2.3.2 Linearized Model

Dalrymple (1997) linearized these equations by assuming that both the incident wave angles and the slope of the shoreline were sufficiently small. His linearized two-line model used Bakker's expression for the cross-shore sediment transport:

$$q_y = C_y(w - y_2' + y_1)$$

Again, q_y is positive if $y_2' - y_1 < w$ which means the contour spacing is smaller than its equilibrium spacing, and offshore transport will act to return the profile to equilibrium. Here the definitions of the shoreline positions are shown in Figure 2.8 with $y_2 = y_2' - w$.

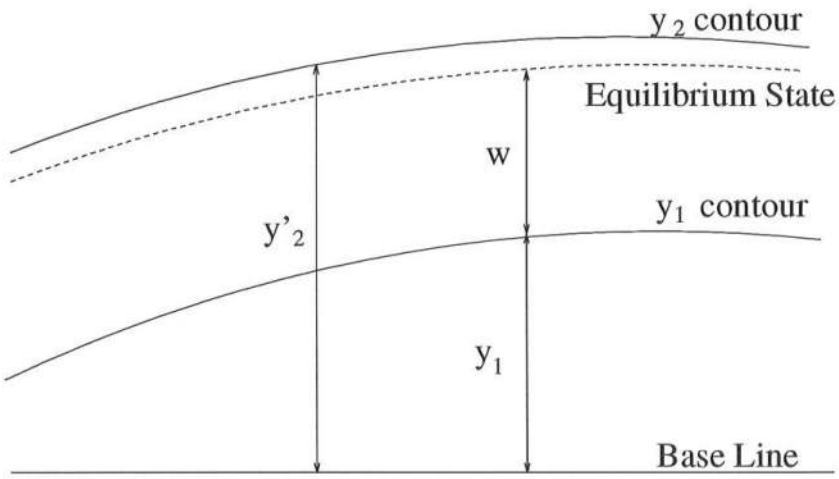

Figure 2.8: Definition of the shoreline positions

Dalrymple expanded Eq. 2.2 using the trigonometric relationship,

$$k_o \sin\delta_o \cos\gamma_2 - k_o \cos\delta_o \sin\gamma_2 = k_2 \sin\mu_2 \cos\gamma_2 - k_2 \cos\mu_2 \sin\gamma_2$$

He first derived the explicit expression for μ_2 using these assumptions. Approximating the trigonometric functions $\sin\delta$ as $\cos\delta$ to δ and 1, respectively, the preceding equation was rewritten.

$$k_o\delta_o - k_o\gamma_2 = k_2\mu_2 - k_2\gamma_2$$

Since, γ_2 can be also approximated as $\gamma_2 \approx \frac{\partial y_2'}{\partial x}$, the above equation can be written as the following equation for μ_2.

$$\mu_2 = \frac{k_o}{k_2}\delta_o + (1 - \frac{k_o}{k_2})\frac{\partial y_2'}{\partial x} \tag{2.13}$$

Dalrymple also assumed straight wave rays from the y_2 contour to the y_1 contour which were spaced $y_2' - y_1$ apart. Then he expressed the relationship between δ_1 and μ_2 as:

$$\delta_1(x_1) = \mu_2(x_1 - \Delta\xi) \tag{2.14}$$

where

$$x_1 = x_o + \Delta\xi$$

$$\Delta\xi = (y_2' - y_1)\sin\mu_2(x_o) = (w + y_2 - y_1)\sin\mu_2(x_o) \approx w\mu_2(x_o)$$

Expanding $\mu_2(x_1 - \Delta\xi)$ about $x = x_1$ using a Taylor series:

$$\begin{aligned} \delta_1(x_1) &= \mu_2(x_1 - \Delta\xi) = \mu_2(x_1) - \left.\frac{\partial\mu_2}{\partial x}\right|_{x_1} \Delta\xi + \cdots \\ &\approx \mu_2(x_1) - w\mu_2(x_o)\left.\frac{\partial\mu_2}{\partial x}\right|_{x_1} \end{aligned} \tag{2.15}$$

On the other hand, expanding $\mu_2(x_o + \Delta\xi)$ about $x = x_o$,

$$\mu_2(x_1) = \mu_2(x_o + \Delta\xi) = \mu_2(x_o) + \left.\frac{\partial \mu_2}{\partial x}\right|_{x_o} \Delta\xi + \cdots$$

Solving for $\mu_2(x_o)$,

$$\mu_2(x_o) \approx \mu_2(x_1) - \left.\frac{\partial \mu_2}{\partial x}\right|_{x_o} \Delta\xi \tag{2.16}$$

At $x = x_1$ using Eq. 2.13:

$$\mu_2(x_1) = \frac{k_o}{k_2}\delta_o + (1 - \frac{k_o}{k_2}) \left.\frac{\partial y_2'}{\partial x}\right|_{x_1} \tag{2.17}$$

Taking the derivative of $\mu_2(x)$ at $x = x_1$,

$$\left.\frac{\partial \mu_2}{\partial x}\right|_{x_1} = (1 - \frac{k_o}{k_2}) \left.\frac{\partial^2 y_2'}{\partial x^2}\right|_{x_1} \tag{2.18}$$

Substitute Eq. 2.17, Eq. 2.16 and Eq. 2.18 into Eq. 2.15.

$$\begin{aligned}
\delta_1(x_1) &= \mu_2(x_1) - w\left(\mu_2(x_1) - \left.\frac{\partial \mu_2}{\partial x}\right|_{x_o} \Delta\xi\right) \left.\frac{\partial \mu_2}{\partial x}\right|_{x_1} \\
&\approx \mu_2(x_1) - w\mu_2(x_1)(1 - \frac{k_o}{k_2}) \left.\frac{\partial^2 y_2'}{\partial x^2}\right|_{x_1} \\
&\approx \mu_2(x_1) - w\left(\frac{k_o}{k_2}\delta_o + (1 - \frac{k_o}{k_2}) \left.\frac{\partial y_2'}{\partial x}\right|_{x_1}\right)(1 - \frac{k_o}{k_2}) \left.\frac{\partial^2 y_2'}{\partial x^2}\right|_{x_1}
\end{aligned}$$

From this expression Dalrymple obtained the approximated equation for δ_1, Eq. 2.19.

$$\delta_1(x) = \mu_2(x) - w\frac{k_o}{k_2}\delta_o(1 - \frac{k_o}{k_2})\frac{\partial^2 y_2'}{\partial x^2} \tag{2.19}$$

Further, he expanded the equation of Snell's law on the y_1 contour, Eq. 2.1, in the same way as that of the y_2 contour and got the next relation.

$$\mu_1 = \frac{k_2}{k_1}\mu_2 + (1 - \frac{k_2}{k_1})\gamma_1$$

This equation is valid on the same wave ray. By using Eq. 2.14, the following equation is valid at the same longshore position.

$$\mu_1 = \frac{k_2}{k_1}\delta_1 + (1 - \frac{k_2}{k_1})\gamma_1$$

Using Eq. 2.19 and Eq. 2.13 and approximating $\gamma_1 \approx \frac{\partial y_1}{\partial x}$, Dalrymple obtained the following equation for μ_1.

$$\mu_1 = \frac{k_2}{k_1}\left[\frac{k_o}{k_2}\delta_o + (1 - \frac{k_o}{k_2})\frac{\partial y_2'}{\partial x} - w\frac{k_o}{k_2}\delta_o(1 - \frac{k_o}{k_2})\frac{\partial^2 y_2'}{\partial x^2}\right] + (1 - \frac{k_2}{k_1})\frac{\partial y_1}{\partial x} \tag{2.20}$$

Moving on to longshore transport both at y_1 and at y_2, Q_2 can be approximated as follows:

$$\begin{aligned} Q_2 &= C_q \sin 2(\mu_2 - \gamma_2) \approx 2C_q(\mu_2 - \gamma_2) \\ &\approx 2C_q \left[\frac{k_o}{k_2}\delta_o + \left(1 - \frac{k_o}{k_2}\right) \frac{\partial y_2'}{\partial x} - \frac{\partial y_2'}{\partial x} \right] \\ &\approx 2C_q \frac{k_o}{k_2}\delta_o - 2C_q \frac{k_o}{k_2} \frac{\partial y_2'}{\partial x} \end{aligned}$$

Taking the derivative of this,

$$\frac{\partial Q_2}{\partial x} = -2C_q \frac{k_o}{k_2} \frac{\partial^2 y_2'}{\partial x^2} = -q_2 \frac{\partial^2 y_2'}{\partial x^2}$$

Here, Dalrymple defined:

$$q_2 \equiv 2C_q \frac{k_o}{k_2}$$

Similarly, for Q_1,

$$\begin{aligned} Q_1 &= C_q \sin 2(\mu_1 - \gamma_1) \\ &\approx 2C_q(\mu_1 - \gamma_1) \\ &\approx 2C_q \left[\frac{k_2}{k_1} \left(\frac{k_o}{k_2}\delta_o + (1 - \frac{k_o}{k_2}) \frac{\partial y_2'}{\partial x} - w \frac{k_o}{k_2}\delta_o (1 - \frac{k_o}{k_2}) \frac{\partial^2 y_2'}{\partial x^2} \right) + (1 - \frac{k_2}{k_1}) \frac{\partial y_1}{\partial x} - \frac{\partial y_1}{\partial x} \right] \end{aligned}$$

Taking the derivative of this,

$$\frac{\partial Q_1}{\partial x} \approx 2C_q \frac{k_2}{k_1}(1 - \frac{k_o}{k_2}) \frac{\partial^2 y_2'}{\partial x^2} - 2C_q w \frac{k_o}{k_1}\delta_o (1 - \frac{k_o}{k_2}) \frac{\partial^3 y_2'}{\partial x^3} - 2C_q \frac{k_2}{k_1} \frac{\partial^2 y_1}{\partial x^2}$$

Here, he defined the following terms:

$$\begin{aligned} q_1 &\equiv 2C_q \frac{k_2}{k_1} \\ q_r &\equiv 2C_q \frac{k_2}{k_1}(1 - \frac{k_o}{k_2}) \\ q_m &\equiv 2C_q w \frac{k_o}{k_1}\delta_o (1 - \frac{k_o}{k_2}) \end{aligned}$$

Finally, substituting expressions for $\partial Q_1/\partial x$, $\partial Q_2/\partial x$, Q_y into the governing equations Eq. 2.12, one can obtain the next set of equations.

$$D_1 \frac{\partial y_1}{\partial t} = -C_y(w - y_2' + y_1) - q_r \frac{\partial^2 y_2'}{\partial x^2} + q_m \frac{\partial^3 y_2'}{\partial x^3} + q_1 \frac{\partial^2 y_1}{\partial x^2} \quad (2.21)$$

$$D_2 \frac{\partial y_2'}{\partial t} = C_y(w - y_2' + y_1) - q_2 \frac{\partial^2 y_2'}{\partial x^2} \quad (2.22)$$

By solving these two equations for y_2' and y_1, one can examine the change in time of shoreline position. Dalrymple (1997) developed a numerical model and obtained the solutions to this model. The results will be presented in Chapter 5.

2.3.3 Dimensional Analysis

To determine which parameters are more important in the linearized equation, the dimensional analysis was performed. In this analysis, to avoid confusion the symbol y_2' was replaced by y_2. (Actually, any derivative of y_2' would be same as that of y_2 due to the relationship $y_2 = y_2' - w$.) Combining Eq. 2.21 and Eq. 2.22, one can get Eq. 2.23.

$$\begin{aligned} D_1 D_2 \frac{\partial^2 y_2}{\partial t^2} + C_y(D_1 + D_2)\frac{\partial y_2}{\partial t} - (q_2 D_1 + q_1 D_2)\frac{\partial^3 y_2}{\partial t \partial x^2} \\ -C_y(q_1 + q_2)\frac{\partial^2 y_2}{\partial x^2} + C_y q_r \frac{\partial^2 y_2}{\partial x}\partial x^2 - q_m C_y \frac{\partial^3 y_2}{\partial x^3} + q_1 q_2 \frac{\partial^4 y_2}{\partial x^4} = 0 \end{aligned} \tag{2.23}$$

First, it is necessary to introduce three nondimensional parameters:

$$x' = kx \ ; \ y' = ky \ ; \ t' = \sigma t$$

where k is the wavelength of sand waves, σ is the wave frequency of sand waves and x', y', t' are dimensionless. Substituting these into Eq. 2.23,

$$\begin{aligned} \frac{\partial^2 y_2'}{\partial t'^2} + \frac{C_y(D_1 + D_2)}{\sigma D_1 D_2}\frac{\partial y_2'}{\partial t'} - \frac{k^2(q_2 D_1 + q_1 D_2)}{\sigma D_1 D_2}\frac{\partial^3 y_2'}{\partial t' \partial x'^2} - \frac{C_y k^2(q_1 + q_2)}{\sigma^2 D_1 D_2}\frac{\partial^2 y_2'}{\partial x'^2} \\ + \frac{C_y k^2 q_r}{\sigma^2 D_1 D_2}\frac{\partial^2 y_2'}{\partial x'^2} - \frac{k^3 q_m C_y}{\sigma^2 D_1 D_2}\frac{\partial^3 y_2'}{\partial x'^3} + \frac{k^4 q_1 q_2}{\sigma^2 D_1 D_2}\frac{\partial^4 y_2'}{\partial x'^4} = 0 \end{aligned}$$

Further, using following additional nondimensional parameters:

$$q_1' = \frac{k^2 q_1}{\sigma D_1} \ ; \ q_r' = \frac{k^2 q_r}{\sigma D_1} \ ; \ q_m' = \frac{k^3 q_m}{\sigma D_1} \ ; \ q_2' = \frac{k^2 q_1}{\sigma D_1} \ ; \ C_y' = \frac{C_y}{\sigma D_1}$$

the nondimensional equation finally becomes

$$\frac{\partial^2 y_2'}{\partial t'} + \left(\frac{D_1}{D_2} + 1\right) C_y' \frac{\partial y_2'}{\partial t'} - \left(\frac{D_1}{D_2} q_2' + q_1'\right) \frac{\partial^3 y_2'}{\partial t' \partial x'^2} - \left(\frac{D_1}{D_2}\right) C_y' (q_r' - q_1' + q_2') \frac{\partial^2 y_2'}{\partial x'^2} - \left(\frac{D_1}{D_2}\right) q_m' C_y' \frac{\partial^3 y_2'}{\partial x'^3} + \left(\frac{D_1}{D_2}\right) q_1' q_2' \frac{\partial^4 y_2'}{\partial x'^4} = 0$$

As a result, it was found that the importance of terms strongly depends on the ratio of the two depths, D_1 and D_2.

Chapter 3

LABORATORY EXPERIMENT

To verify the results from numerical models, several experiments were performed using a circular basin at the Center for Applied Coastal Research at the University of Delaware. This chapter discusses the procedure of our experiments and their results.

3.1 Circular Wave Basin and Spiral Wavemaker

Our unique circular basin was designed for the study of littoral processes because it can simulate an infinitely long beach in the laboratory eliminating end boundary effects associated with conventional rectangular basins. Dalrymple and Dean (1972) developed the linear spiral wavemaker theory for this type of basin using small-amplitude assumptions. For this study, to predict wave angles in the basin, the linear spiral wavemaker theory will be used.

The circular wave basin is 8.53 m in diameter and 0.61 m in height. It has a spiral wavemaker at its center which is mounted on a pully-driven shaft. The spiral wavemaker consists of a steel drum 90 cm tall and a 57.4 cm in diameter. The rotation axis is offset 3.81 cm from the drum center. When the drum is rotated about this axis, regular spiral waves are generated (Dalrymple and Dean, 1972). Figure 3.1 shows the plan view of the basin.

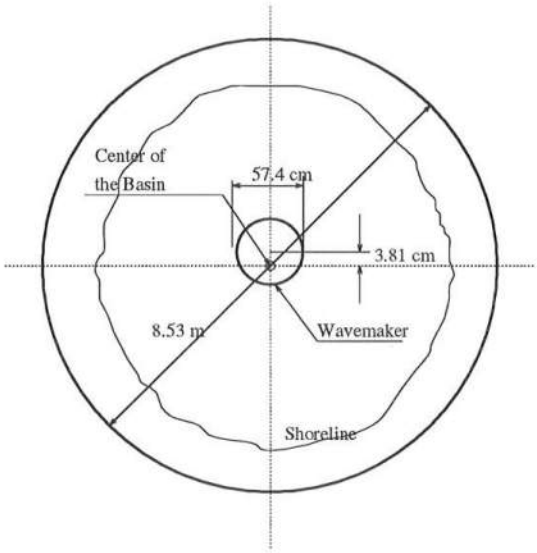

Figure 3.1: The plan view of the spiral basin

3.2 Equilibrium Beaches

For experiments, equilibrium beach conditions were needed. The most common way to express equilibrium profiles is to use the two-thirds power law, $h(y) = Ay^{2/3}$, which was originally introduced by Bruun (1954). Later, it was verified by Dean (1977), who examined more than 500 profiles on the US coast. Here, A is defined as the profile scale factor and is a function of the grain size. According to the sieve-analysis performed by Suh (1986), the mean size of the sand in the spiral basin is 0.41 mm (medium sand) and the standard deviation is 0.625 (relatively well-sorted). Refering the relationship between the profile scale factor A and the diameter of sediments (Moore, 1982), A can be predicted as around 0.1.

Equilibrium beach profiles were constructed by generating waves of constant size and period for several hours, until a survey showed insignificant change in the beach profile. Figure 3.2 shows the temporal variation of the profiles at the same location. Figure 3.3 explains the spatial variation of the profiles at the same time. The plots indicate that profiles are nearly stable temporally at the same location, while they have some spatial variations, especially in the offshore region. These variations are difficult to avoid without the extremely careful construction of beaches. However, the test area would be in the very shallow zones of less than 6 cm depth. Thus, as long as the profiles remain constant in this region, it is possible to say that equilibrium has been established at least locally. Due to the short distance between the beach face and the wavemaker, relatively steep profiles were observed at the offshore.

After establishing equilibrium conditions, the profiles were carefully measured. Dashed lines represent calculated equilibrium profiles using $h = Ay^{\frac{2}{3}}$ with $A = 0.1$, which was predicted by the size of sediments in the basin, in both figures.

In the region shallower than 12 cm depth, they show very good agreement with this value.

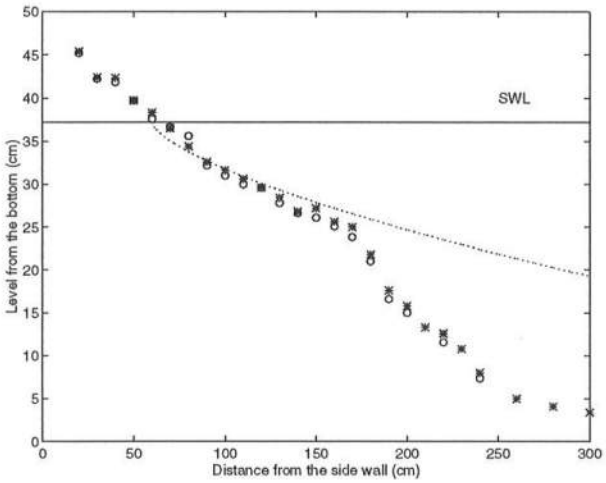

Figure 3.2: The temporal comparison at the tank center on September 13, 1996 (o) and September 30, 1996 (*). The dashed line denotes the calculated profile by $h = Ay^{\frac{2}{3}}$ with $A = 0.1$.

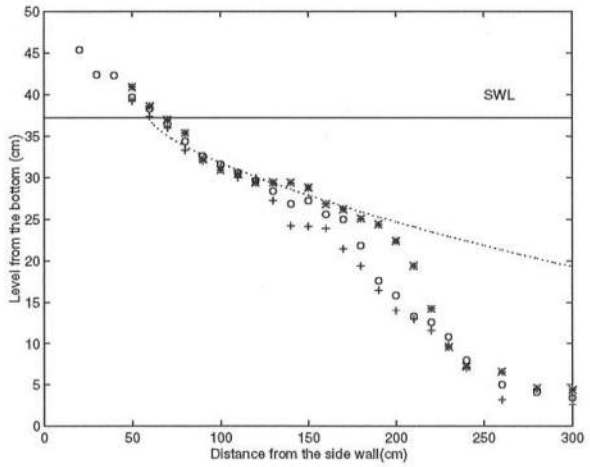

Figure 3.3: The spatial comparison on September 30, 1996 at the tank center (o), 30 degree to the right(*) and 30 degree to the left (+). The dash line denotes the calculated profile by $h = Ay^{\frac{2}{3}}$ with $A = 0.1$.

3.3 Measurement Tools

A level bar specifically designed for this basin was used to conduct all surveys. It crosses from the central shaft of the spiral wavemaker to the cinder block side wall. At the center, the level is mounted on top of the shaft with a circular cap so that it can rotate freely. At the outer wall, it is shaped like a T-bar, both for stability and for easier adjustment of its position.

For horizontal measurements, the distance from the side wall was determined by a tape measure attached to the level bar, while for vertical measurements a vernier attached to the level bar was used to measure elevations of the still water surface and the beach profiles. The vernier can slide along the bar over almost the whole tank radius. The level bar was capable of rotating around the center of the basin while keeping a constant horizontal position so that almost the entire tank could be covered by this equipment, excepting only a small range behind the steel tower that supports the wavemaker drum. As a result, wave fields behind the steel tower were rather different from those in other ranges due to the scattering effect of the steel structure. However, for this experiment, only a half range in front of the wavemaker was used.

Cylindrical coordinate system (r, θ, z) were established in the basin. First, let the center of the basin be the origin and take the r-axis positive to front side of the basin, which is opposite side of the supporting structure of the drum. Then, mark standard reference points every 20 cm along the side wall where each 20 cm arc corresponds positive 2.7 degree in right direction and negative in left. Figure 3.4 shows an example of the mesh at test site.

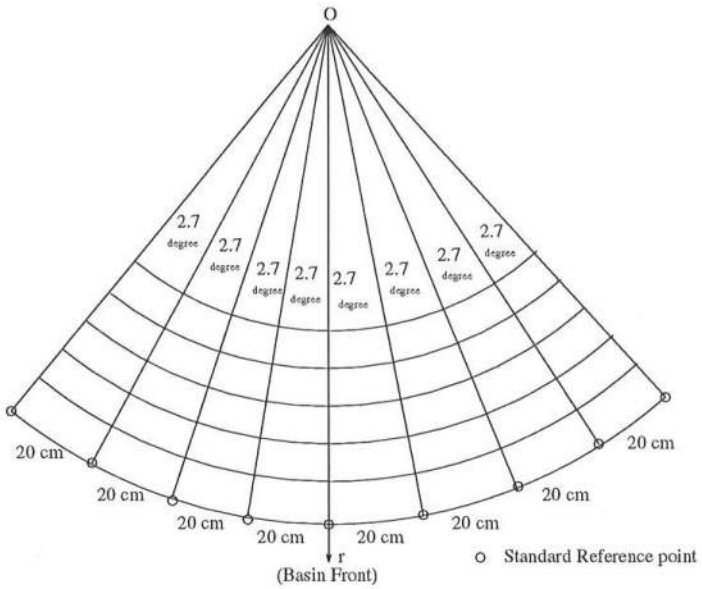

Figure 3.4: Example of mesh

3.4 Wave Measurements

Two capacitance type wave gauges were used to measure the free surface elevation and incident wave angles. The gauges were mounted on tripods using the specially fabricated equipment and were located at certain points in the basin, as shown in Figure 3.5.

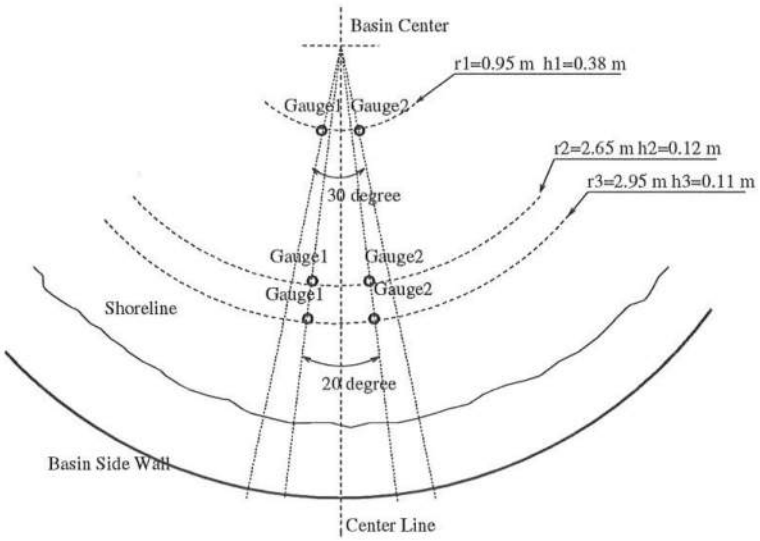

Figure 3.5: Locations of wave gauges

The gauges were calibrated at the beginning of each run. Two stepper motors were used to move the gauges up and down by 1 cm increments and carry out the calibrations accurately. The motors were connected to a PC through a motor controller and an amplifier. The calibration operations were synchronized by FORTRAN programs. Calibration ranges were from 3.0 cm below the still water level to 3.0 cm above the still water level. At each of the 7 points data were taken two times, then those were averaged to get the final data for calibration curves.

Calibrations curves were made for converting the voltage data from the wave gauges to free surface elevation data. The calibration curves were nearly linear in each case. Figure 3.6 shows the results of the calibrations.

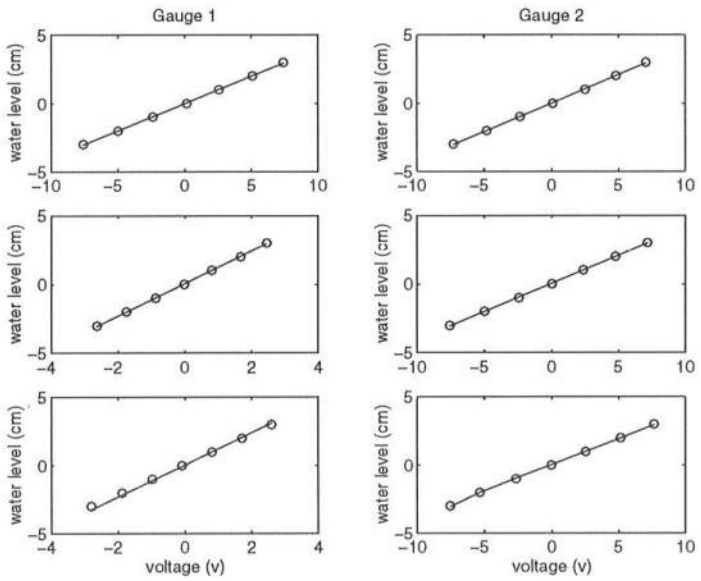

Figure 3.6: Calibration curve fitting by results at $r_1 = 0.95\ cm$ (upper), $r_2 = 2.65\ cm$ (middle) and $r_3 = 2.95\ cm$ (lower).

The wave measurements were made at three different locations: $r_1 = 0.95\ m$, $r_2 = 2.65\ m$, and $r_3 = 2.95\ m$ from the center of the basin, referring Figure 3.5. At each location two wave gauges were set up to take data of the surface displacement. The reason for the use of two gauges was that the calculations of the angle of wave incidence were needed, using the time lag between the two wave gauges. Locations were selected as one for offshore wave data, one for waves in nearshore and one for between those. Due to both the period of waves and the water depth in the basin, even at the center, waves were not in deep water. According to the profiles from the survey, there was a change in the slope of the bottom at approximately $r_2 = 2.65\ m$ where the depth was 12 cm. Regarding the

last location, it could be possible to be set up much closer to the shoreline, within the surf zone; however, due to the unreliability of data in extremely shallow water, the guages were set at $r_3 = 2.95\ m$ where the depth was 11 cm. As a result, the water depth and the angle of each wave gauge are $h_1 = 38\ cm$, $\phi_1 = 30^o$, $h_2 = 12\ cm$, $\phi_2 = 20^o$, and $h_3 = 11\ cm$, $\phi_3 = 20^o$, respectively.

It was found to be better to use small angles ϕ to reduce error in the linear approximation of the arc between two gauges. Since at $r_1 = 0.95\ m$ the distance between two gauges became very small, there was a concern that wave scattering from one of the wave gauge supports would affect the other gauge, thus a larger angle, $\phi_1 = 30^o$, was adopted only for this location. The sampling rate was 50 Hz and the duration for each sampling was 200 sec. The first 40 second of time series of water surface elevations at each location are plotted in Figure 3.7, Figure 3.4 and Figure 3.9.

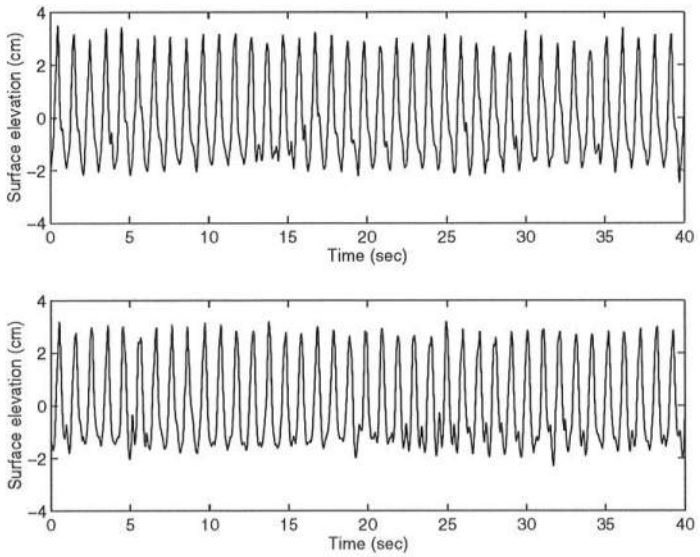

Figure 3.7: Time series of surface displacement at $r = 0.95\,m$ at gauge 1 (upper) and at gauge 2 (lower).

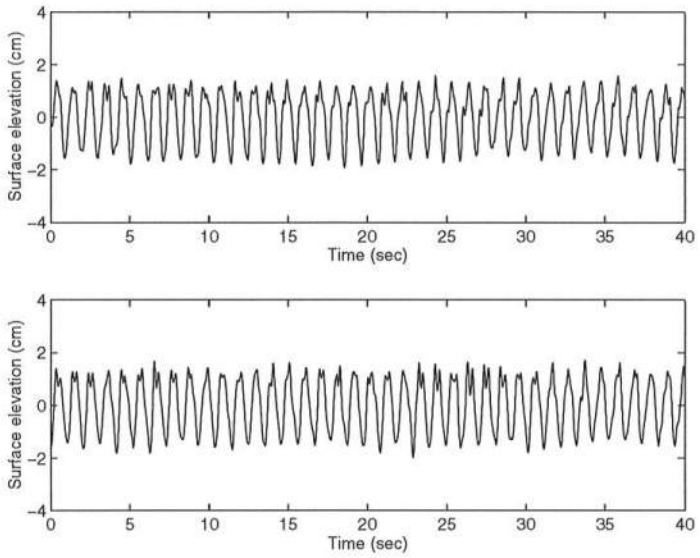

Figure 3.8: Time series of surface displacement at $r = 2.65\,m$ at gauge 1 (upper) and at gauge 2 (lower).

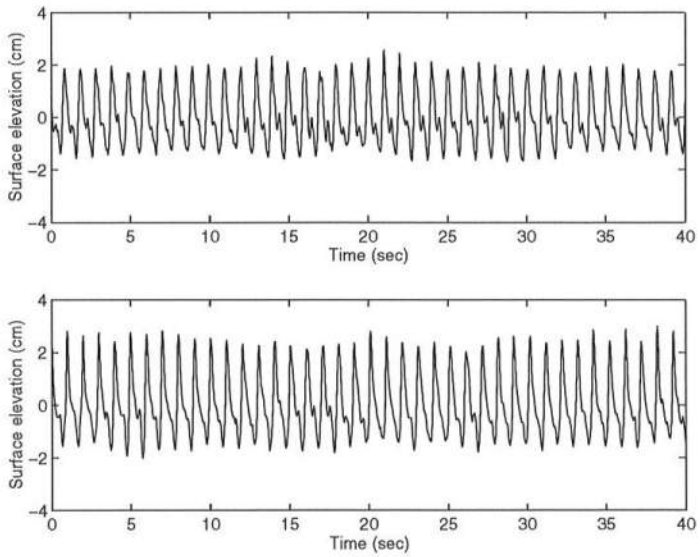

Figure 3.9: Time series of surface displacement at $r = 2.95\,m$ at gauge 1 (upper) and at gauge 2 (lower).

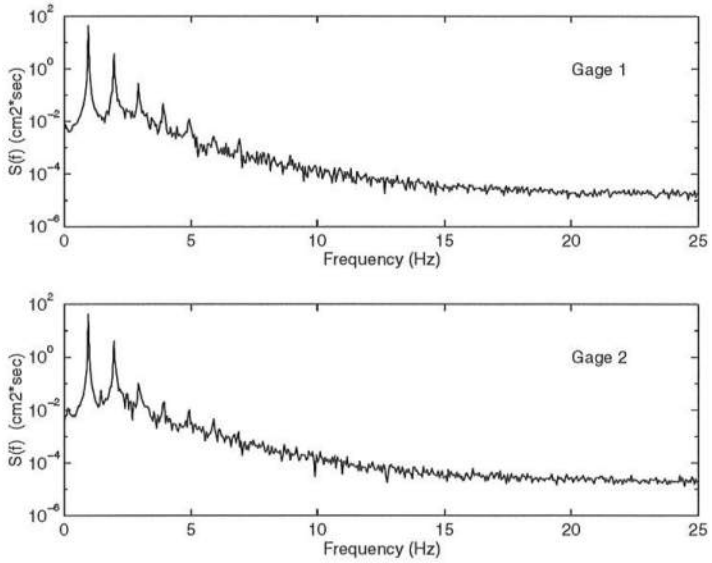

Figure 3.10: Power spectra of surface displacement at $r = 0.95\,m$ at gauge 1 (upper) and at gauge 2 (lower).

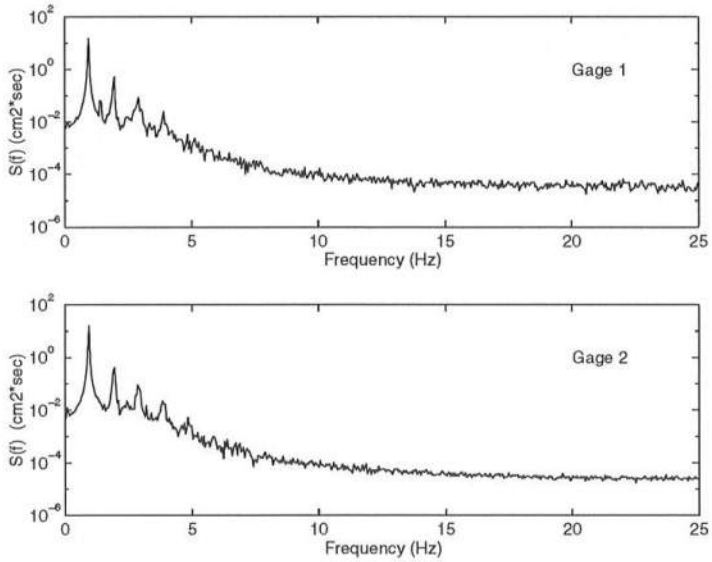

Figure 3.11: Power spectra of surface displacement at $r = 2.65\,m$ at gauge 1 (upper) and at gauge 2 (lower).

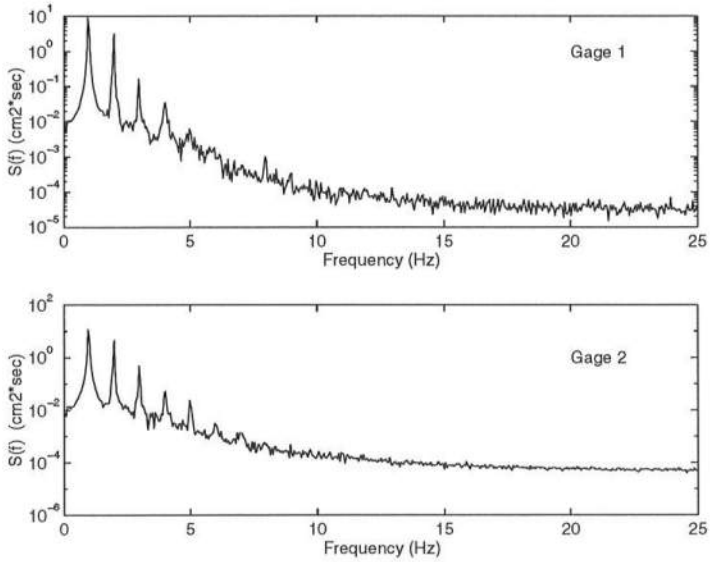

Figure 3.12: Power spectra of surface displacement at $r = 2.95\,m$ at gauge 1 (upper) and at gauge 2 (lower).

Next, a spectral analysis was made to determine wave periods and wave heights. The data sets of surface elevations were transformed by using a first Fourier Transform from the time domain into the frequency domain, then the power spectra were plotted against frequencies as shown in Figure 3.10, Figure 3.11 and Figure 3.12. The peak frequencies and periods were determined from each power spectrum. The peak period was T=0.98 sec, which seemed to stay the same throughout the entire experiment.

The root-mean-square of the wave height is determined as follows. First, the time-averaged specific wave energy per unit area is expressed as (Goda, 1978):

$$\rho g\overline{(\eta - \eta_o)^2} = \rho g \int_0^\infty S(f)df = \rho g m_o \tag{3.1}$$

with

$$m_o = \int_0^\infty S(f)df \tag{3.2}$$

where $S(f)$ is a frequency power spectrum and m_o is a zeroth-moment of $S(f)$. η is the water surface elevation and η_o is an average of η. So, $\overline{(\eta - \eta_o)^2}$ represents a variance of η. On the other hand, the time-averaged energy per unit area based on the linear wave theory would be $\frac{1}{8}\rho g H_{rms}^2$. Equating those two expressions we have:

$$\rho g m_o = \frac{1}{8}\rho g H_{rms}^2 \tag{3.3}$$

Finally,

$$H_{rms} = \sqrt{8m_o} \tag{3.4}$$

Table 3.1 shows results of wave heights for this experiment.

Table 3.1: Root-mean-square wave height

	H_{rms}	
Location	Gauge 1	Gauge 2
r_1	4.54	4.46
r_2	2.87	2.96
r_3	2.82	3.24

The incident wave angle was also calculated at each location. Refering Figure 3.13, let points A and B be the wave gauge locations and let O be the center of the tank. The radii of both two points are the same, say, r. Define the angle between line OA and OB as ϕ. The distance between A and B is determined by the geometry.

$$d = 2r \sin\frac{\phi}{2} \tag{3.5}$$

Further, assuming the wave crest at $t = t_1$ and $t = t_1 + \Delta t$, passes through the point A and B respectively, the incident angles with respect to shoreline

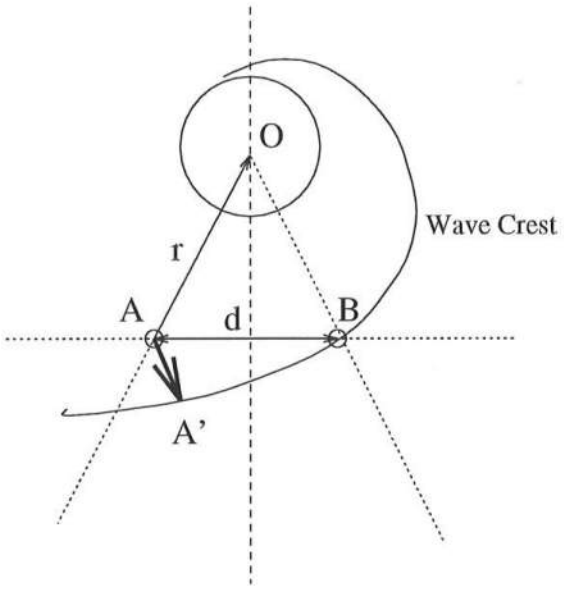

Figure 3.13: Diagram for calculation of time lag

normal are approximately calculated as follows. Suppose Δt is very small and the point A moves to the point A' after $t = \Delta t$. The radius of the curvature of the spiral crest would be large enough to approximate the curve between A' and B as the straight line. Since travelling directions of waves are perpendicular to the crest line, the incident wave angle θ would be equal to $\angle ABA'$ by geometry. The angle θ would be determined using the trigonometric relation.

$$\theta = \arcsin \frac{\Delta \ell}{d} \tag{3.6}$$

where $\Delta \ell$ is the distance between A and A'. $\Delta \ell$ would be calculated by examining the time lag Δt of waves between two gauges,

$$C = \frac{L}{T}, \longrightarrow \Delta \ell = C \Delta t$$

So,

$$\theta = \arcsin \frac{C \Delta t}{d} \tag{3.7}$$

Here, the phase speed should be calculated from dispersion relationship (Dean and Dalrymple, 1984).

$$\sigma^2 = gk \tanh kh$$

$$\omega = \frac{2\pi}{T}, k = \frac{2\pi}{L}$$

Finally, Δt needs to be determined. For this, the cross-correlation function was used. The cross-correlation function between data from gauge 1 and gauge 2 is expressed as follows (Bendat and Piersol, 1986).

$$C_{12}(\tau) = \frac{1}{N-\tau} \sum_{t=1}^{N} \eta_1(t)\eta_2(t+\tau) \qquad 0 \leq \tau \leq \tau_{max}$$

where N is the number of sample points from each gauge, η_1 is the water surface displacement data from gauge 1, η_2 is the water surface displacement data from gauge 2, τ is the time lag between two gauges, T is the peak period of the waves (sec). f_s is a sampling rate (Hz) and τ_{max} is a sampling time which corresponds to one wave length (i.e. one period). Since a time lag should be very small in this case compared to the wave period, a domain of τ would be limited. The correlation function would be maximized when two data sets correlated perfectly, which means that the τ which maximized the cross-correlation function would be the desirable time lag (Bendat and Piersol, 1986). In other word, if one of the data sets is shifted by this τ, the most perfect match would occur between the two records. Correlation function over a wave period in each case were plotted in Figure 3.14, Figure 3.15 and Figure 3.16. Taking the maximum values for each case, one can obtain the time lags. Then, using Eq. 3.7 the angles of wave incidence could be calculated. Table 3.2 shows results of calculation for the time lag.

Dalrymple and Dean (1972) expressed that the angle between the normal to the wave crest and the radial direction as:

$$\theta = \arctan(\frac{1}{k_o r}) \tag{3.8}$$

However, this equation does not take into acount the variable depth. Meanwhile, Mei (1983) modified Snell's law for circular depth contours,

$$kr \sin\theta = constant \tag{3.9}$$

Table 3.3 is a comparison of the angles of wave incidence including the results from other theories, which are the linear spiral wavemaker theory (Dalrymple and Dean, 1972) and the modified Snell's law for circular contours (Mei, 1983). Since it was impossible to apply the modified Snell's law to deep water regime because the radial position at offshore, r_o must be given. Instead, r_1 can be taken as a reference point so that one can evaluate the constant value for the modified Snell's law by using the wavenumber and the wave angle at r_1 from the experiment. Comparison showed that the spiral wavemaker theory gave closer results to the experimental result than the modified Snell's law.

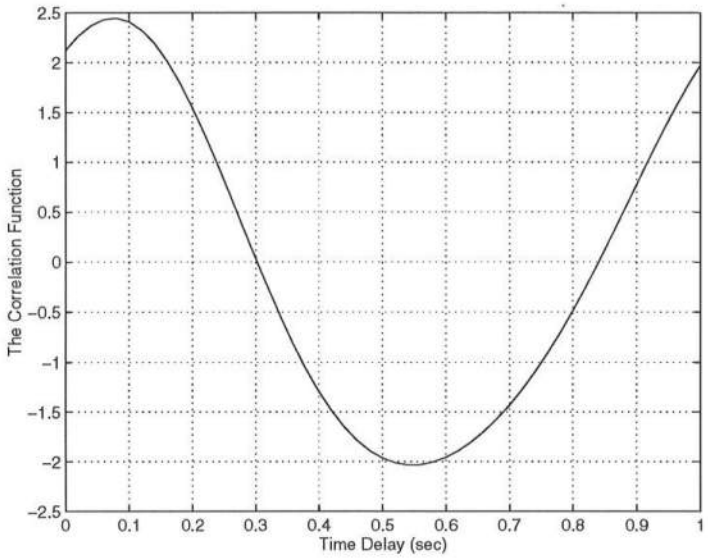

Figure 3.14: Correlation function over a wave period at $r = 0.95m$.

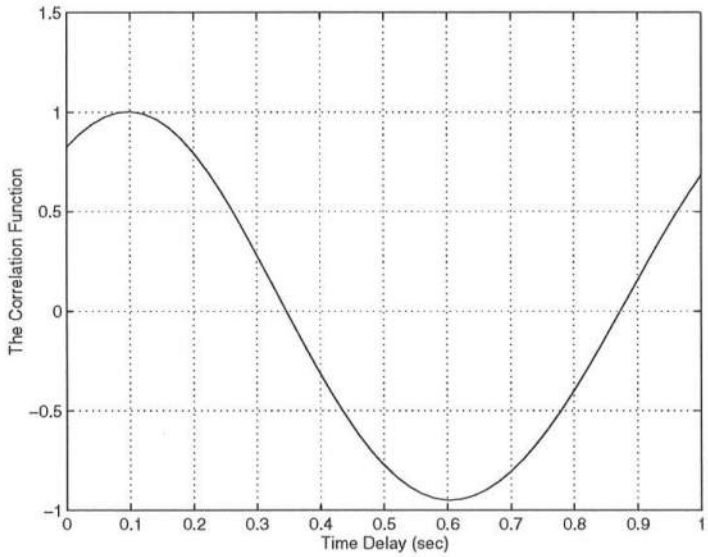

Figure 3.15: Correlation function over a wave period at $r = 2.65m$.

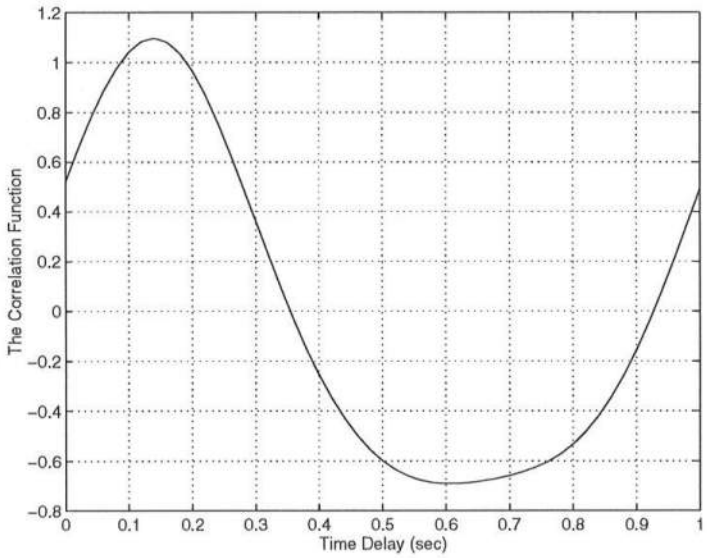

Figure 3.16: Correlation function over a wave period at $r = 2.95m$.

Table 3.2: Calculation of time lag

r (m)	h (m)	k (m^{-1})	L (m)	T (sec)	C (m/sec)	ϕ $(degree)$	d (m)	τ (sec)	θ $(degree)$
0.95	0.38	4.52	1.390	0.98	1.418	30	0.492	0.08	13.3
2.65	0.12	6.50	0.967	0.98	0.987	20	0.920	0.10	6.2
2.95	0.11	6.73	0.934	0.98	0.953	20	1.024	0.14	7.5

Table 3.3: Comparison of incident wave angles (unit:degree)

Gauge Location	r_1	r_2	r_3
Laboratory Experiment	13.3	6.2	7.5
Spiral Wavemaker Theory	14.1	5.1	4.6
Modified Snell's Law	13.3	3.3	2.9

3.5 Longshore Sediment Transport

The rate of longshore sediment transport was determined by measuring profile changes in the circular tank. At equilibrium, the single groin method, which traps all longshore sediments in the surf zone, was used for measuring the rate of sediment transport. The rectangular shaped groin was buried along the profile. The length of the groin was sufficient to ensure no bypassing at its offshore end. Offshore, the top of the groin was below the still water level so that its effects on the wave fields was reduced. The groin was made of a hard plastic and was heavy enough both to be stable in water and to resist wave action.

On the upwave side of the groin, for 1.8 m along the side wall, 10 test profiles were measured. The profiles were taken along radii from the center of the basin. The angle between two consecutive profiles was 2.7^o, which corresponded to a 20 cm arc at the center line of the side wall. In offshore region survey points were taken every 5 cm for a distance of 70 cm beginning at a point 50 cm from the side wall. The polar coordinate grid was used for calculating sand budgets in this region. Sections were numbered from 1 to 10, with section 10 just to the left side of the groin.

Figure 3.18 to Figure 3.22 show the profile changes at each section. Four surveys were conducted at T=0 min, 10 min, 30 min and 60 min. Reviewing the profile changes, it was clear that as the section closer to the groin, the profile changes were significant. Also, one can say the test domain was broad enough for our purpose because the profile at section 1 remained nearly unchanged, which means the test area covered almost all area affected by the groin.

Since all longshore sediment would be trapped by the groin, the volume changes in the test area would indicate the rate of longshore sediment transport,

which was the amount of the sediment coming into the test area from upwave side. Taking into account the distortion of the grid due to the use of polar coordinate system, the change of volume was calculated by simply multiplying the depth changes at each survey point dh by the area of the mesh grid dA. Figure 3.17 shows the example of the mesh grid in the test area.

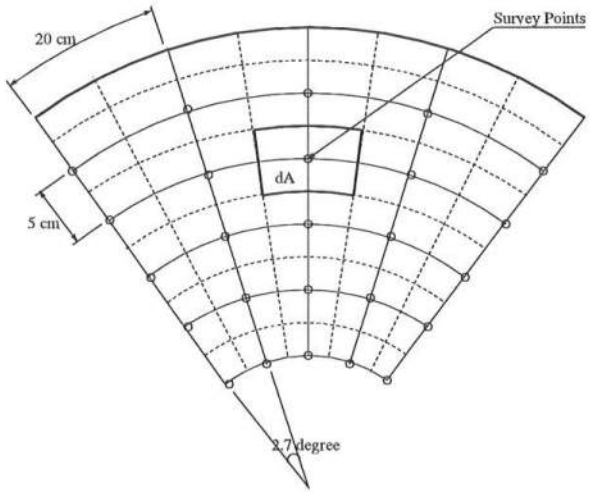

Figure 3.17: Mesh grid for measuring the longshore transport rate

Table 3.4 shows the calculations of the longshore sediment transport coefficient from the measurements. The values on the first row were calculated from the depth change from T=0 min to T=10 min. The other rows are T=10 min to T=30 min, T=30 min to T=60 min and T=0 min to T=60 min.

Some formulae used for the calculations are as follows (Dean and Dalrymple, 1997):

$$H_b = \kappa h_b$$

$$C_{g_b} = C_b = (gh_b)^{\frac{1}{2}}$$

$$k_3 r_3 \sin \alpha_3 = k_b r_b \sin \alpha_b$$

$$E_b = \frac{1}{8}\rho g H_b^2$$

$$Q = \frac{\mathcal{K}(EC_g)_b \sin \alpha_b \cos \alpha_b}{\rho g(s-1)(1-p)}$$

where H_b is the breaking wave height, h_b is the water depth at the breakerline, $\kappa(= 0.78)$ is the wave breaking index for a spilling breaker, C_b and C_{g_b} are the wave phase speed and the wave group velocity at the breakerline, respectively, α_b is the wave incident angle at the breakerline, r_b is the distance from the center of the basin to the breakerline, E_b is the wave energy at the breakerline, Q is the volumetric longshore sediment transport rate, $\mathcal{K}$ is a longshore transport coefficient, p $(= 0.4)$ is the porosity of sand, and s $(= 2.65)$ is the specific gravity of sand. To calculate α_b, the modified Snell's law were used taking the r_3 point, which was the farthest point, as the reference point because there was no data available at the breakerline.

The longshore transport coefficient, $\mathcal{K}$, was found to be approximately 0.77 in the field (Komar and Inman, 1970) and 0.25 in the laboratory (Das, 1972, cited in Suh, 1986). In this experiment, during the first 30 minutes the sediment were accumulated quicker, then, the amount of trapped sediment decreased quickly in the last 30 minutes. Averaging the results over the entire period of the run, one could use 1.01 as $\mathcal{K}$.

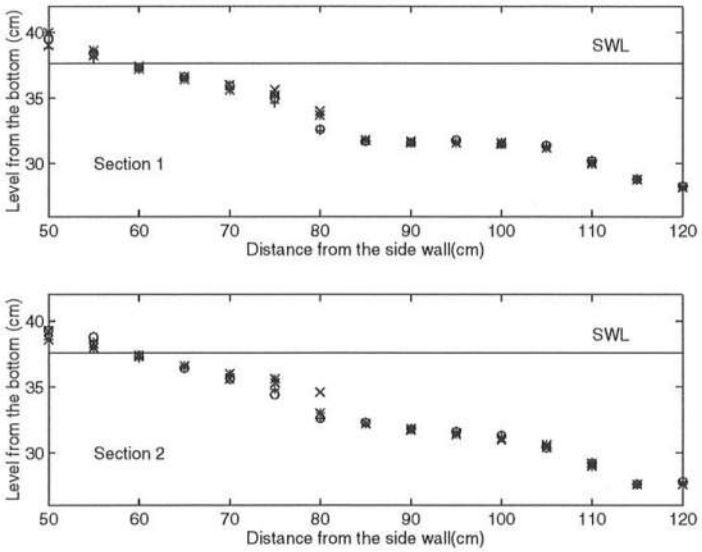

Figure 3.18: Profile changes at Section 1 and Section 2 due to the single groin; T=0 min (o), T=10 min (+), T=30 min (*), T=60 min (x)

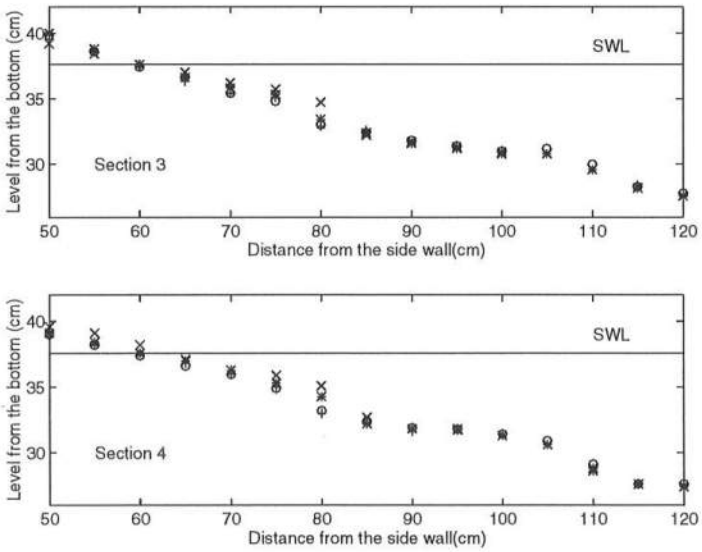

Figure 3.19: Profile changes at Section 3 and Section 4 due to the single groin; T=0 min (o), T=10 min (+), T=30 min (*), T=60 min (x)

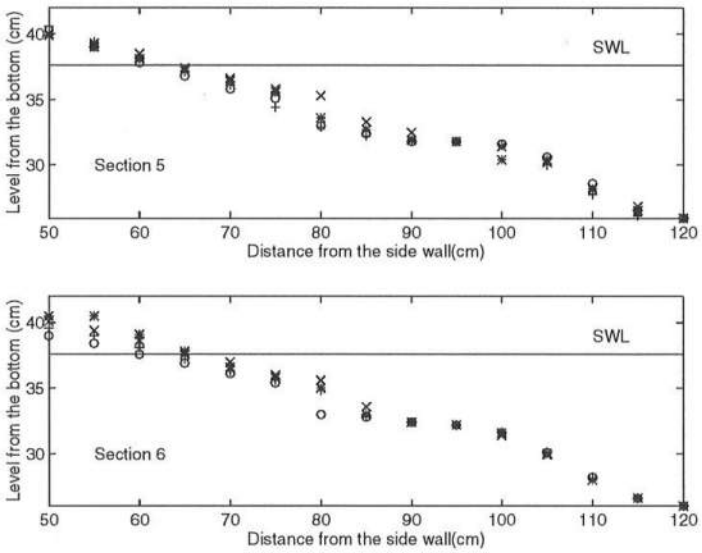

Figure 3.20: Profile changes at Section 5 and Section 6 due to the single groin; T=0 min (o), T=10 min (+), T=30 min (*), T=60 min (x)

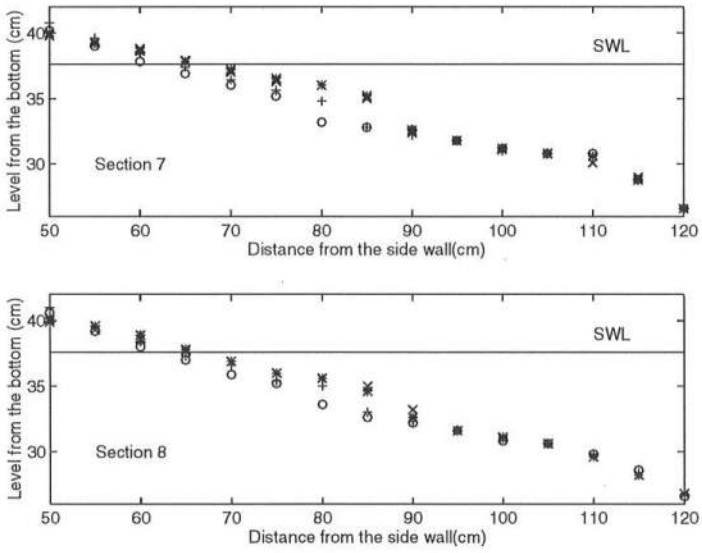

Figure 3.21: Profile changes at Section 7 and Section 8 due to the single groin; T=0 min (o), T=10 min (+), T=30 min (*), T=60 min (x)

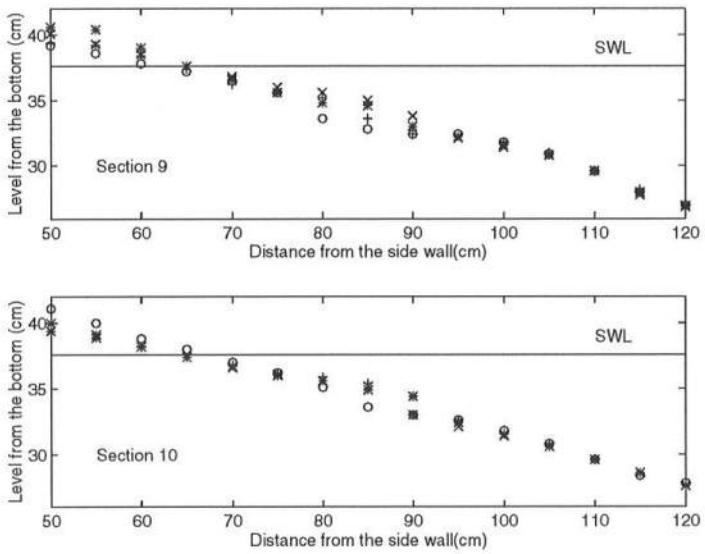

Figure 3.22: Profile changes at Section 9 and Section 10 due to the single groin; T=0 min (o), T=10 min (+), T=30 min (*), T=60 min (x)

Table 3.4: Calculation of longshore sediment transport rate

Δt (min)	ΔV (cm^3)	Q (m^3/day)	K
10	909.7	0.131	1.39
20	1959.2	0.141	1.49
30	1085.1	0.052	0.55
60	3954.0	0.095	1.01

3.6 Beach Fill

Only two complete tests were performed for this study because each test required approximately 3000 manual survey points which took a long time to measure due to the fairly primitive methods used. Despite its crudeness, however, this method worked suprisingly well.

The surveys were conducted at four times, T=0 min, T=3 min, T=10 min and T=20 min. 30 sections were taken at front side of the basin along radii and each section had 23 points spaced every 5 cm for a distance of 110 cm beginning at a point 50 cm from the side wall. So, each time 690 points surveys and in total 2760 times surveys were needed for this case. Figure 3.23 to Figure 3.26 show contours at each time. The initial shape of the beach fill would ideally have been perfectly rectangular, however, to account for the circular shape of the basin, the side borders of the fill were aligned with radii to the center of the basin. This way, the measured angle of wave incidence would be same as the angle of wave attack with respect to the side lines. The actual shape of the initial beach fill was trapezoidal, though the final plots were mapped onto a rectangular coordinate system so that thier initial shape appeared rectangular.

It is clear that the bathymetry beyond the depth 6 cm remained nearly unchanged, so 6 cm could be called the depth of closure. Following the same contour line over time, one can determine the evolutions of contours. The depth 6 cm corresponds 32 cm contour line measured from the basin bottom; the 38 cm line is the still water level and 35 cm is the middle of two depths as indicated in Figure 3.23 to Figure 3.26. So, the 38 cm lines represent the shorelines of each case.

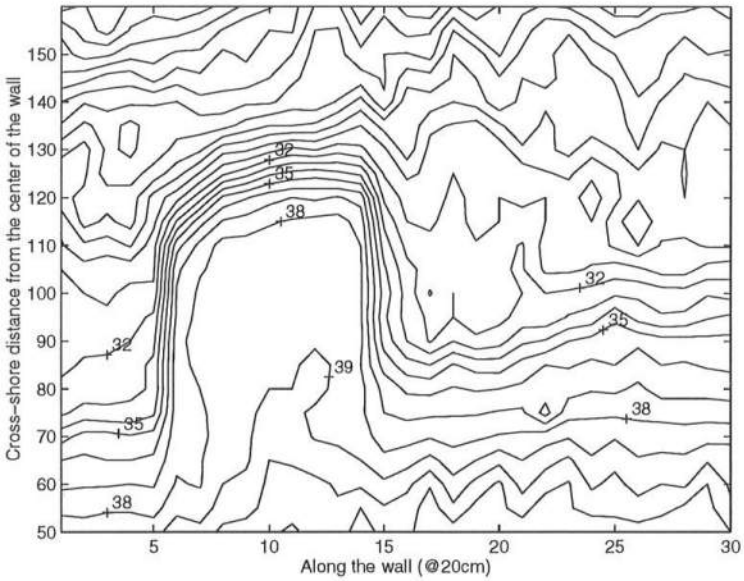

Figure 3.23: Contours at T=0 min (Beach Fill)

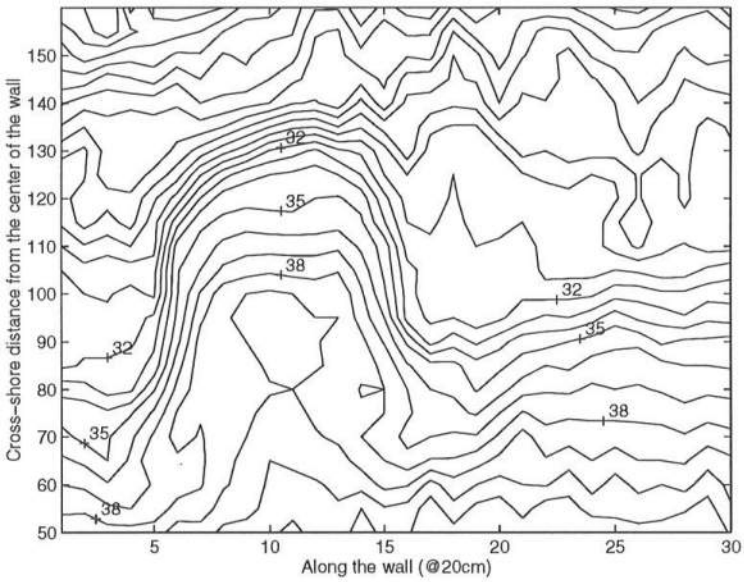

Figure 3.24: Contours at T=3 min (Beach Fill)

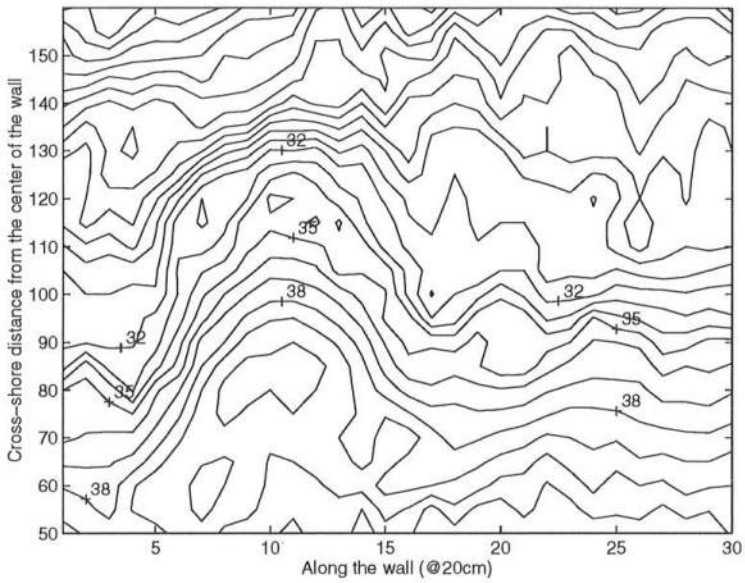

Figure 3.25: Contours at T=10 min (Beach Fill)

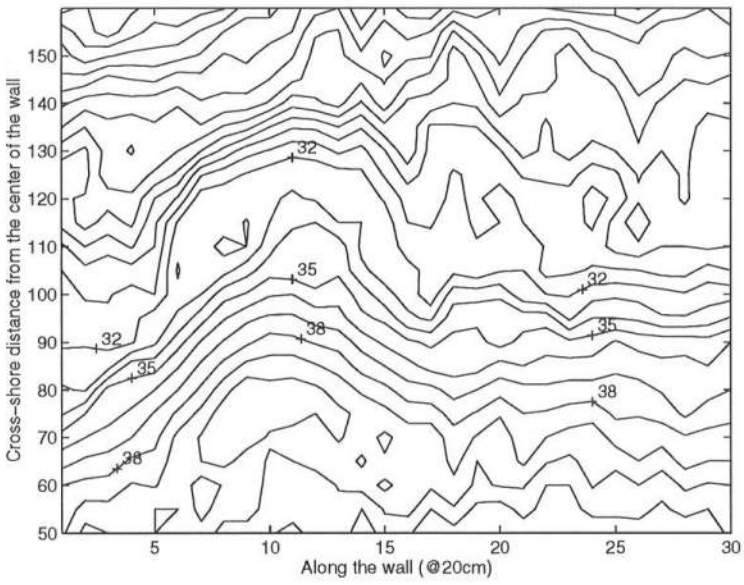

Figure 3.26: Contours at T=20 min (Beach Fill)

Figure 3.27 to Figure 3.41 show the profile change at the each section. Once again, one can notice that the offshore profiles were almost unchanged. Also, it is clear that there were remarkable erosion from section 6 to section 14, which correspond the beach fill. On the other hand, there were some accretion at both ends of beach fill. This phenomenon can explain the sand movement due to alongshore diffusion.

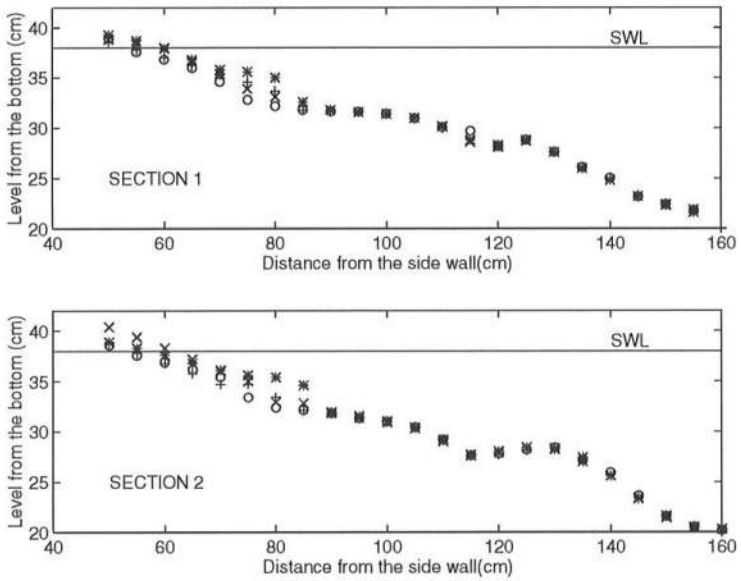

Figure 3.27: Profile changes at Section 1 and Section 2 (Beach Fill); T=0 min (o), T=3 min (+), T=10 min (*), T=20 min (x)

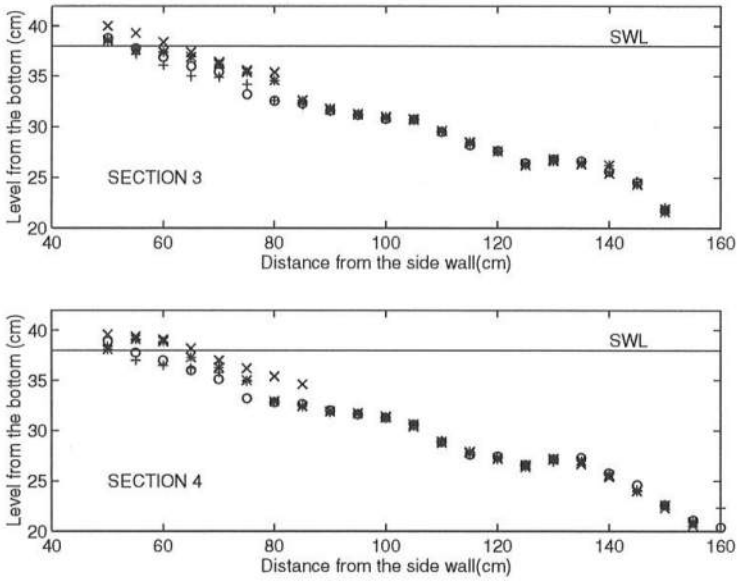

Figure 3.28: Profile changes at Section 3 and Section 4 (Beach Fill); T=0 min (o), T=3 min (+), T=10 min (*), T=20 min (x)

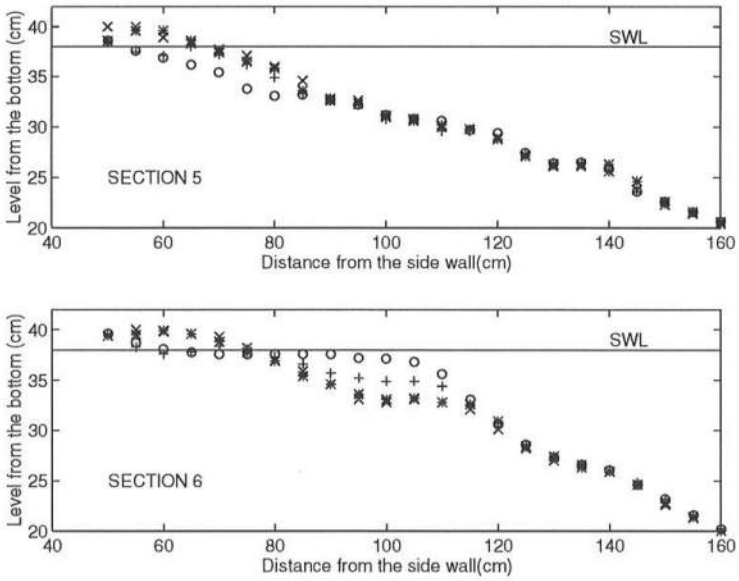

Figure 3.29: Profile changes at Section 5 and Section 6 (Beach Fill); T=0 min (o), T=3 min (+), T=10 min (*), T=20 min (x)

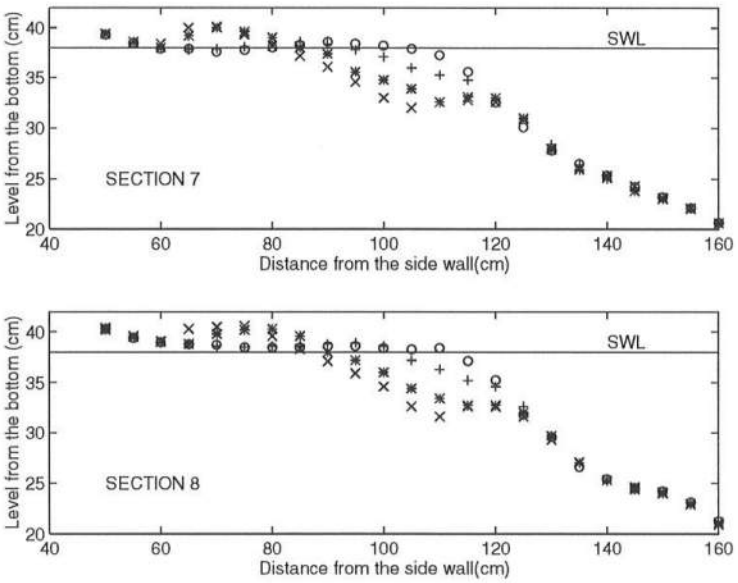

Figure 3.30: Profile changes at Section 7 and Section 8 (Beach Fill); T=0 min (o), T=3 min (+), T=10 min (*), T=20 min (x)

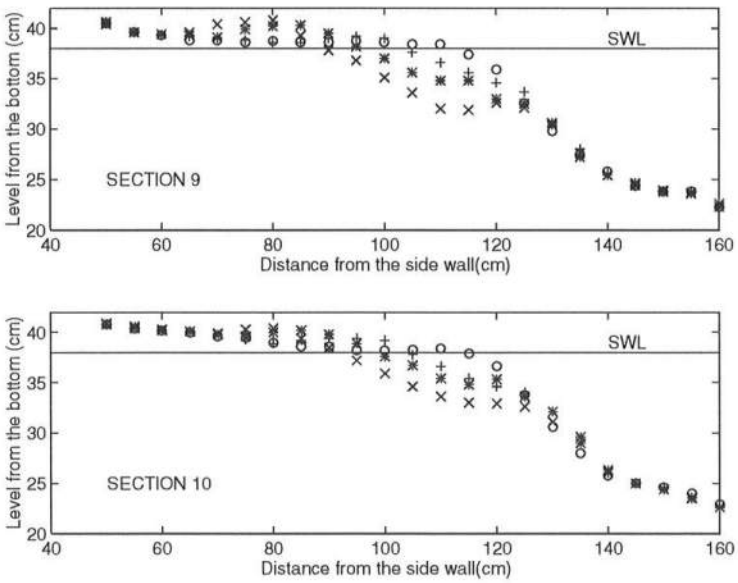

Figure 3.31: Profile changes at Section 9 and Section 10 (Beach Fill); T=0 min (o), T=3 min (+), T=10 min (*), T=20 min (x)

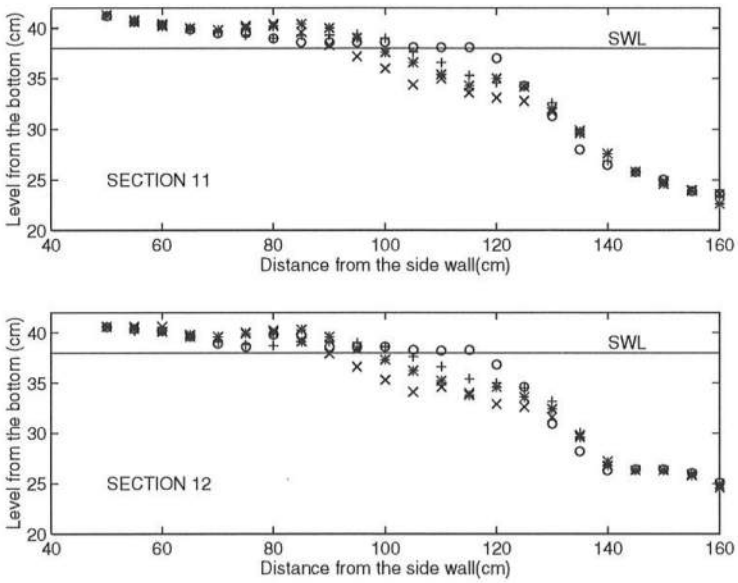

Figure 3.32: Profile changes at Section 11 and Section 12 (Beach Fill); T=0 min (o), T=3 min (+), T=10 min (*), T=20 min (x)

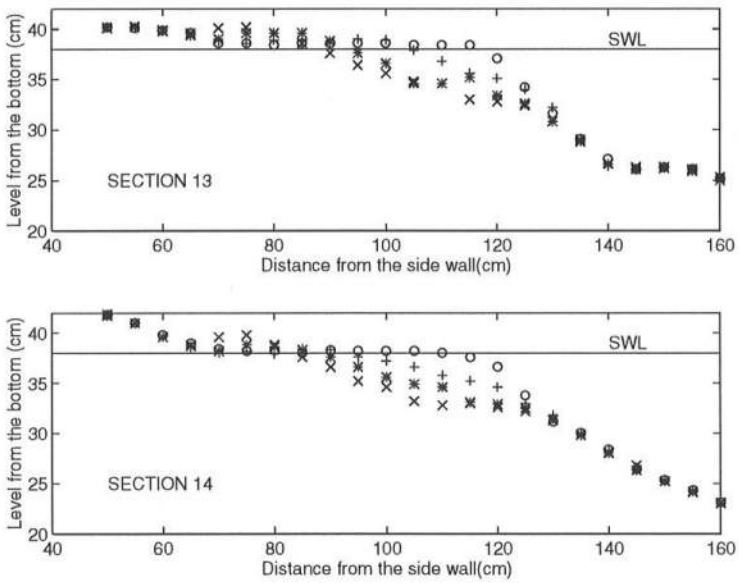

Figure 3.33: Profile changes at Section 13 and Section 14 (Beach Fill); T=0 min (o), T=3 min (+), T=10 min (*), T=20 min (x)

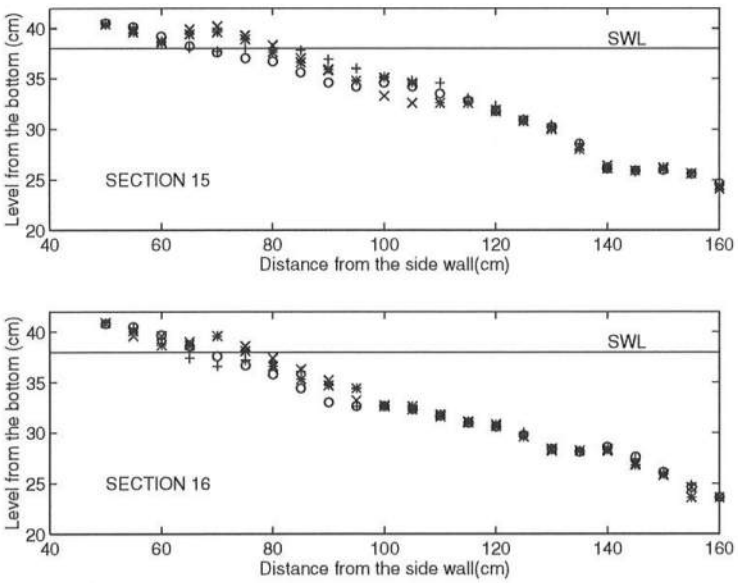

Figure 3.34: Profile changes at Section 15 and Section 16 (Beach Fill); T=0 min (o), T=3 min (+), T=10 min (*), T=20 min (x)

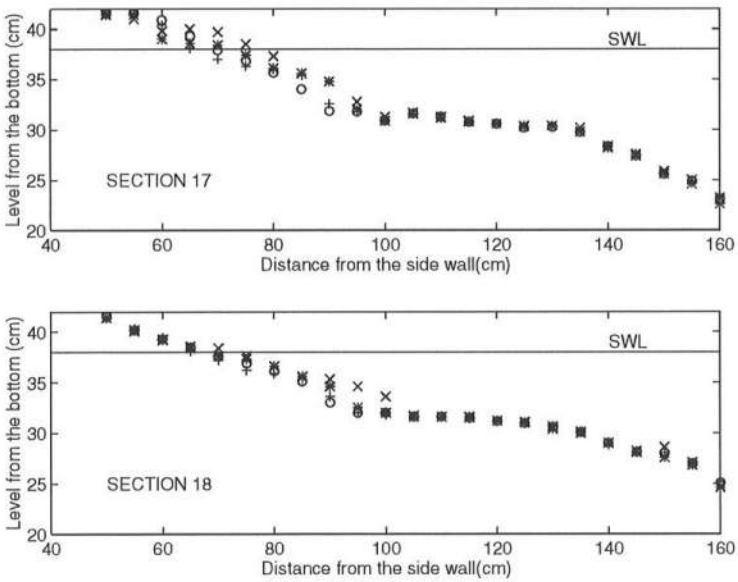

Figure 3.35: Profile changes at Section 17 and Section 18 (Beach Fill); T=0 min (o), T=3 min (+), T=10 min (*), T=20 min (x)

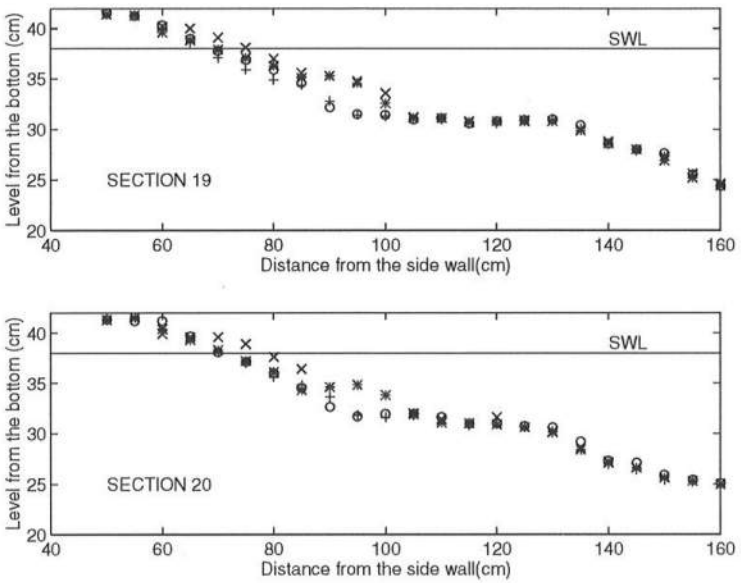

Figure 3.36: Profile changes at Section 19 and Section 20 (Beach Fill); T=0 min (o), T=3 min (+), T=10 min (*), T=20 min (x)

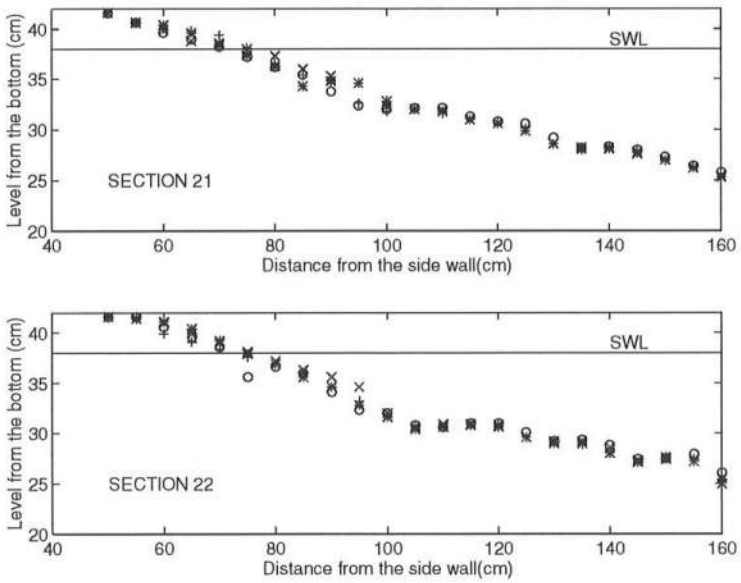

Figure 3.37: Profile changes at Section 21 and Section 22 (Beach Fill); T=0 min (o), T=3 min (+), T=10 min (*), T=20 min (x)

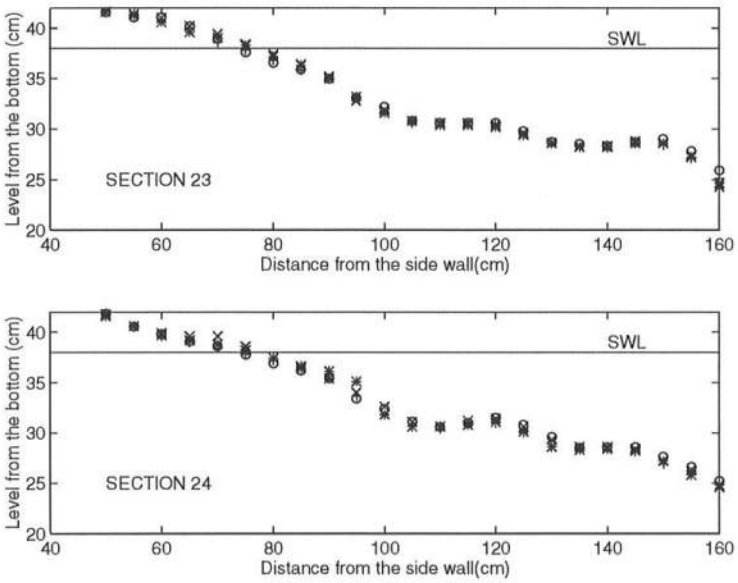

Figure 3.38: Profile changes at Section 23 and Section 24 (Beach Fill); T=0 min (o), T=3 min (+), T=10 min (*), T=20 min (x)

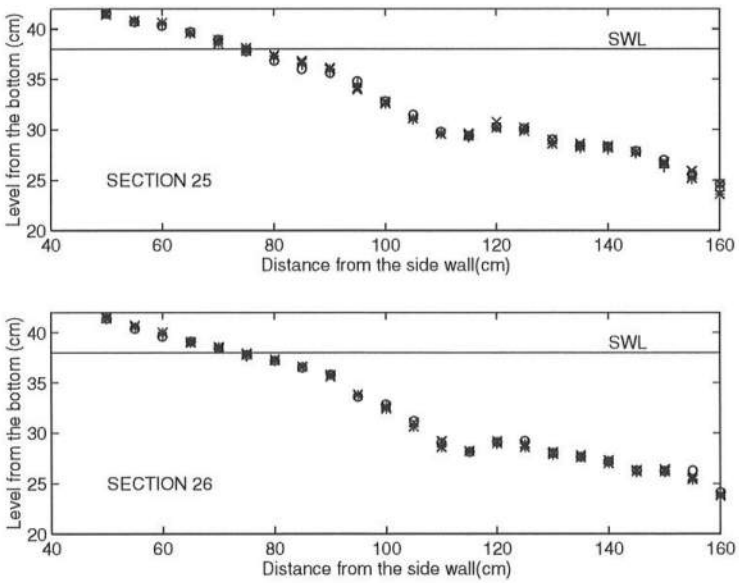

Figure 3.39: Profile changes at Section 25 and Section 26 (Beach Fill); T=0 min (o), T=3 min (+), T=10 min (*), T=20 min (x)

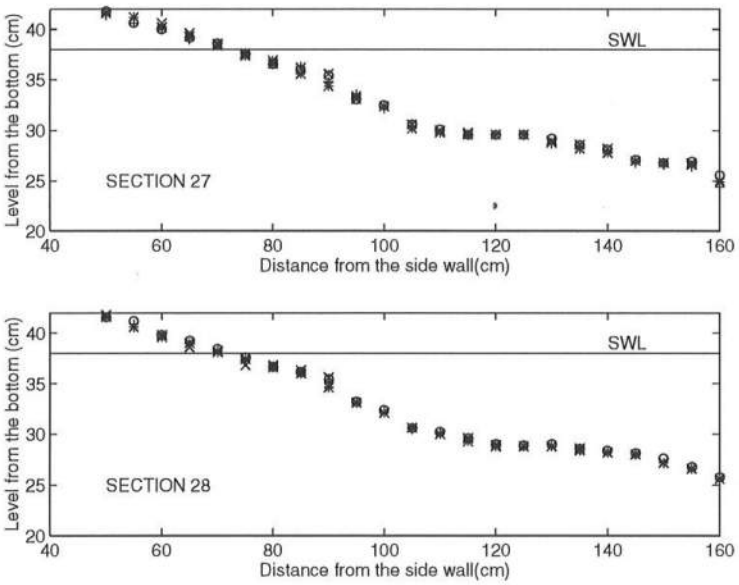

Figure 3.40: Profile changes at Section 27 and Section 28 (Beach Fill); T=0 min (o), T=3 min (+), T=10 min (*), T=20 min (x)

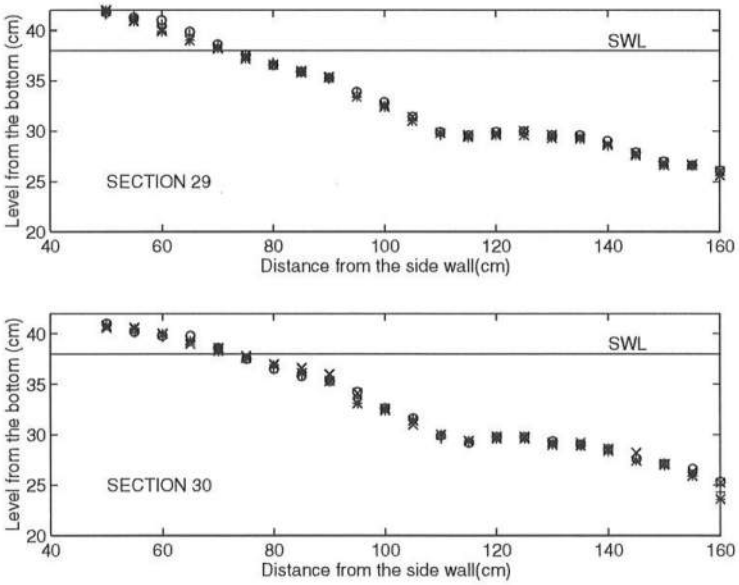

Figure 3.41: Profile changes at Section 29 and Section 30 (Beach Fill); T=0 min (o), T=3 min (+), T=10 min (*), T=20 min (x)

3.7 Periodic Beach

Since there are some area behind the wavemaker where wave fields are not same as those in front, it was impossible to simulate real infinitely periodic beaches, that is, to use the entire circumference of the basin. Furthermore, to keep the same spatial resolution as in the beach fill case would require an enormous number of measurements. However, it was possible to examine multiple beach fills as an alternative.

Three rectangular beach fills were constructed in the test area as shown in Figure 3.42. Periodic beach has the 2 m wave length and the 0.3 m amplitude. For this case due to the initial shape, three sections at upwave side and four sections at downwave side were added. Regarding the number of measurement points at each section, six points in the landward direction were added, whereas four points at offshore end were reduced because almost insignificant changes were observed at this region in the previous experiment. The distance between two consecutive points along radii was same as before, 5 cm. The times surveys were conducted were also same as the beach fill case. So, each time 925 points and a total of 3700 points of surveys were required.

Figure 3.42 to Figure 3.45 give the evolution of contours. As mentioned in previous chapter, this plot was distorted from the real data, which was based on the (r, θ) coordinate. Also, longshore distance and cross-shore distance have different scales. One can observe that the contours beyond the depth of 6 cm which corresponds the level of 32 cm, were hardly changed through this experiment and there were not any significant wave migrations in this case as well. Again, the 38 cm lines represent shorelines in each time. One can observe that diffusions of fills were extremely rapid; especially, in first 10 minutes.

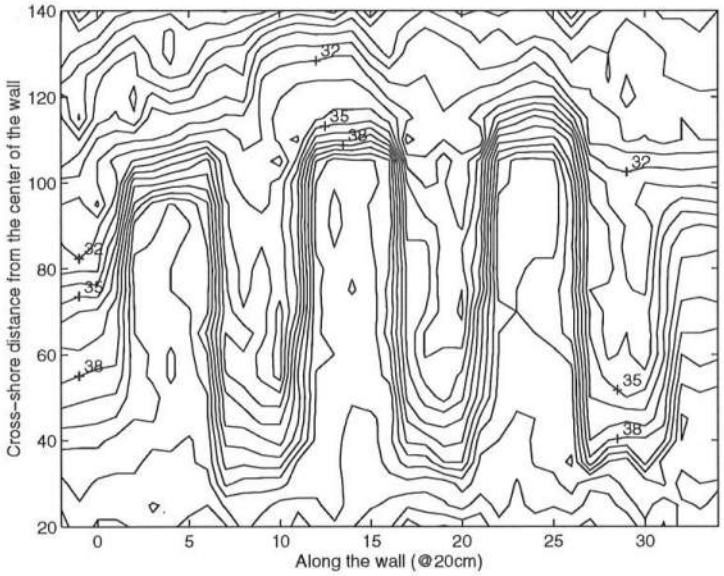

Figure 3.42: Contours at T=0 min (Periodic Beach)

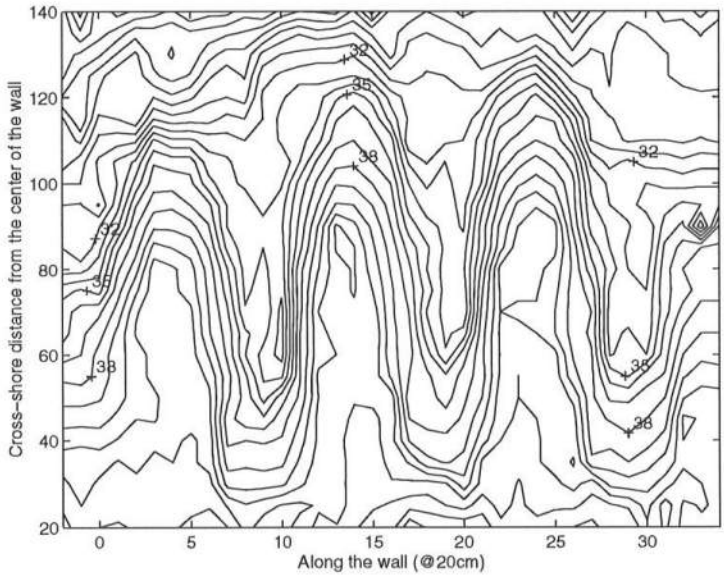

Figure 3.43: Contours at T=3 min (Periodic Beach)

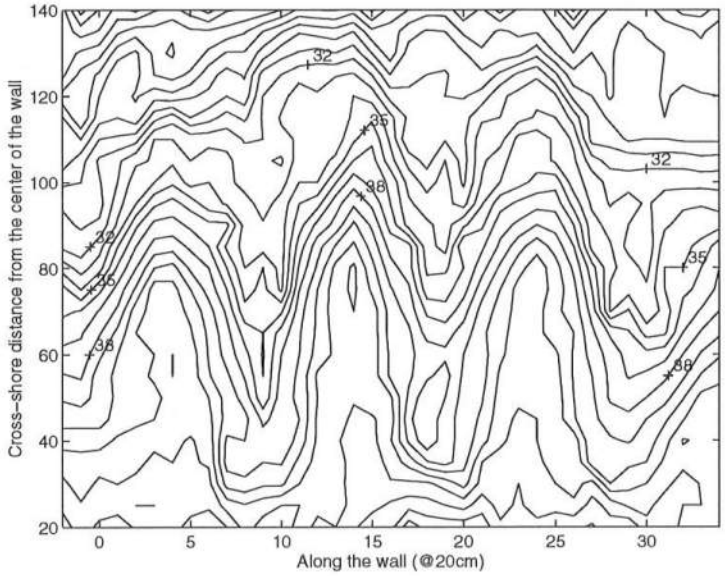

Figure 3.44: Contours at T=10 min (Periodic Beach)

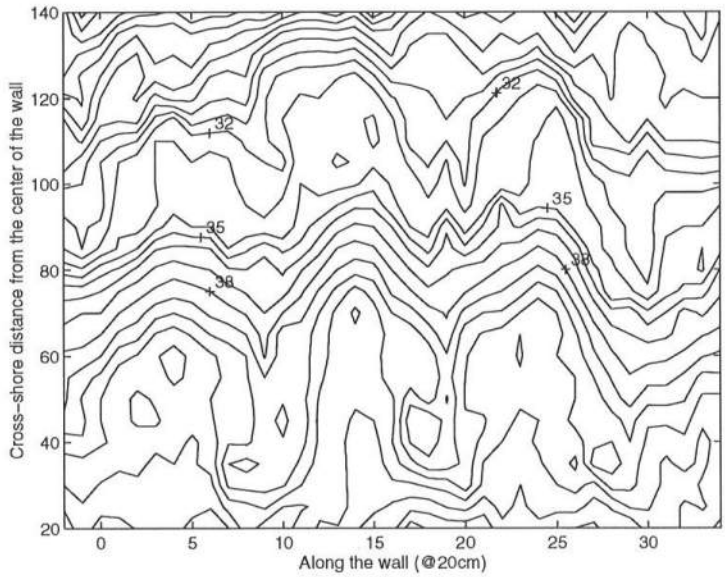

Figure 3.45: Contours at T=20 min (Periodic Beach)

Figure 3.46 to Figure 3.64 show changes of profile at the each section. One can observe significant offshore and onshore transports at some sections which correspond crests and troughs of initial impulsive waves.

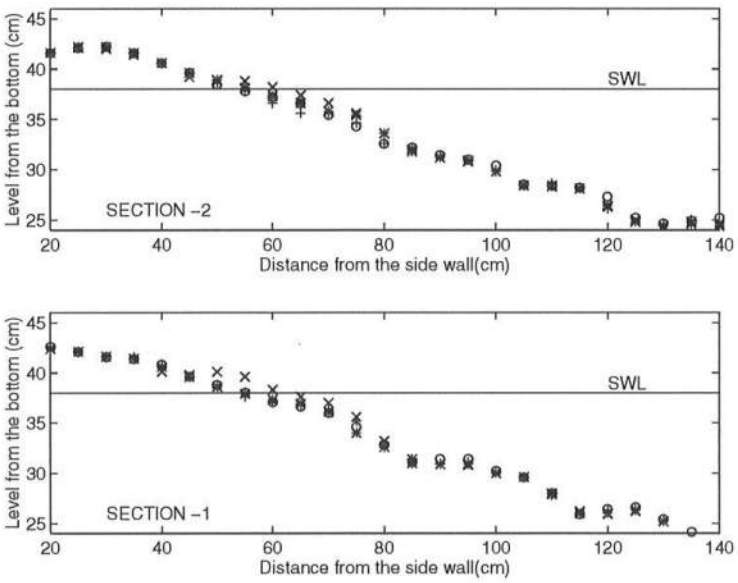

Figure 3.46: Profile changes at Section -2 and Section -1 (Periodic Beach); T=0 min (o), T=3 min (+), T=10 min (*), T=20 min (x)

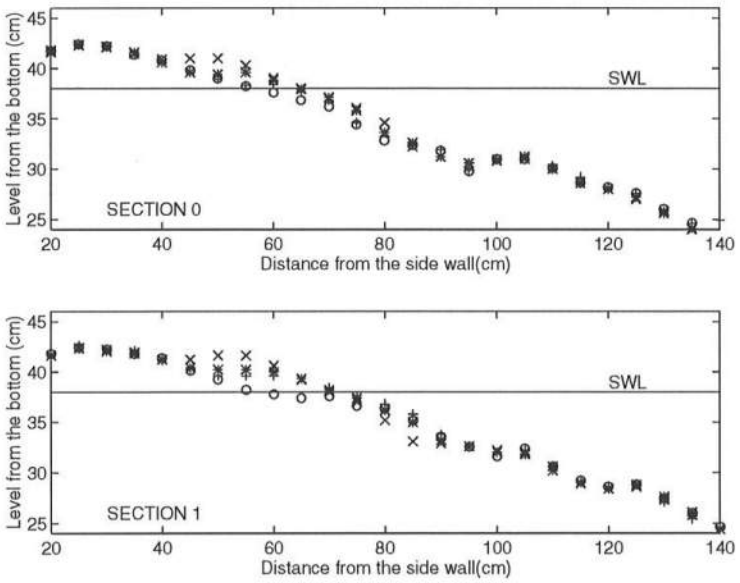

Figure 3.47: Profile changes at Section 0 and Section 1 (Periodic Beach); T=0 min (o), T=3 min (+), T=10 min (*), T=20 min (x)

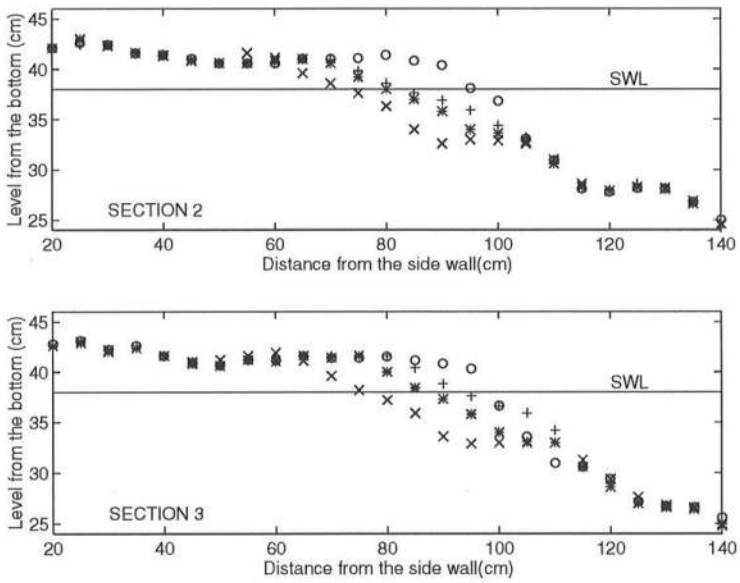

Figure 3.48: Profile changes at Section 2 and Section 3 (Periodic Beach); T=0 min (o), T=3 min (+), T=10 min (*), T=20 min (x)

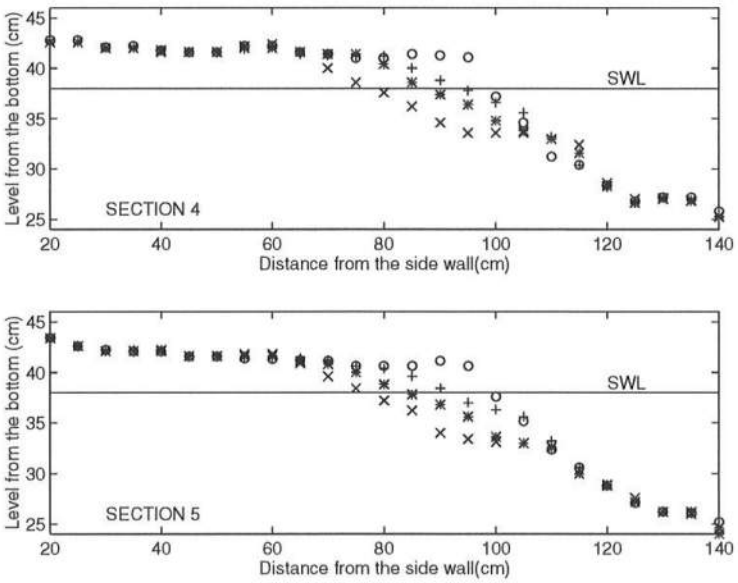

Figure 3.49: Profile changes at Section 4 and Section 5 (Periodic Beach); T=0 min (o), T=3 min (+), T=10 min (*), T=20 min (x)

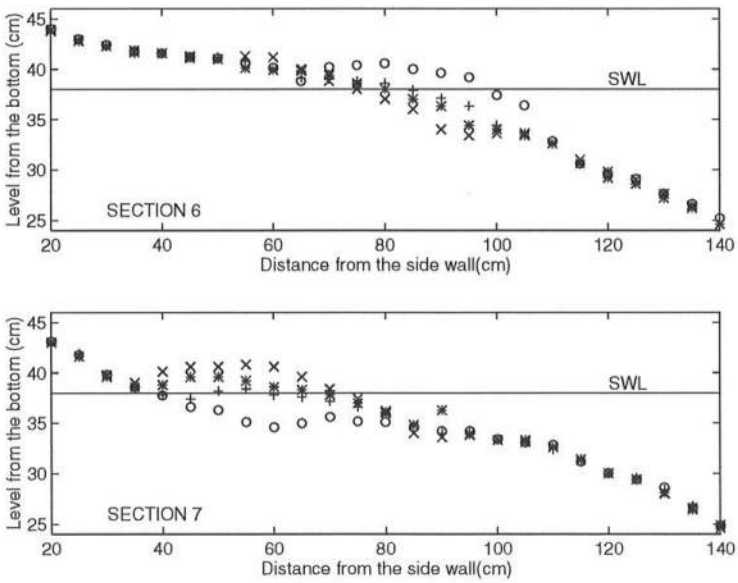

Figure 3.50: Profile changes at Section 6 and Section 7 (Periodic Beach); T=0 min (o), T=3 min (+), T=10 min (*), T=20 min (x)

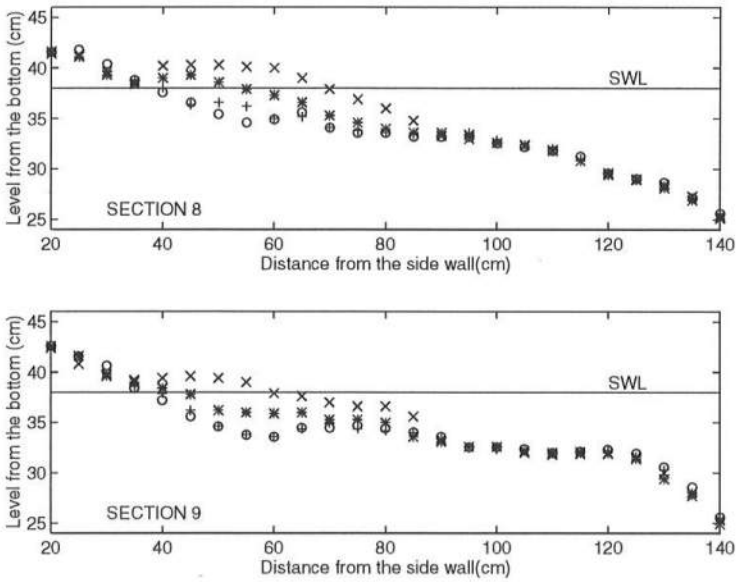

Figure 3.51: Profile changes at Section 8 and Section 9 (Periodic Beach); T=0 min (o), T=3 min (+), T=10 min (*), T=20 min (x)

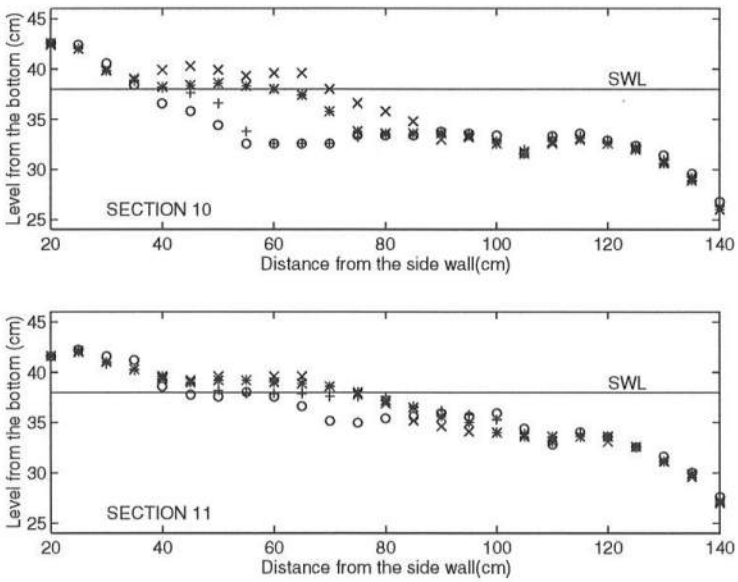

Figure 3.52: Profile changes at Section 10 and Section 11 (Periodic Beach); T=0 min (o), T=3 min (+), T=10 min (*), T=20 min (x)

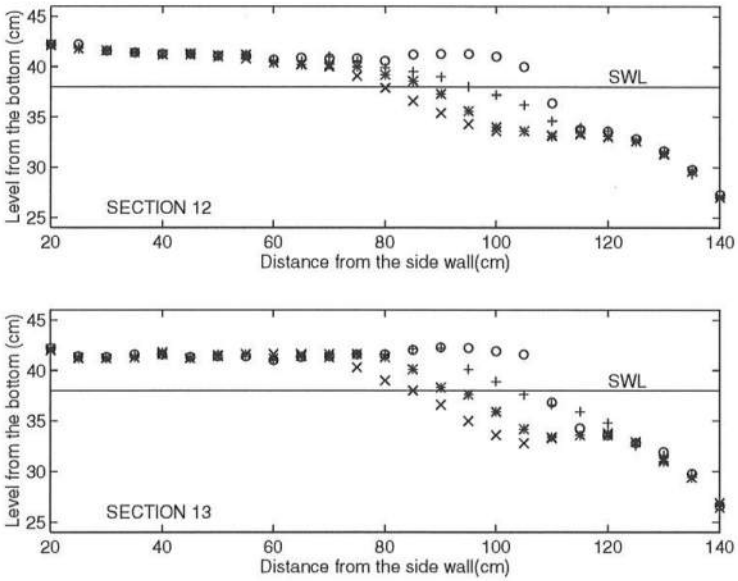

Figure 3.53: Profile changes at Section 12 and Section 13 (Periodic Beach); T=0 min (o), T=3 min (+), T=10 min (*), T=20 min (x)

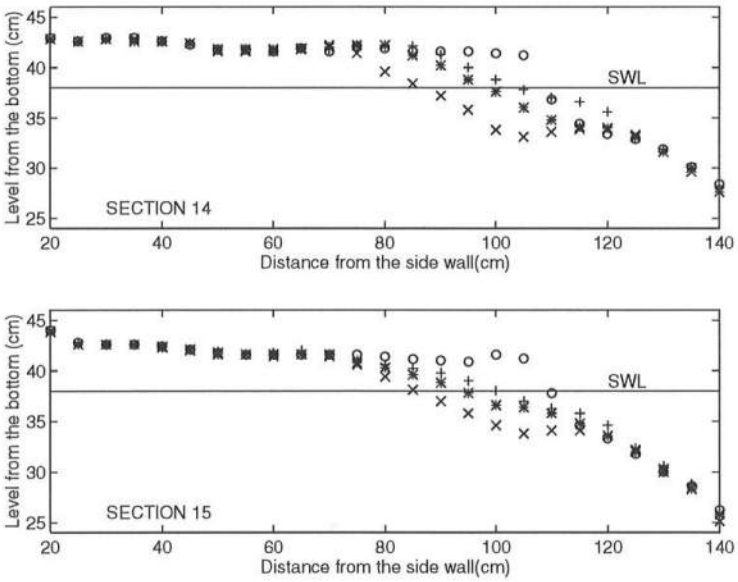

Figure 3.54: Profile changes at Section 14 and Section 15 (Periodic Beach); T=0 min (o), T=3 min (+), T=10 min (*), T=20 min (x)

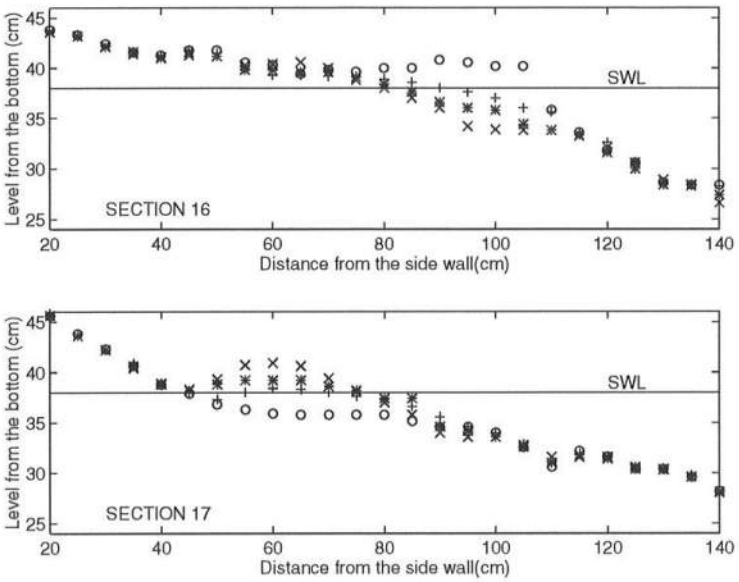

Figure 3.55: Profile changes at Section 16 and Section 17 (Periodic Beach); T=0 min (o), T=3 min (+), T=10 min (*), T=20 min (x)

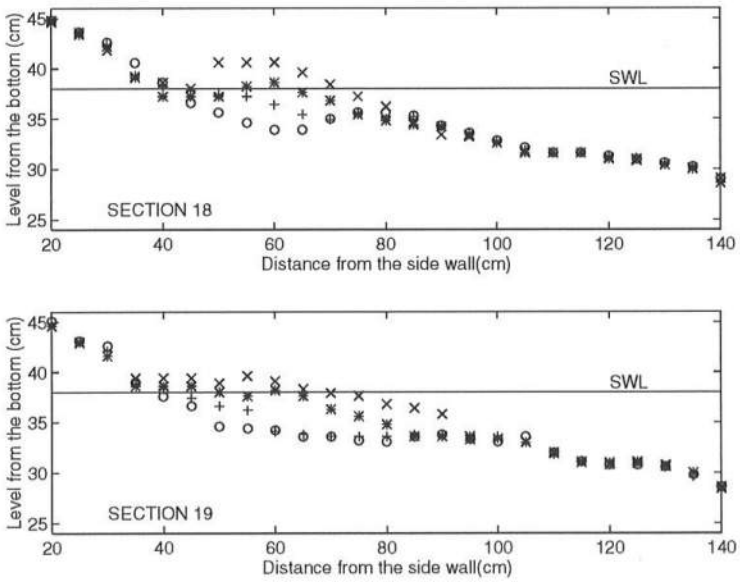

Figure 3.56: Profile changes at Section 18 and Section 19 (Periodic Beach); T=0 min (o), T=3 min (+), T=10 min (*), T=20 min (x)

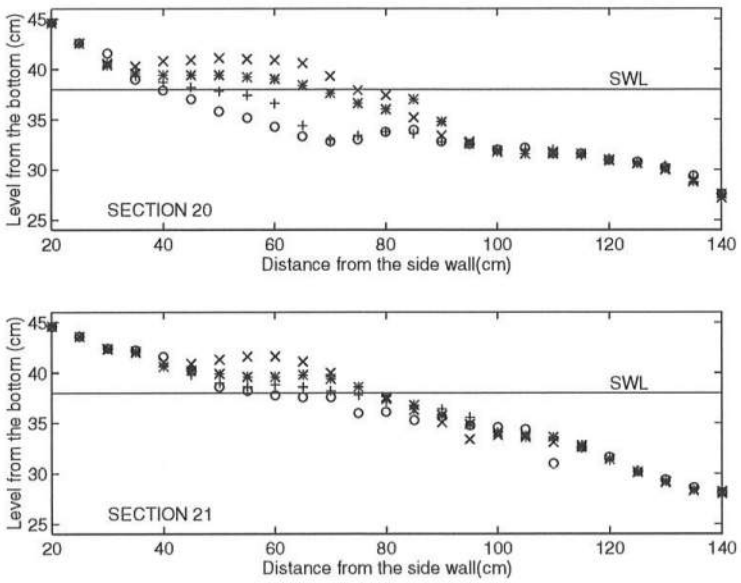

Figure 3.57: Profile changes at Section 20 and Section 21 (Periodic Beach); T=0 min (o), T=3 min (+), T=10 min (*), T=20 min (x)

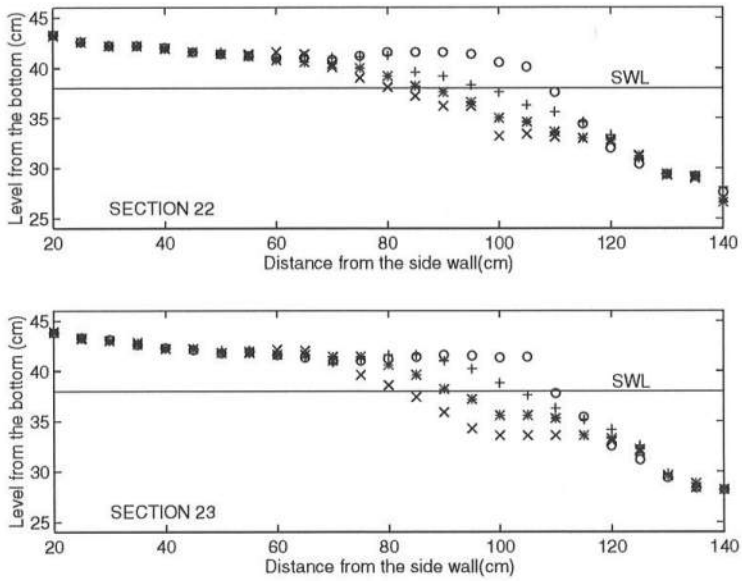

Figure 3.58: Profile changes at Section 22 and Section 23 (Periodic Beach); T=0 min (o), T=3 min (+), T=10 min (*), T=20 min (x)

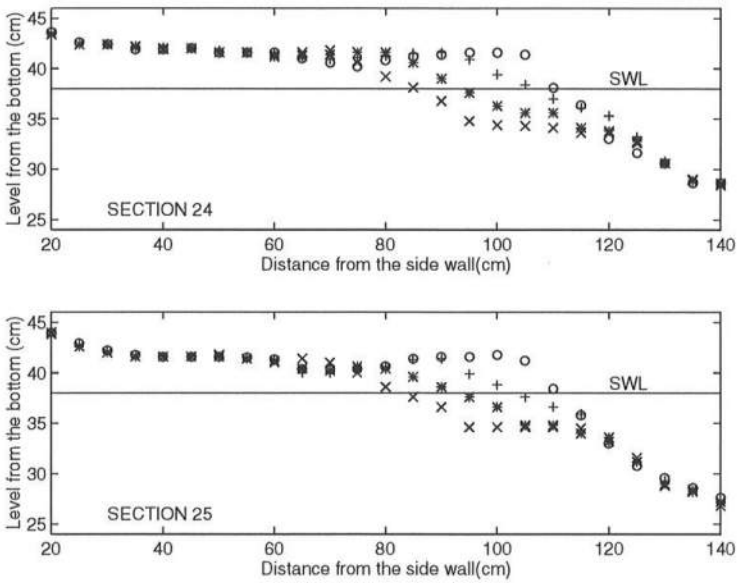

Figure 3.59: Profile changes at Section 24 and Section 25 (Periodic Beach); T=0 min (o), T=3 min (+), T=10 min (*), T=20 min (x)

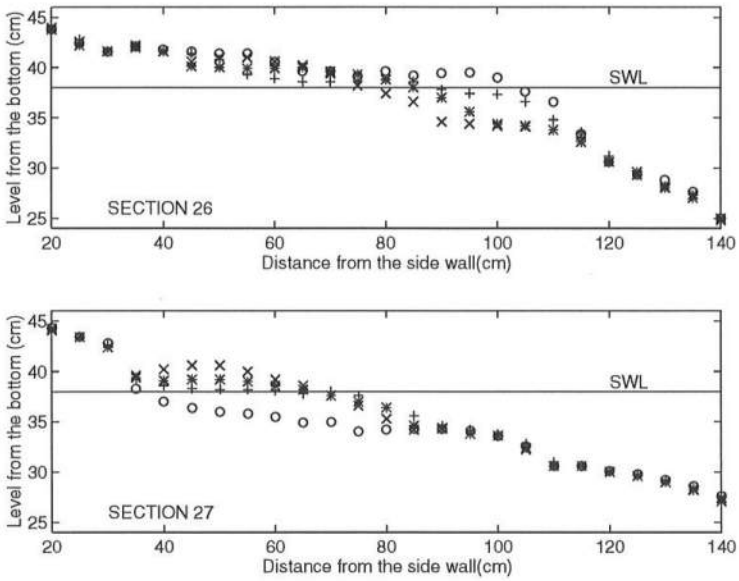

Figure 3.60: Profile changes at Section 26 and Section 27 (Periodic Beach); T=0 min (o), T=3 min (+), T=10 min (*), T=20 min (x)

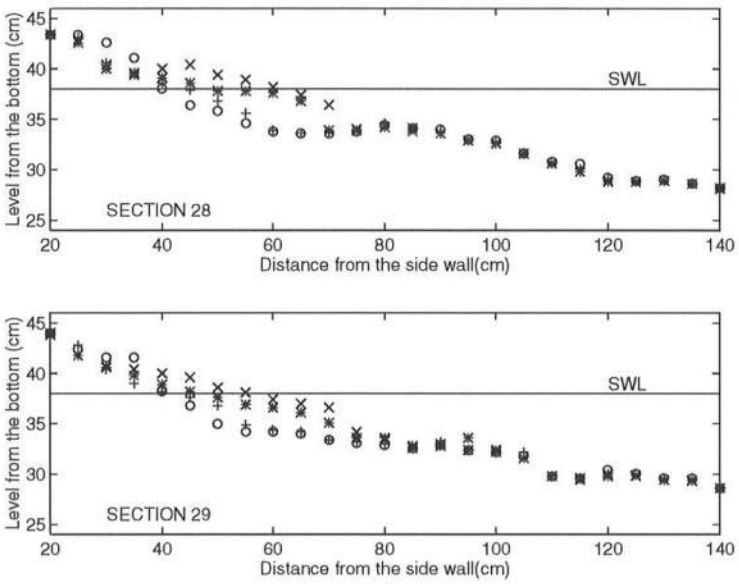

Figure 3.61: Profile changes at Section 28 and Section 29 (Periodic Beach); T=0 min (o), T=3 min (+), T=10 min (*), T=20 min (x)

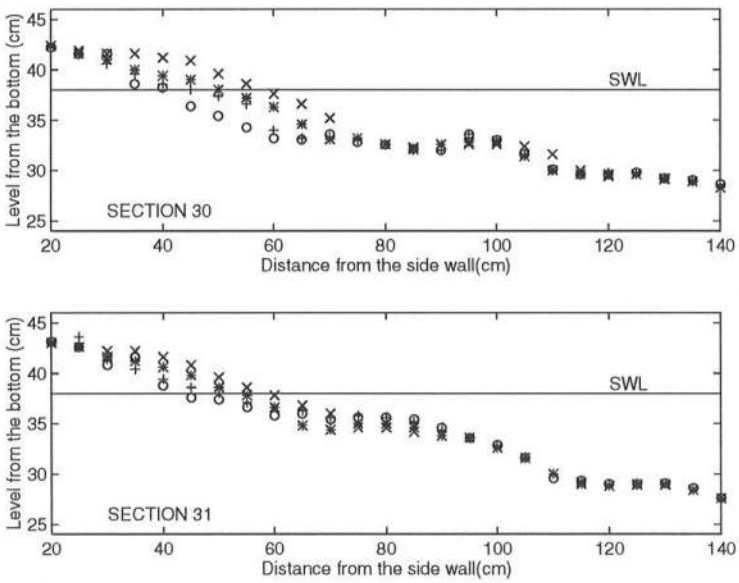

Figure 3.62: Profile changes at Section 30 and Section 31 (Periodic Beach); T=0 min (o), T=3 min (+), T=10 min (*), T=20 min (x)

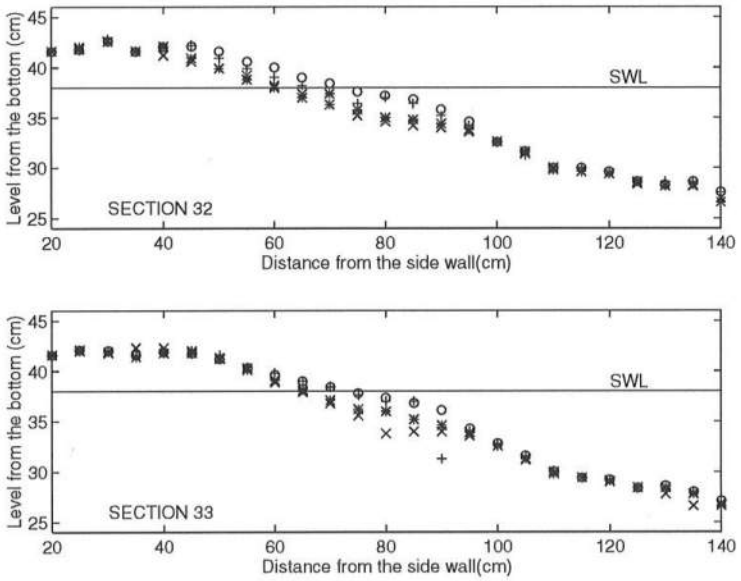

Figure 3.63: Profile changes at Section 32 and Section 33 (Periodic Beach); T=0 min (o), T=3 min (+), T=10 min (*), T=20 min (x)

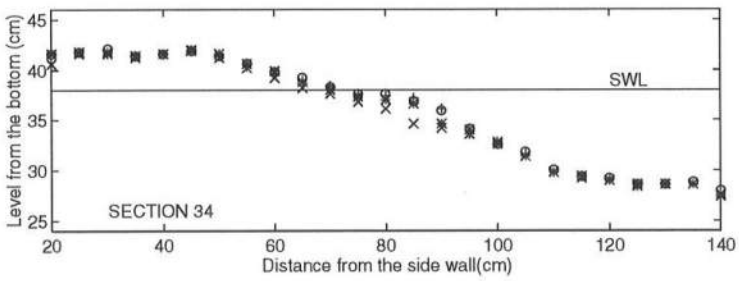

Figure 3.64: Profile changes at Section 34 (Periodic Beach); T=0 min (o), T=3 min (+), T=10 min (*), T=20 min (x)

Chapter 4

NUMERICAL MODEL

Based on the theory of the two-line model with refraction, the nonlinear numerical two-line model with refraction was developed. The linear two-line model was developed by Dalrymple (1997) with the assumption of small angles both for incident wave rays and for slopes of contours in the longshore direction. In this study, that model is improved by removing these restrictions on angles. Furthermore, the nonlinear two-line model now includes the effect of energy density difference at the y_1 contour by using the assumption of the straight wave rays and the "bin method". In this chapter, the procedure used to develop the one-line and two-line models will be reviewed. Numerical results will be discussed and compared with the experimental results and those from the linear model.

4.1 Formulation of the Nonlinear Numerical Model

Since the development of the theory of the two-line model was already introduced in Chapter 2, only the conclusion of the theory will be summarized here. The following set of equations are the governing equations of this model.

$$
\begin{aligned}
D_1 \frac{\partial y_1}{\partial t} &= -Q_y - \frac{\partial Q_1}{\partial x} \\
D_2 \frac{\partial y_2}{\partial t} &= Q_y - \frac{\partial Q_2}{\partial x}
\end{aligned}
$$

where

$$Q_y = k_y(D - D_*)$$

$$Q_1 = C_q \sin 2(\mu_1 - \gamma_1)$$

$$Q_2 = C_q \sin 2(\mu_2 - \gamma_2)$$

For the cross-shore transport the following results from Section 2.2 will be added:

$$D = \frac{5}{16}\gamma\kappa^2 g^{\frac{1}{2}} \bar{h}^{\frac{1}{2}} \frac{\partial h}{\partial x}$$

$$D_* = \frac{5}{16}\gamma\kappa^2 g^{\frac{1}{2}} \bar{h}^{\frac{1}{2}} \left(\frac{\partial h}{\partial x}\right)_*$$

Using the schematized profile as shown in Figure 4.1 the depth h and the beach slope $\partial h/\partial x$ can be approximated as follows:

$$\left(\frac{\partial h}{\partial x}\right) \simeq \frac{(D_1 + D_2)/2}{y_2 - y_1}$$

$$\left(\frac{\partial h}{\partial x}\right)_* \simeq \frac{(D_1 + D_2)/2}{w}$$

$$\bar{h} \simeq D_1$$

Therefore, the equation for the cross-shore transport can be written as:

$$Q = \frac{5}{32} k_y \gamma \kappa^2 g^{\frac{1}{2}} D_1^{\frac{1}{2}} (D_1 + D_2) \left(\frac{1}{y_2 - y_1} - \frac{1}{w}\right) \tag{4.1}$$

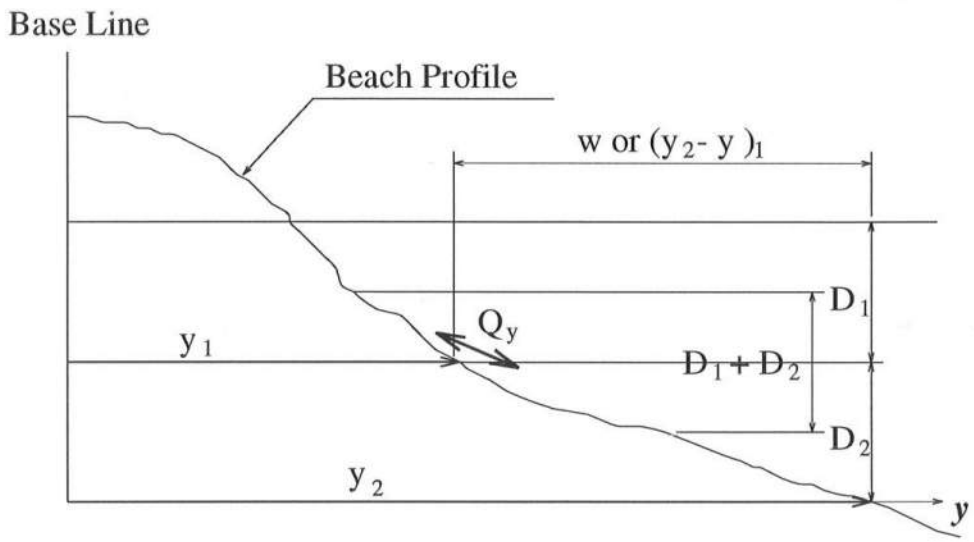

Figure 4.1: Definition of the beach slope in the cross-shore transport model

For longshore transport, the determination of wave angles at each contour and the alongshore slope of the contour were required. The slope of the beach can be calculated using the following two equations which were derived in Chapter 2:

$$\gamma_1 = \arcsin\left(\frac{\frac{\partial y_1}{\partial x}}{\sqrt{1+(\frac{\partial y_1}{\partial x})^2}}\right)$$

$$\gamma_2 = \arcsin\left(\frac{\frac{\partial y_2}{\partial x}}{\sqrt{1+(\frac{\partial y_2}{\partial x})^2}}\right)$$

Meanwhile, Eq. 2.6 was used for computation of μ_1 from μ_2, while μ_2 was calculated from the offshore wave angle by using Snell's law with the shoreline positions y_1 and y_2 defined by the functions f_1 and f_2, respectively. The regularly spaced grid in the longshore direction is shown in Figure 4.2. It was necessary to know the value of the shoreline position for at the all grid points along each contour, so called $y_1(x_i)$, $y_2(x_i)$. Furthermore, additional resolution will be needed for f_1 in order to obtain the spatial lag $\Delta\xi$ by solving for the x value at the intersection

of the straight wave ray and the y_1 contour. The survey data are usually discrete data points, so it is necessary to get an appropriate function f_1 which can interpolate y_1 data reasonably well. In this model the cubic spline curve fitting was adopted to achieve this goal.

The cubic spline is an especially appropriate mathematical tool for curve fitting to discrete data (Gerald, 1978). The method fits a third-order polynomial curve to each interval and can work with regular or irregularly spaced data sets. Furthermore, since each interval has its own third order polynomial function, it is easy to take their derivatives. This is extremely effective when used with the Newton-Raphson technique, which requires the first order derivative of the function. Using this method for the approximation of y_1, the spatial lag $\Delta\xi$ was obtained. Finally, Snell's law from the y_2 to the y_1 contour led to the relationship between μ_1 and μ_2. When the spacing of the two contours is very large, the error in computing the spatial lag $\Delta\xi$ can be quite significant.

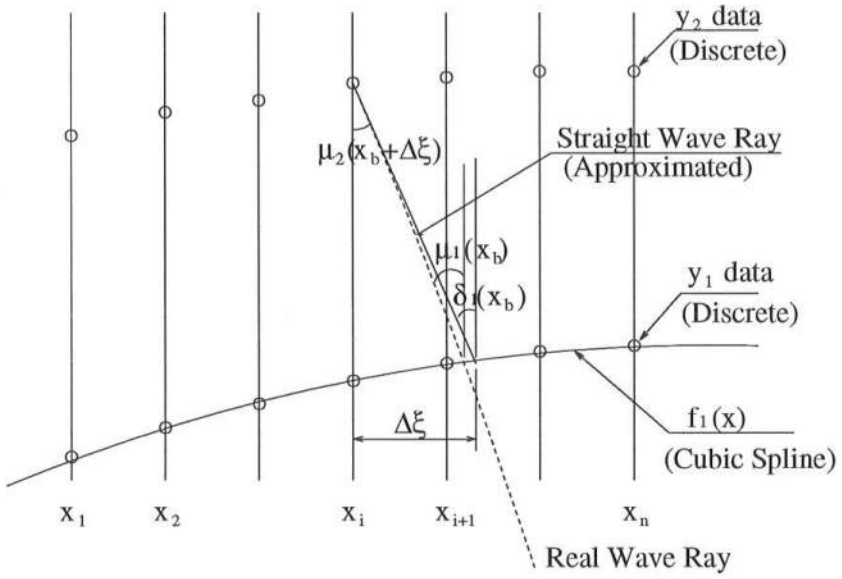

Figure 4.2: Spatial grid and wave rays

4.1.1 Finite Difference Equations

The governing equations are expressed below in finite difference form using a forward-difference scheme in time and a centered-difference scheme in space (Hoffman, 1992).

$$
\begin{aligned}
D_1 \frac{{y_1}^{n+1}{}_i - y^n_{1\,i}}{\Delta t} &= -Q^n_{y_i} - \frac{Q^n_{1\,i+1} - Q^n_{1\,i-1}}{2\Delta x} \\
D_2 \frac{{y_2}^{n+1}{}_i - y^n_{2\,i}}{\Delta t} &= Q^n_{y_i} - \frac{Q^n_{2\,i+1} - Q^n_{2\,i-1}}{2\Delta x}
\end{aligned}
$$

or

$${y_1}^{n+1}{}_i = y^n_{1\,i} - \frac{\Delta t}{D_1} Q^n_{y_i} - \frac{\Delta t}{D_1} \frac{Q^n_{1\,i+1} - Q^n_{1\,i-1}}{2\Delta x} \tag{4.2}$$

$${y_2}^{n+1}{}_i = y^n_{2\,i} + \frac{\Delta t}{D_2} Q^n_{y_i} - \frac{\Delta t}{D_2} \frac{Q^n_{2\,i+1} - Q^n_{2\,i-1}}{2\Delta x} \tag{4.3}$$

where

$$Q^n_{1\,i} = C_q \sin 2(\mu^n_{1\,i} - \gamma^n_{1\,i}) \tag{4.4}$$

$$Q^n_{2\,i} = C_q \sin 2(\mu^n_{2\,i} - \gamma^n_{2\,i}) \tag{4.5}$$

$$\gamma^n_{1\,i} = \arcsin \left[\frac{\left(\frac{\partial y_1}{\partial x}\right)^n_i}{\sqrt{1 + \left(\frac{\partial y_1}{\partial x}\right)^{n\,2}_i}} \right] \tag{4.6}$$

$$\gamma^n_{2\,i} = \arcsin \left[\frac{\left(\frac{\partial y_2}{\partial x}\right)^n_i}{\sqrt{1 + \left(\frac{\partial y_2}{\partial x}\right)^{n\,2}_i}} \right] \tag{4.7}$$

$$\left(\frac{\partial y_1}{\partial x}\right)^n_i = \frac{y^n_{1\,i+1} - y^n_{1\,i-1}}{2\Delta x} \tag{4.8}$$

$$\left(\frac{\partial y_2}{\partial x}\right)^n_i = \frac{y^n_{2\,i+1} - y^n_{2\,i-1}}{2\Delta x} \tag{4.9}$$

Assuming that $f_2(x_i)$ or y_{2i}, the position of the y_2 contour, is known, $\gamma^n_{2\,i}$ can be calculated by using Eq. 4.7. Then, $\mu^n_{2\,i}$ can be obtained by applying Snell's

law with the offshore wave angle. On the other hand, the effect of the spatial lag $\Delta\xi$ on $Q^n_{1\,i}$ has to be considered. First, Eq. 2.6 can be rewritten by using x_b which is the x value at the intersection of the straight wave ray and the y_1 contour as shown in Figure 4.2.

$$x^n_{b\,i} = \tan\mu_2(x^n_i)\{f_2(x_i) - f_1(x^n_{b\,i})\} + x_i$$

Using the assumption of straight wave rays, one may derive the relationship.

$$\delta^n_1(x^n_{b\,i}) = \mu^n_2(x^n_i)$$

Further, applying Snell's law from the y_2 to y_1 contour, one may obtain μ_1 at x_b.

$$\begin{aligned}\mu^n_{1\,bi} &= \arcsin\left[\frac{k_2}{k_1}\sin(\delta^n_{1\,bi} - \gamma^n_{1\,bi})\right] + \gamma^n_{1\,bi} \\ &= \arcsin\left[\frac{k_2}{k_1}\sin(\mu^n_{2\,i} - \gamma^n_{1\,bi})\right] + \gamma^n_{1\,bi}\end{aligned}$$

Here, $\gamma^n_{1\,bi}$ is the slope of the y_1 contour at x_{bi} where the straight wave ray from x_i on the y_2 contour passes over the y_1 contour. $\gamma^n_{1\,bi}$ was calculated by linearly interpolating the $\gamma^n_{1\,i}$. Assuming that $x^n_{b\,i}$ exists between x_i and x_{i+1}, Eq. 4.10 gives the approximation of γ^n_{1bi}.

$$\gamma^n_{1\,bi} = r\gamma^n_{1\,i} + (1-r)\gamma^n_{1\,i+1} \tag{4.10}$$

where r is the ratio of $x^n_{b\,i} - x_i$ to the grid spacing Δx. Then, one can obtain longshore transport at x^n_b as in Eq. 4.11.

$$Q^n_{1\,bi} = C_q \sin 2(\mu^n_{1\,bi} - \gamma^n_{1\,bi}) \tag{4.11}$$

Finally, it is necessary to interpolate $Q^n_{1\,bi}$ to get the values on the regularly spaced grid because those data were needed to carry out the finite difference method.

Cross-shore transport can be written by using Eq. 4.1.

$$Q^n_{y\,i} = K_d\left(\frac{1}{y^n_{2\,i} - y^n_{1\,i}} - \frac{1}{w}\right) \tag{4.12}$$

where

$$K_d = \frac{5}{32} K \gamma \kappa^2 g^{\frac{1}{2}} D_1^{\frac{1}{2}} (D_1 + D_2)$$

Eq. 4.2 and Eq. 4.3 are coupled together through the cross-shore transport term $Q^n_{y_i}$ and the relationship between $\mu^n_{2\,i}$ and $\mu^n_{1\,i}$ in the longshore transport term which is strongly related to the spatial lag $\Delta\xi$.

Since this finite difference scheme is based on the forward-difference scheme in time and the centered-difference scheme in space, basically three data in space at the present time step are required to compute the value at the next time step. However, since this model has the spatial derivative of the longshore transport terms, Q_1 and Q_2 and the temporal derivative of the shoreline positions y_1 and y_2, additional y_1 and y_2 terms will be needed to compute the y_1 and y_2 values at the next time step. Figure 4.3 shows the computational grid using $Q's$. More details about the computation of Q_2 and Q_1 are shown in Figure 4.4. The calculation of Q_2 is relatively straightforward as shown in the upper right figure. Since μ_2 can be calculated from the offshore wave angle δ_o, its value can be considered as constant. Therefore, the computation of $Q^n_{2\,i}$ depends on only that of $\gamma^n_{2\,i}$ and involves $y^n_{2\,i-1}$ and $y^n_{2\,i+1}$. As for Q_1, a different procedure was needed. In the bottom figure in Figure 4.4, $Q^n_{1\,bi}$ indicates longshore transport at x_{bi} on the y_1 contour. The $Q^n_{1\,i}$ are obtained by interpolating from $Q^n_{1\,bi}$. To obtain $x^n_{b\,i}$, all $y^n_{1\,i}$ and $y^n_{2\,i}$ were needed because it was required to solve implicitly for the intersection of the straight wave ray and the y_1 contour. To complete this numerical scheme, two extra points were needed at both ends of the y_1 and y_2 contours.

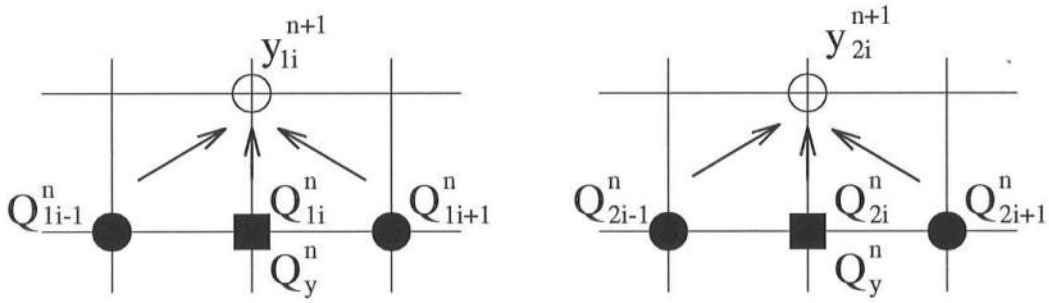

Figure 4.3: The computational diagram of the finite difference scheme (part 1)

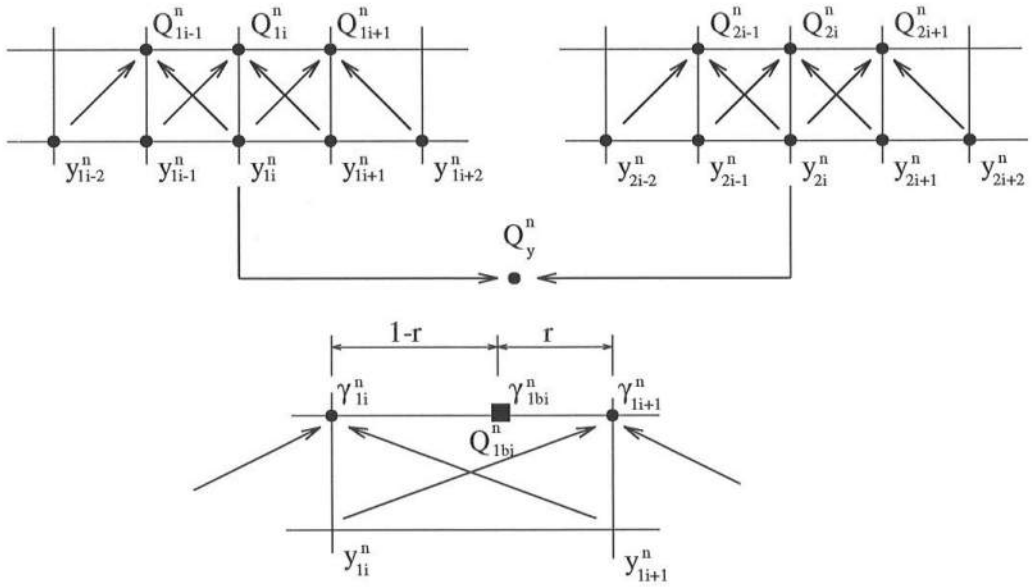

Figure 4.4: The computational diagram of the finite difference scheme (part 2)

4.1.2 Boundary Conditions

The positions of the four extra points for the boundary conditions can be determined by specifying the type of boundary conditions. For instance, the fixed boundary condition can be expressed by assigning values identical to the initial values for every time step.

$$y_1^n(1) = y_1^1(1),\ y_1^n(2) = y_1^1(2),\ y_1^n(N+3) = y_1^1(N+3),\ y_1^n(N+4) = y_1^1(N+4)$$
$$y_2^n(1) = y_2^1(1),\ y_2^n(2) = y_2^1(2),\ y_2^n(N+3) = y_2^1(N+3),\ y_2^n(N+4) = y_2^1(N+4)$$

On the other hand, the periodic boundary condition requires the following relations.

$$y_1^n(1) = y_1^n(N+1),\ y_1^n(2) = y_1^n(N+2),\ y_1^n(3) = y_1^n(N+3),\ y_1^n(4) = y_1^n(N+4)$$
$$y_2^n(1) = y_2^n(N+1),\ y_2^n(2) = y_2^n(N+2),\ y_2^n(3) = y_2^n(N+3),\ y_2^n(4) = y_2^n(N+4)$$

where N is the total number of data points including four extra points for the boundary condition.

4.1.3 Focusing Effect of Longshore Transport Along the y_1 Contour

The directions of wave rays directly depend on the bathymetry in the ocean because of wave refraction effects. In this model, some factors determining the bathymetry are the shape of the y_1 and y_2 contours and their depths. Due to the convex shape of y_2 contour offshore, the spacing of the wave rays passing over that region will narrow. Sometimes rays may even cross under the straight wave ray approximation. In the meantime, the concave y_2 contour makes the spacing increase. As a result, the density of wave energy reaching the y_1 contour is not uniform in the longshore direction. To account for this effect, so called "bin method" was invented for the nonlinear model.

The "bin method" needed a certain number of bins produced by dividing up the computational domain. Assuming that a single straight wave ray coming from each point on the equally spaced grid on the y_2 contour, such rays will travel in a direction which will depend on the shape of the y_2 contour. Since the coefficient of the longshore transport term C_q is proportional to the energy flux, the wave energy is also related to the longshore transport. Therefore, it is natural to superimpose longshore transport contributions, if more than two wave rays come into the same bin. The sign of transport from each bin must be considered to take into account the transport directions so that the sum of values in each bin becomes the net transport for the region. The regular grid spacing dx was chosen as the bin size for this model. In this manner, the focusing effect can be included in this model.

Finally, cubic spline curve fitting is once again used to interpolate the values on the regularly spaced grid because the finite difference scheme needs Q_1 values at all grid points in the computational domain. Unfortunately, approximated Q_1 values were noisy in many cases, leading to significant noise in the final predicted

y_1 contour. A numerical filtering technique applied to the Q_1 data was necessary to solve this problem. The filtering time was examined in many cases, but it was impossible to establish the criteria for an infinite possibility of cases with unlimited geometric and wave conditions. Five-point Shapiro filtering (Shapiro, 1970) was used for this model. This filtering technique is able to remove only relatively small noise so that it retains most of the important information in the original signal.

4.1.4 Stability Analysis

Since this model is nonlinear, there is not a particular method for stability analysis like that for the linear model. Dalrymple (1997) used the following relationship to estimate the proper dt for his linear two-line model which used the Crank-Nicolson method.

$$(dt)_{linear} = \frac{D_1 \Delta x^2}{4q_1} \tag{4.13}$$

where q_1 is defined as:

$$q_1 \equiv 2C_q \frac{k_2}{k_1}$$

On the other hand, since the nonlinear model uses the forward-time centered-space (FTCS) approximation, the next relation, Eq 4.14 can be used to find the proper computational time step, even though it is also the criterion for the linear model.

$$(dt)_{nonlinear} = \frac{1}{4}(dt)_{linear} = \frac{1}{4}\frac{D_1 \Delta x^2}{4q_1} \tag{4.14}$$

It was determined that the nonlinear model still can work under the linear criterion. This relationship includes two parameters, dt and dx. Since dx may affect the resolution of the results, it is recommended to choose a small dx.

4.2 Results

4.2.1 Comparison Between Model Results and Experimental Results

The results from both the nonlinear model and the linear model were compared with the results from two experiments: the single beach fill and three beach fill cases. First of all, it was necessary to determine the contours from the depth measured in the experiment, which were discrete survey points describing the beach profile at each section (see Chapter 3). To accomplish this, the cubic spline curve approximation was applied to interpolate between the data points and find the contour positions which correspond to the depths, D_1 and D_2. After finding those points and plotting them in the same horizontal plane, the cubic spline curve approximation was again used to obtain the contour line passing through them. If the grid sizes in the longshore direction of both the numerical and the physical model were the same, the last procedure would not be needed. The grid size in the physical model was 20 cm, while that in the numerical model could be smaller than this to improve the computational resolution. In this study, 10 cm was used for the grid size in the numerical model.

The comparison was made for two different inshore depths: $D_1 = 1.5\,cm$ and $D_1 = 3.0\,cm$. Table 4.1 shows the all input data used for the numerical computations. In the table, D_1 and D_2 are the inshore and offshore depths, respectively, A is the profile scale factor, H_b is the wave height at the breakerline, δ_o is the incident wave angle with respect to the y axis, T is the wave period, $\mathcal{K}$ is the longshore transport coefficient, C_y is the cross-shore transport coefficient for the linear model, k_y is the cross-shore transport coefficient for the nonlinear model, dx is the spatial grid spacing, and dt is the computational time step. The asterisk denotes the measured values from the experiment. For the initial condition, the data set at $t = 0\,min$ was used directly. Since there is not a

particular method to determine C_y, the values were calibrated to give the best agreement with the experimental data. Two cases were used for the comparison with different depths D_1 to check whether the ratio of the two depths, D_1/D_2 was an important nondimensional parameter, as was indicated by the dimensional analysis for the linear model.

Table 4.1: Input conditions for the comparison with the experimental results.

Conditions	unit	Case 1	Case2
D_1	cm	1.5*	3.0*
D_2	cm	3.0*	3.0*
A	$m^{\frac{1}{3}}$	0.1*	0.1*
H_b	cm	1.8*	1.8*
δ_o	$degree$	13.3*	13.3*
T	sec	0.98*	0.98*
$\mathcal{K}$	--	1.01*	1.01*
C_y	m/day	1.0	1.0
k_y	m^4/N	2.2×10^{-6}	2.2×10^{-6}
dx	m	0.1	0.1
dt	sec	15.3	25.0

Figure 4.5 and Figure 4.6 show the results of comparisons for the beach fill of case 1, which has the shallower inshore depth. As one can see, both the linear and the nonlinear model had relatively good agreement with the experimental data except the y_2 contour at t = 20 min. Figure 4.7 and Figure 4.8 show the results of the single beach fill of case 2. The agreement became a little worse, especially the result at t = 3 min.

Figure 4.9 and Figure 4.10 show the results of comparisons for the periodic beach of case 1. In this case, the linear model seemed to decay much faster than the experiment using same value as the beach fill case for C_y, while the nonlinear model still showed very good agreement with the experiment. Finally, Figure 4.11 and Figure 4.12 show the results from the the periodic beach of case 2. Once again, the agreement at t = 3 min became worse. Otherwise, results were still relatively good.

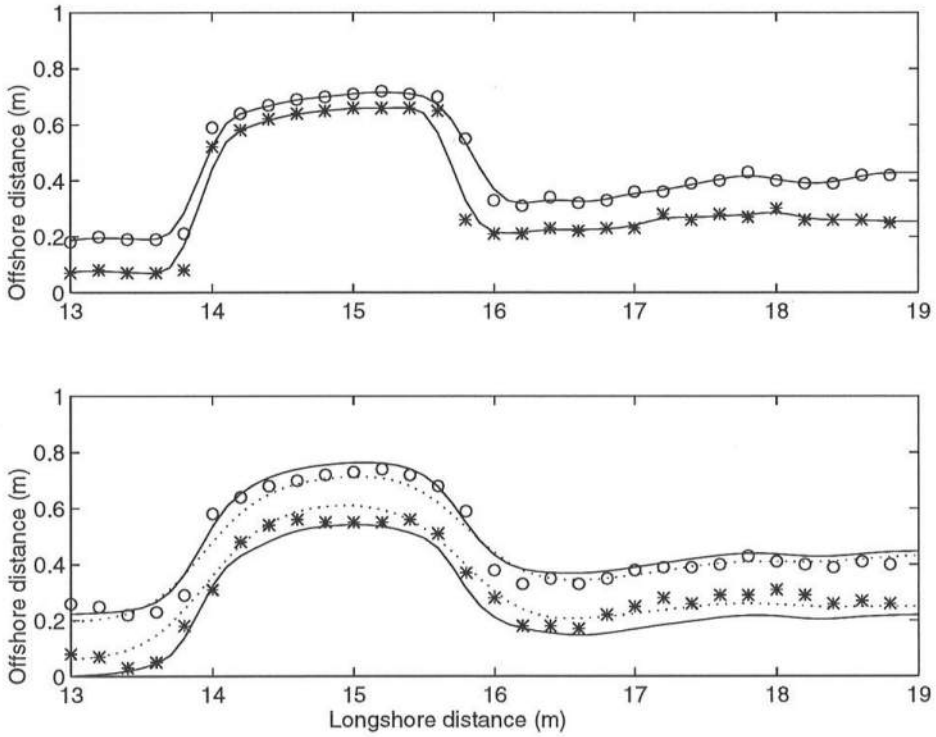

Figure 4.5: Comparison between the experimental result and the numerical result at $T = 0\ min$ (upper) and $T = 3\ min$ (lower). Circle, y_1 data; star, y_2 data; solid line, nonlinear result; dotted line, linear result. (Beach Fill; case 1)

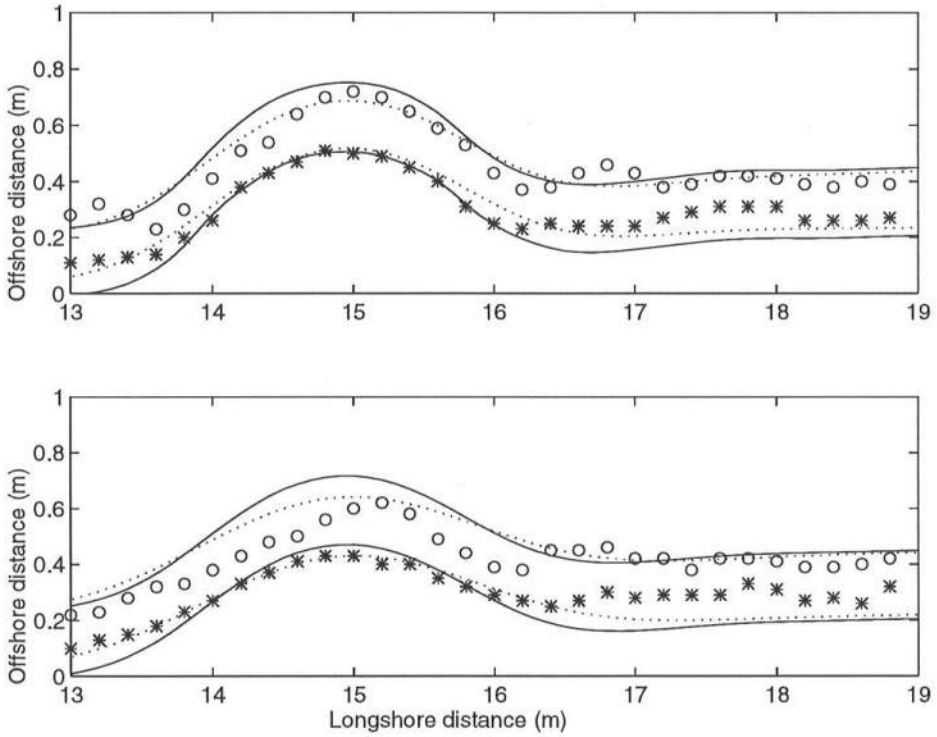

Figure 4.6: Comparison between the experimental result and the numerical result at $T = 10\ min$ (upper) and $T = 20\ min$ (lower). Circle, y_1 data; star, y_2 data; solid line, nonlinear result; dotted line, linear result. (Beach Fill; case 1)

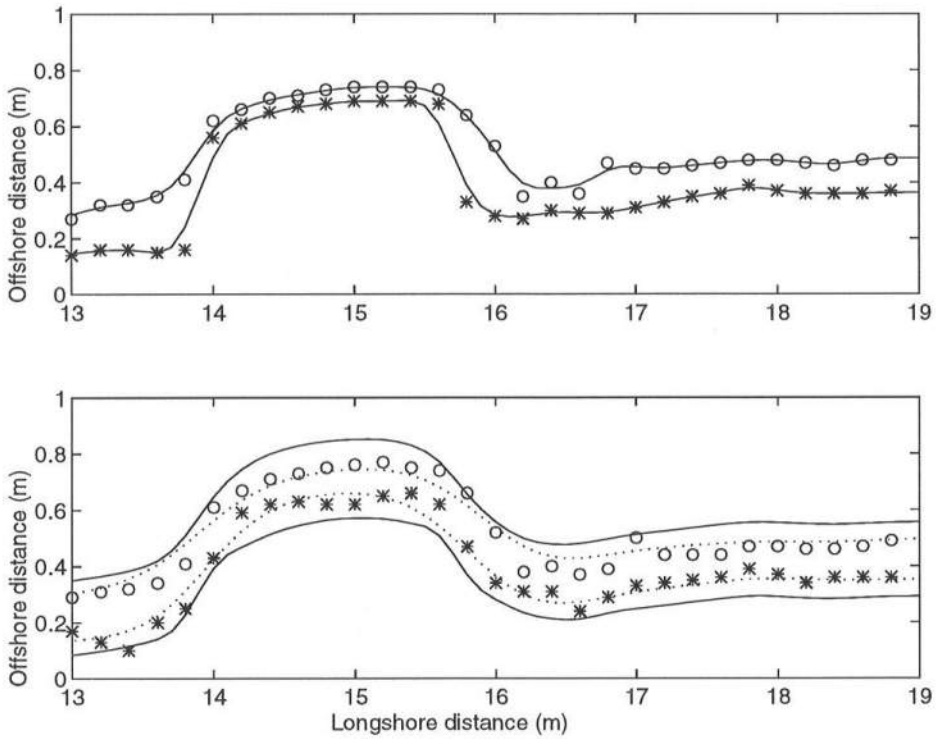

Figure 4.7: Comparison between the experimental result and the numerical result at $T = 0\ min$ (upper) and $T = 3\ min$ (lower). Circle, y_1 data; star, y_2 data; solid line, nonlinear result; dotted line, linear result. (Beach Fill; case 2)

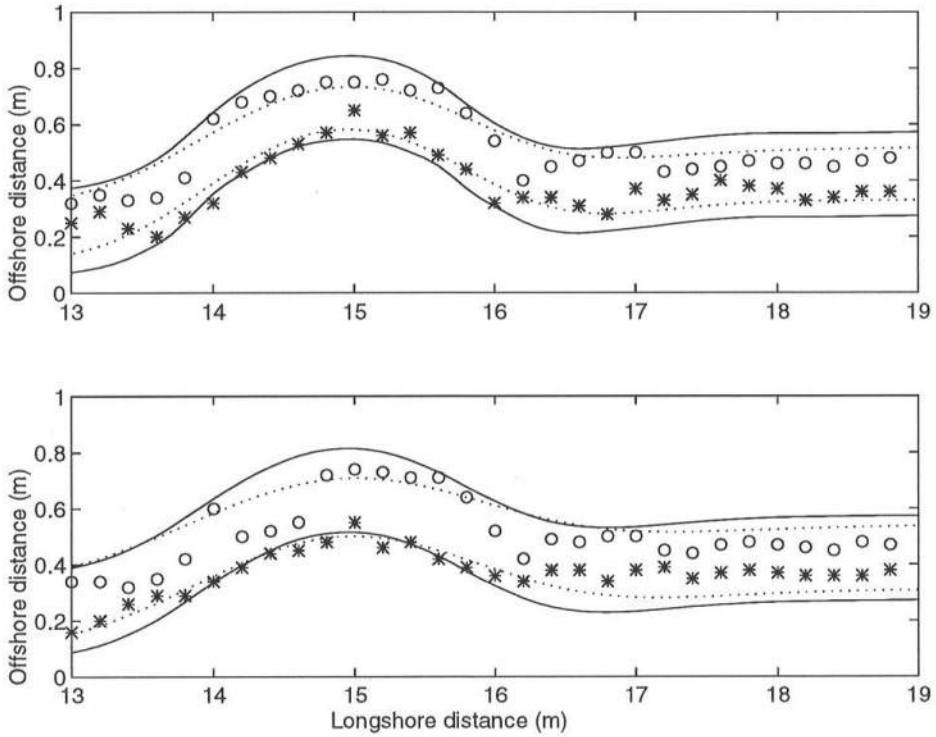

Figure 4.8: Comparison between the experimental result and the numerical result at $T = 10\ min$ (upper) and $T = 20\ min$ (lower). Circle, y_1 data; star, y_2 data; solid line, nonlinear result; dotted line, linear result. (Beach Fill; case 2)

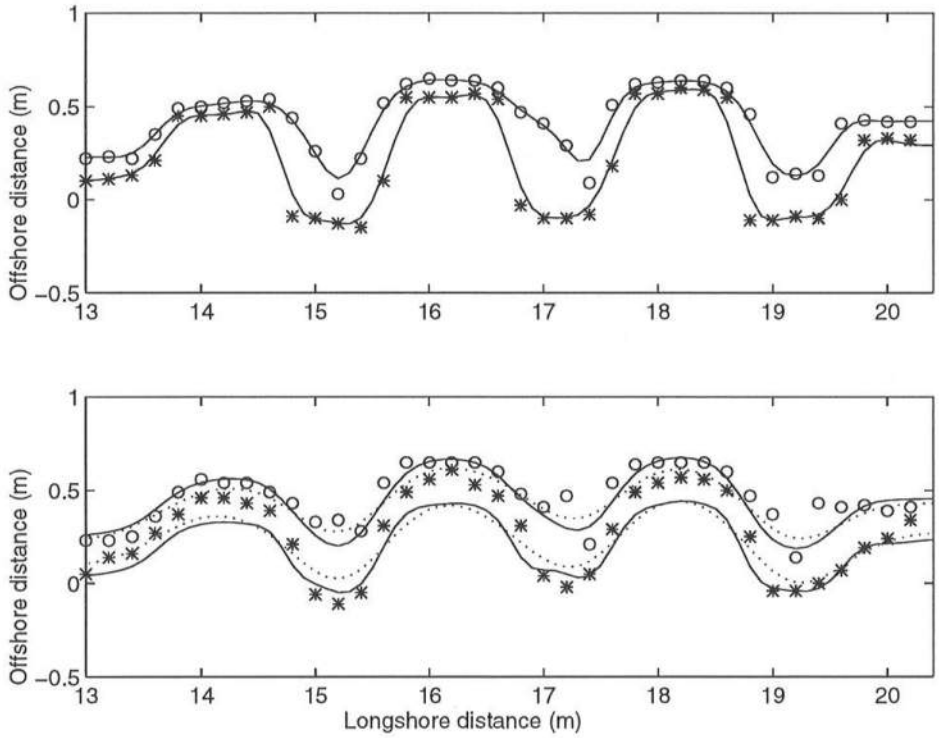

Figure 4.9: Comparison between the experimental result and the numerical result at $T = 0\ min$ (upper) and $T = 3\ min$ (lower). Circle, y_1 data; star, y_2 data; solid line, nonlinear result; dotted line, linear result. (Periodic Beach ; case 1)

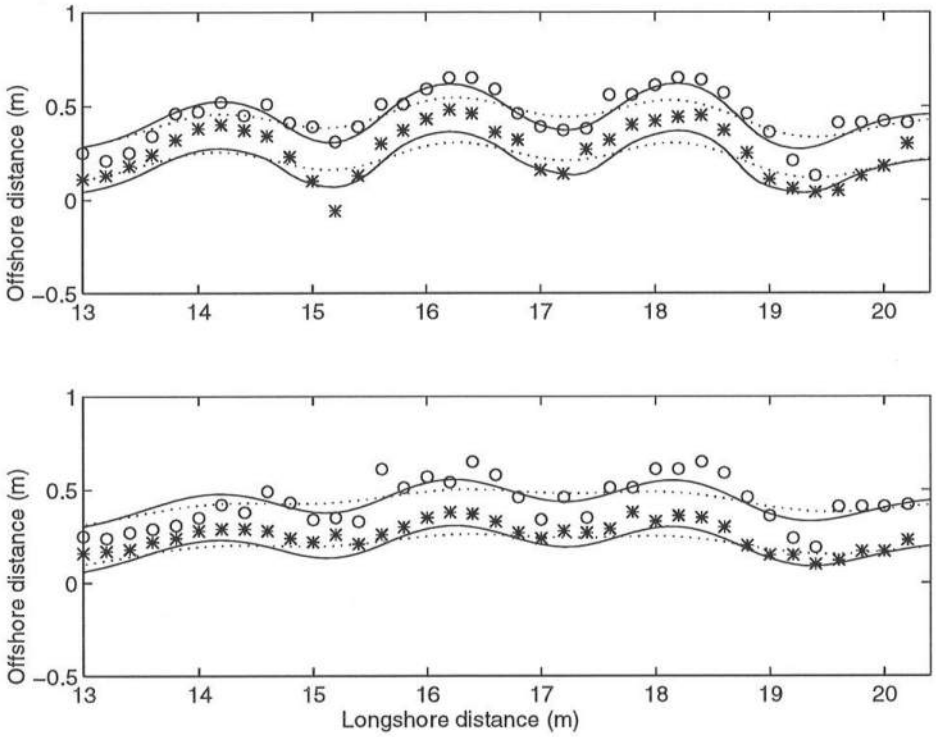

Figure 4.10: Comparison between the experimental result and the numerical result at $T = 10\ min$ (upper) and $T = 20\ min$ (lower). Circle, y_1 data; star, y_2 data; solid line, nonlinear result; dotted line, linear result. (Periodic Beach; case 1)

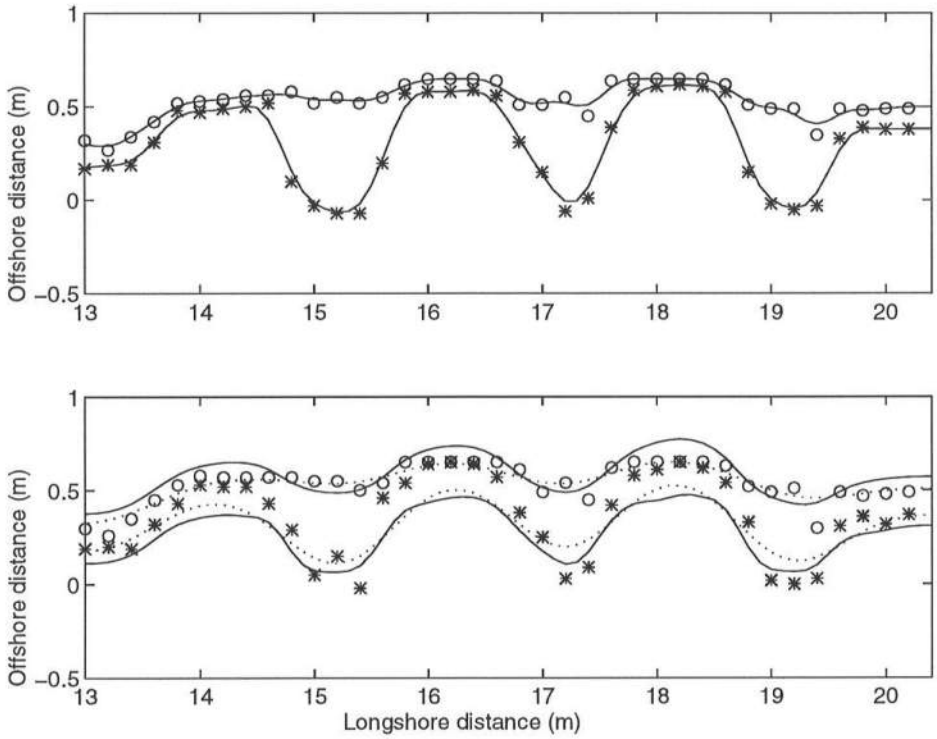

Figure 4.11: Comparison between the experimental result and the numerical result at $T = 0$ *min* (upper) and $T = 3$ *min* (lower). Circle, y_1 data; star, y_2 data; solid line, nonlinear result; dotted line, linear result. (Periodic Beach ; case 2)

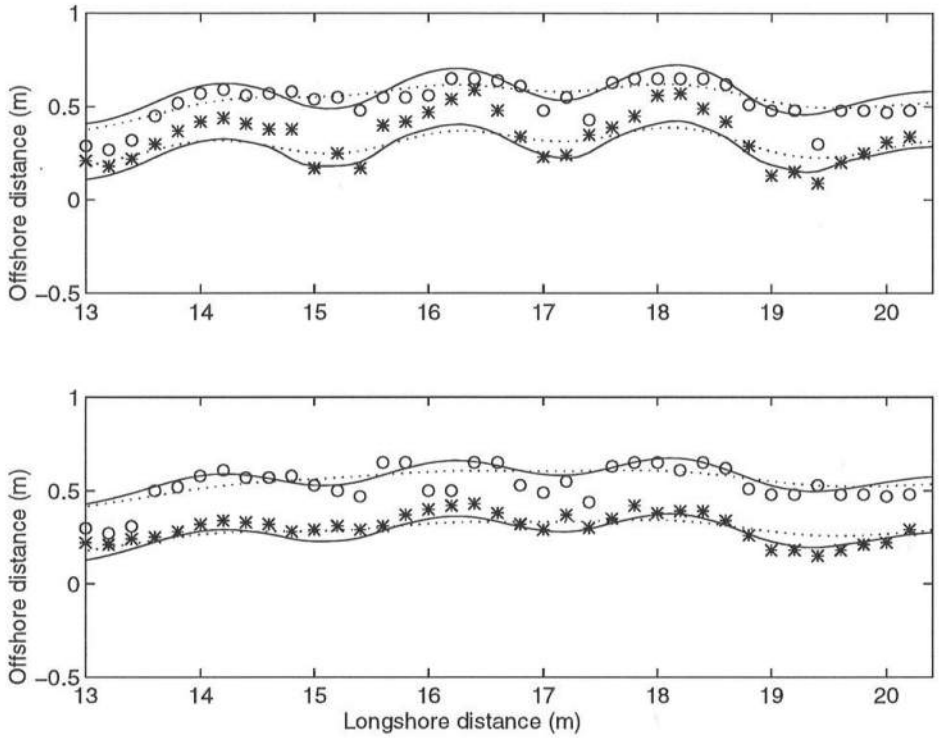

Figure 4.12: Comparison between the experimental result and the numerical result at $T = 10\ min$ (upper) and $T = 20\ min$ (lower). Circle, y_1 data; star, y_2 data; solid line, nonlinear result; dotted line, linear result. (Periodic Beach ; case 2)

4.2.2 Solitary Wave

In the comparison with experimental data, it was impossible to observe effects from wave refraction because of the small scale geometry. Below are some results from both the nonlinear and the linear numerical model which use solitary wave shaped contours for their initial conditions. The amplitude of the solitary wave was 200 m and the wave length was 5000 m. Table 4.2 shows input data for these cases. "Regular slope" in Table 4.2 implies the beach profile with the sediment scale parameter, $A = 0.1$, which is the common value for many beaches. Likewaise, "Mild slope" means that for $A = 0.01$. The parametric analysis for the incident wave angle was made using this slope.

Table 4.2: Input conditions for solitary wave cases

Conditions	unit	Mild slope	Regular slope
D_1	m	3.0	3.0
D_2	m	6.0	6.0
A	$m^{\frac{1}{3}}$	0.01	0.1
H_b	m	0.5	0.5
δ_o	$degree$	0, 10, 30	0, 30
T	sec	10	10
$\mathcal{K}$	--	0.77	0.77
C_y	m/day	5.12×10^{-5}	0.05
k_y	m^4/N	2.2×10^{-6}	2.2×10^{-6}
dx	m	50	50
dt	day	2	2

Dalrymple found that sand waves may migrate only on a very mildly sloped beach (1997a). The first comparison was made with this type of beach. Figure 4.13, Figure 4.17 and Figure 4.21 show the evolutions of contours predicted by the linear model. Figure 4.14, Figure 4.18 and Figure 4.22 show results from the nonlinear model. The linear model gives the migration with some angle of incident wave. For the large incident wave angle 30^o, the amplitudes of contours increased once, then propagated with the gradual decay. The result from nonlinear model does not shows remarkable migrations, instead, it shows the focusing effect with hot spots on the downwave position of the solitary wave shaped contour. The location of the hot spots was different depending on the incident wave angle. Figure 4.15, Figure 4.19 and 4.23 may be able to explain this phenomenon. These figures depict the approximated straight wave rays. By looking at these figures, one can see how some wave rays are concentrated in one spot and how the spots move when the incident wave angle is changed.

Some artificial rays are entering the computational domain from the left side. These rays are necessary especially when one must examine large incident wave angles. If wave angles are too large, there will be very few or possibly no points for the intersection of the rays and the y_1 contour in the computational domain. Then it becomes impossible to calculate the rate of longshore transport along the y_1 contour. In this model, there is a fake domain outside and to the left of the computational domain. For the fixed boundary condition, both the y_1 and y_2 contours in this region are just straight and parallel to the shoreline with values at left end of the real domain. On the other hand, for the periodic boundary condition, the same data as those in the real computational domain are used for the hypothetical contours.

Figure 4.16, Figure 4.20 and 4.24 show approximations of longshore transport at the y_1 contour. The upper figures indicate the raw data of longshore transport at the y_1 contour calculated from approximated straight wave rays. The longshore positions of those points indicates the points where the rays arrive from regularly spaced grid points on the y_2 contour. As a result, the raw data are not only irregularly spaced in the longshore direction, but also not in order. Due to the focusing effect, some regions have higher density of points which implies greater longshore transport. The middle diagram in each figure explains the results obtained after using the "bin method". At this point, the sequence of data sets becomes properly ordered and each regular grid point has one corresponding data point. After the longshore transport contributions are summed in each bin dx and interpolated by using the cubic spline curve approximation, the results unfortunately tend to have a small amount of noise. The wavelength of that noise tends to be much smaller than the wavelength of the water waves. Practically speaking, the straight wave ray approximation may cause a big error under the conditions like large spacing of contours. Also, wave diffraction may play a part in smoothing out wave crests. Therefore, this noises must be filtered out to obtain reasonably smooth contours. After applying Shapiro filtering, one may obtain the bottom diagram in each figure. By using Shapiro filtering, it is possible to retain more information from the original signal despite the 50 repetitions of numerical filtering. However, in order to obtain relatively smooth contours, some important information were filtered out as shown in Figure 4.16, Figure 4.20 and 4.24.

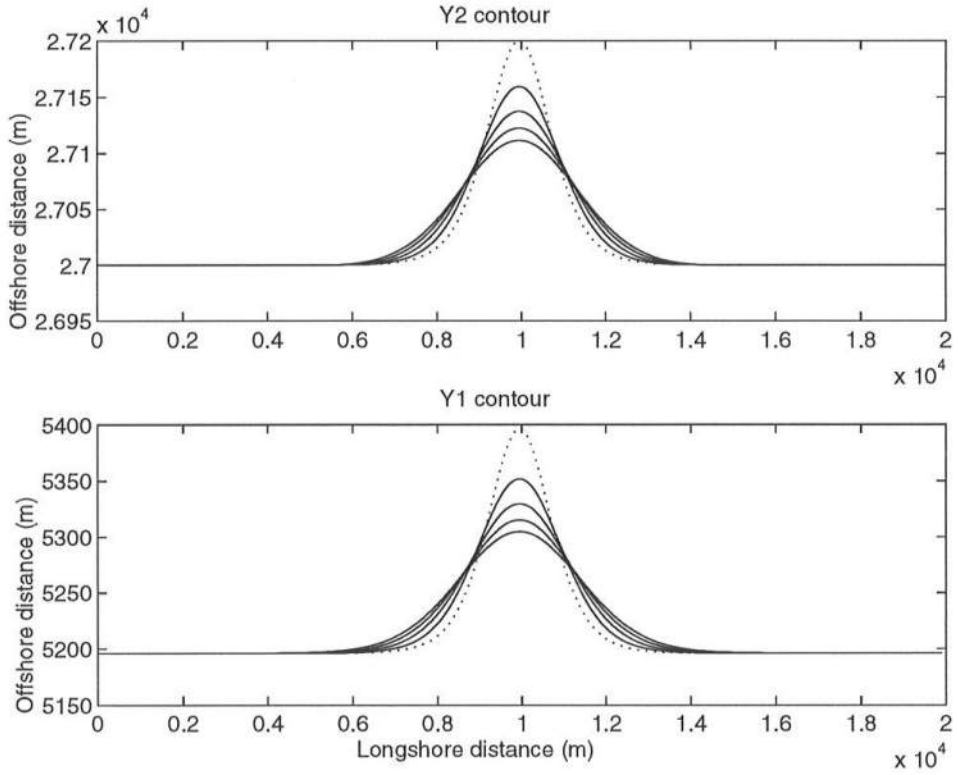

Figure 4.13: Evolution of y_1 and y_2 contours for incident wave angle 0^o on the mild slope ($A = 0.01$) at t=1, 2, 3, and 4 years. Solid line, linear model; dotted line, initial contour. (Solitary Wave).

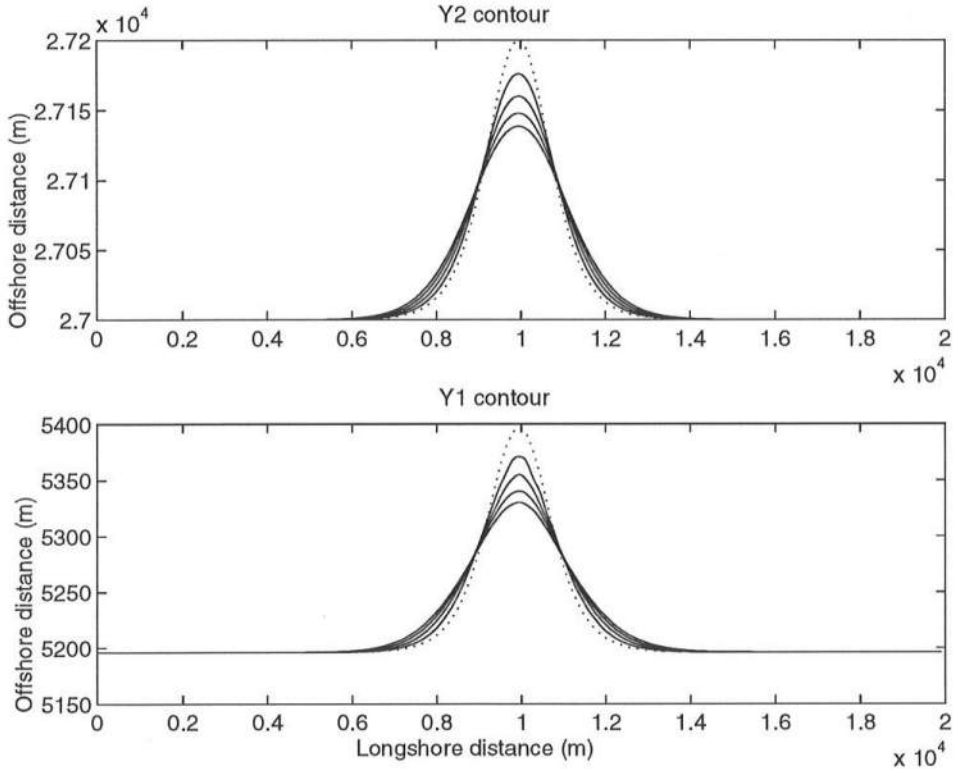

Figure 4.14: Evolution of y_1 and y_2 contours for incident wave angle 0^o on the mild slope ($A = 0.01$) at t=1, 2, 3, and 4 years. Solid line, nonlinear model; dotted line, initial contour. (Solitary Wave).

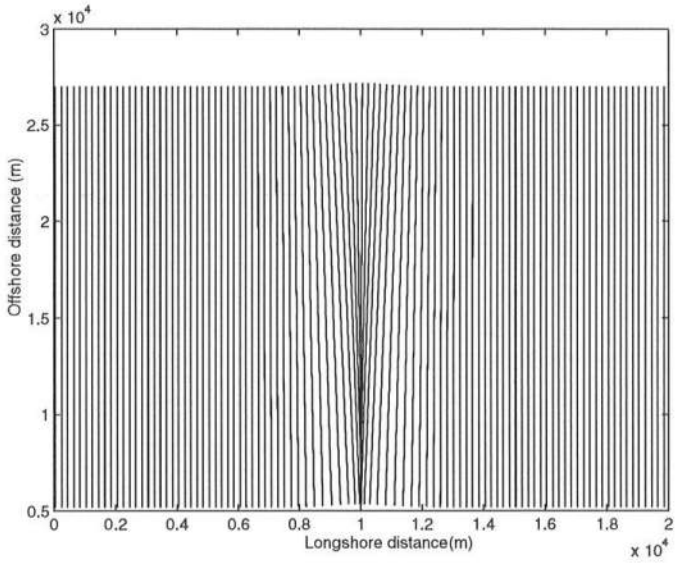

Figure 4.15: Approximated straight wave rays for incident wave angle 0^o on the mild slope ($A = 0.01$) at t=1 year. (Solitary Wave)

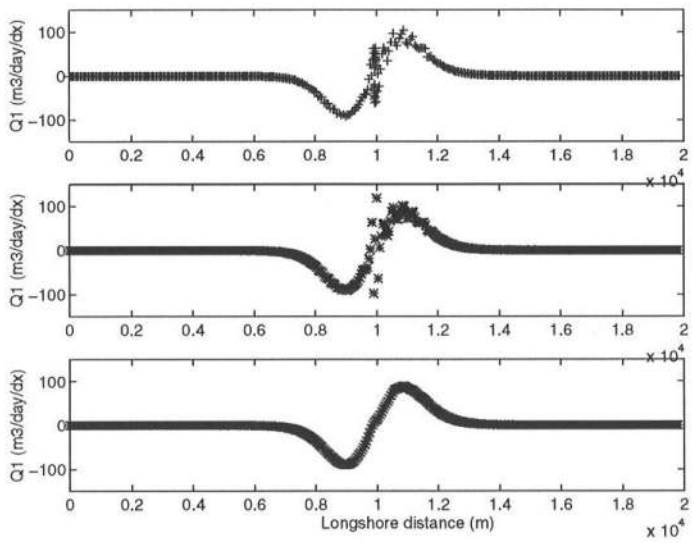

Figure 4.16: Approximation of longshore transport at y_1 contour for incident wave angle 0^o on the mild slope ($A = 0.01$) at t=1 year. Upper, raw data; middle, after bin method; lower, final result after filtering. (Solitary Wave)

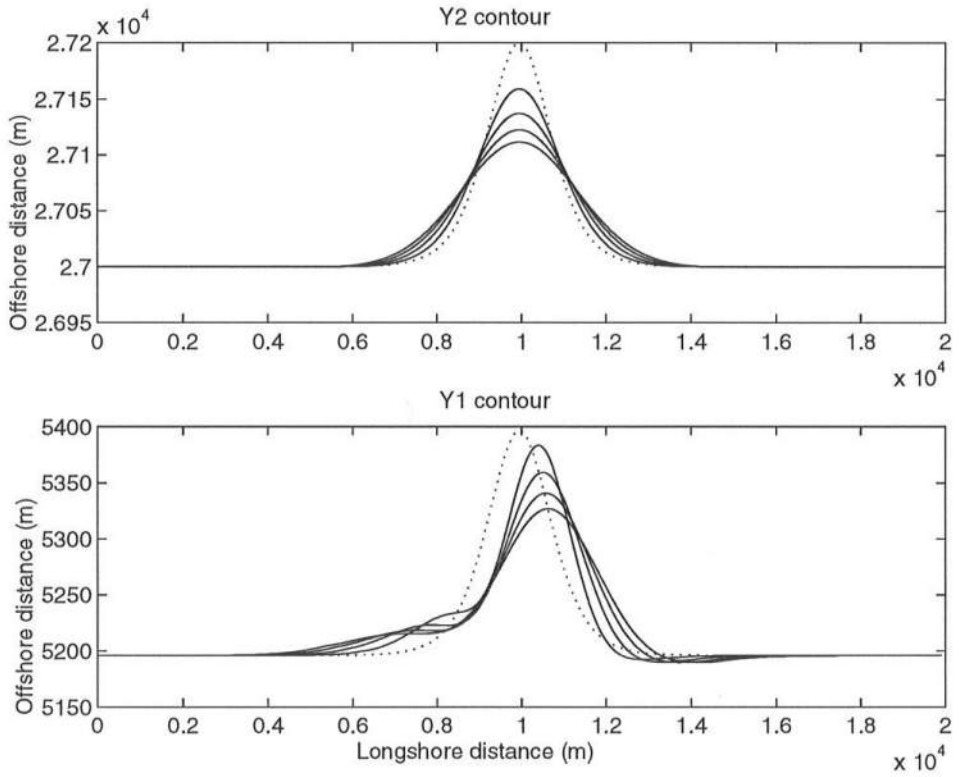

Figure 4.17: Evolution of y_1 and y_2 contours for incident wave angle 10^o on the mild slope ($A = 0.01$) at t=1, 2, 3, and 4 years. Solid line, linear model; dotted line, initial contour. (Solitary Wave).

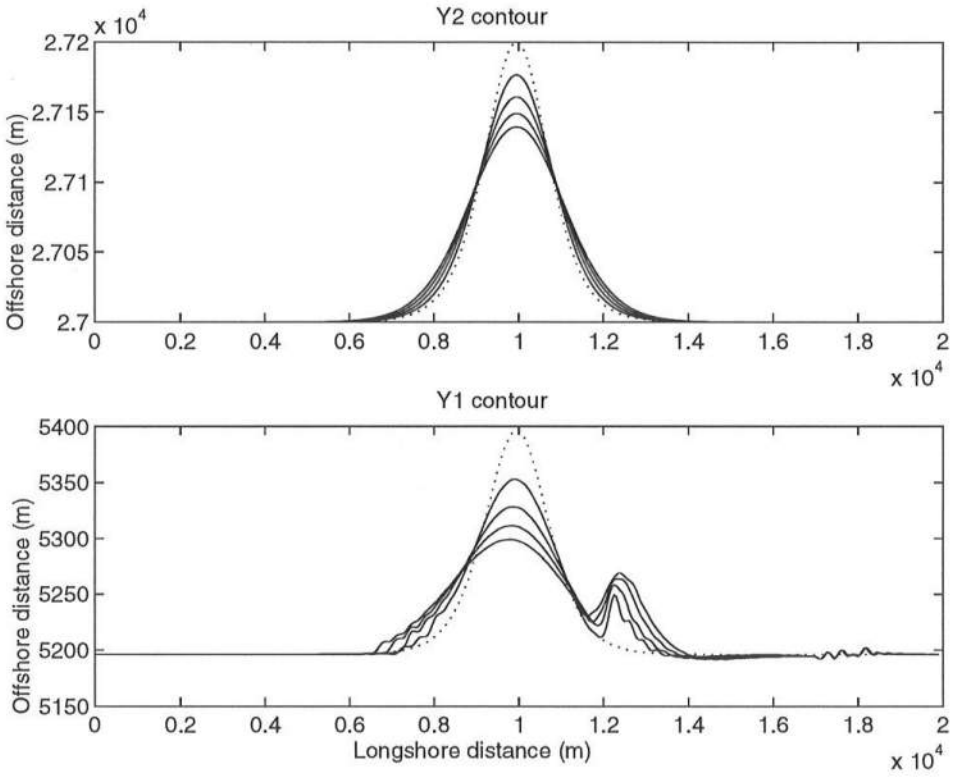

Figure 4.18: Evolution of y_1 and y_2 contours for incident wave angle 10^o on the mild slope ($A = 0.01$) at t=1, 2, 3, and 4 years. Solid line, nonlinear model; dotted line, initial contour. (Solitary Wave).

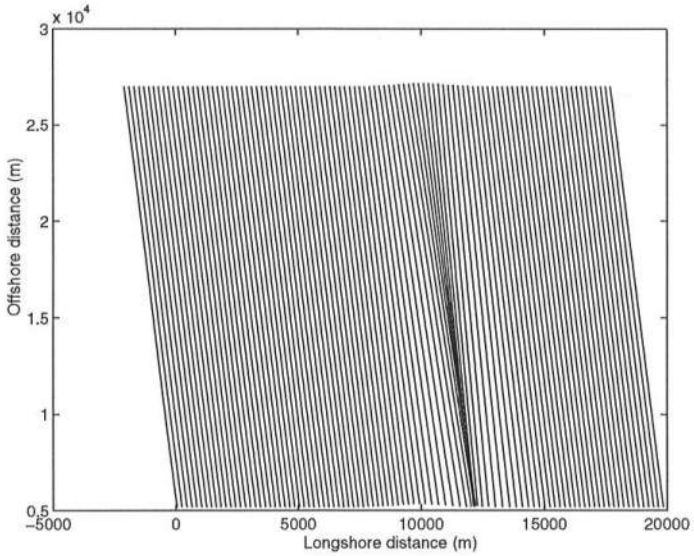

Figure 4.19: Approximated straight wave rays for incident wave angle 10^o on the mild slope ($A = 0.01$) at t=1 year. (Solitary Wave)

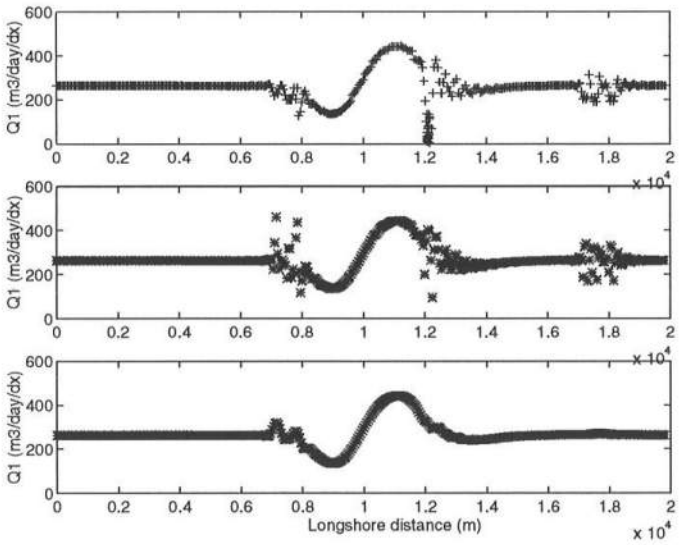

Figure 4.20: Approximation of longshore transport at y_1 contour for incident wave angle 10^o on the mild slope ($A = 0.01$) at t=1 year. Upper, raw data; middle, after bin method; lower, final result after filtering. (Solitary Wave)

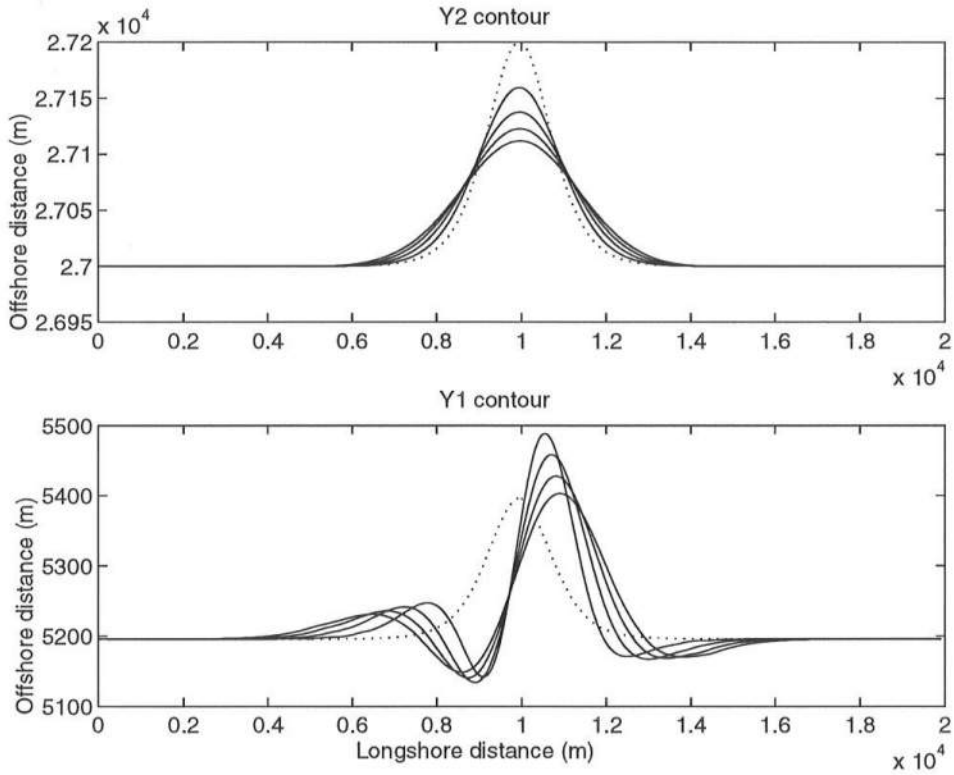

Figure 4.21: Evolution of y_1 and y_2 contours for incident wave angle 30^o on the mild slope ($A = 0.01$) at t=1, 2, 3, and 4 years. Solid line, linear model; dotted line, initial contour. (Solitary Wave).

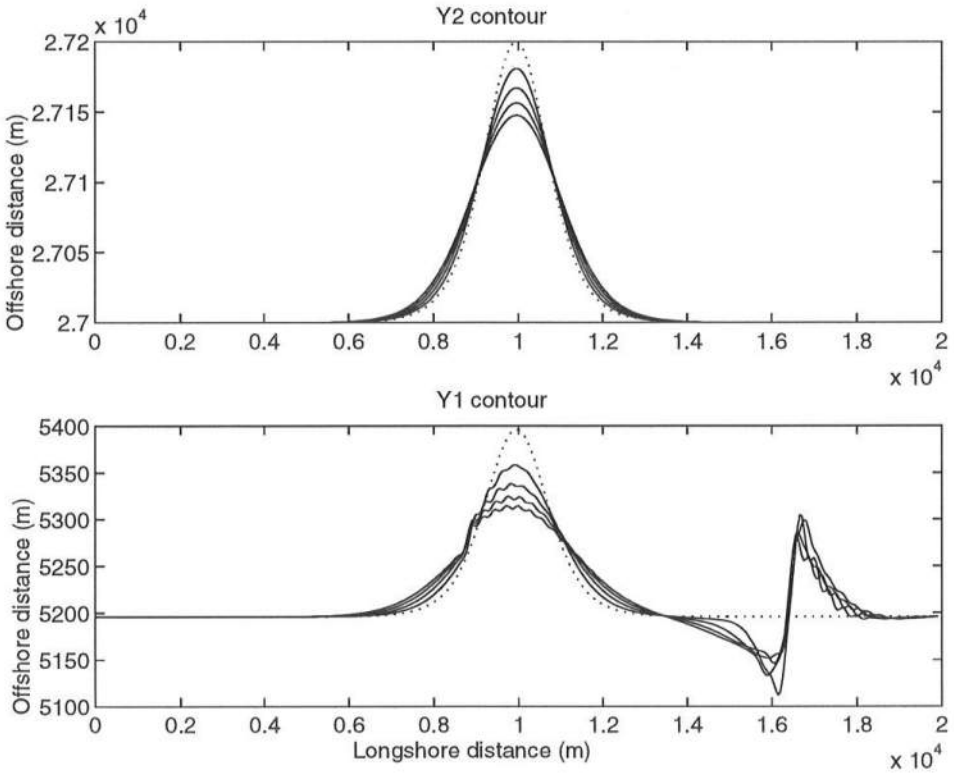

Figure 4.22: Evolution of y_1 and y_2 contours for incident wave angle 30^o on the mild slope ($A = 0.01$) at t=1, 2, 3, and 4 years. Solid line, nonlinear model; dotted line, initial contour. (Solitary Wave).

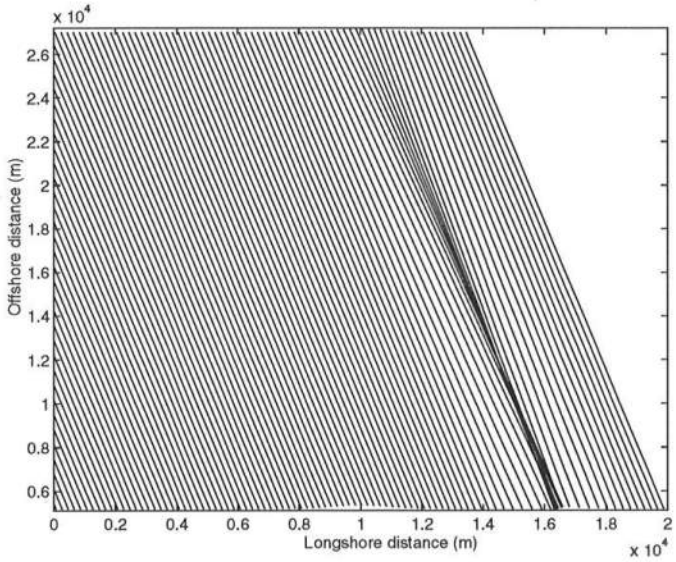

Figure 4.23: Approximated straight wave rays for incident wave angle 30^o on the mild slope ($A = 0.01$) at t=1 year. (Solitary Wave)

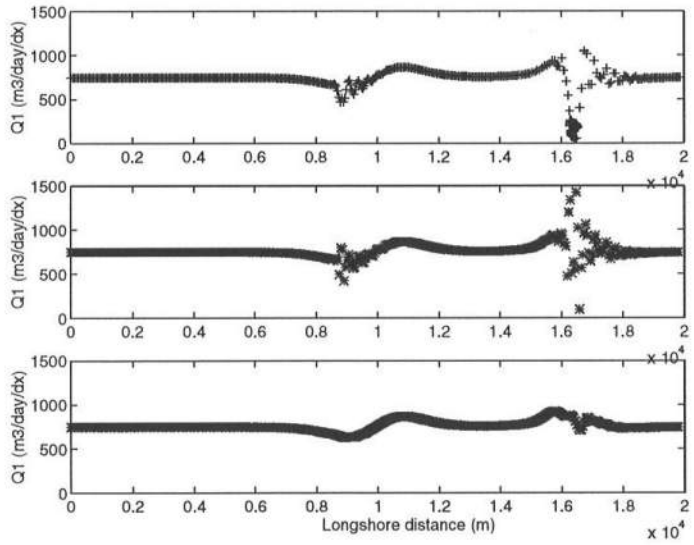

Figure 4.24: Approximation of longshore transport at y_1 contour for incident wave angle 30^o on the mild slope ($A = 0.01$) at t=1 year. Upper, raw data; middle, after bin method; lower, final result after filtering. (Solitary Wave)

Figure 4.25 and Figure 4.26 show evolutions of the y_1 and y_2 contours at t=1, 2, 3, and 4 years. Both models did not show any migration on the profile with $A = 0.1$ even for the large incident wave angle. For the incident angle 0^o, both models give almost same results. For 30^o, the linear model decay faster than the nonlinear, and the nonlinear model shows a small focusing effect on the crest of the solitary wave.

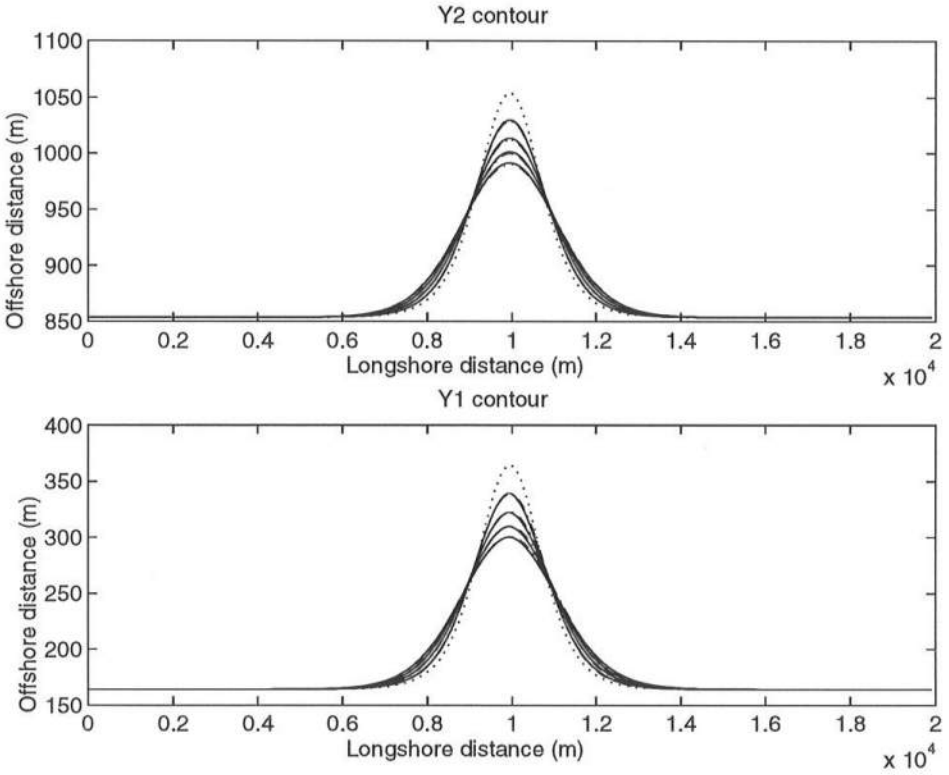

Figure 4.25: Evolution of y_1 and y_2 contours for incident wave angle 0^o on the regular slope ($A = 0.1$) at t=1, 2, 3, and 4 years. Solid line, nonlinear model; dash-dotted line, linear model; dotted line, initial contour (Solitary Wave).

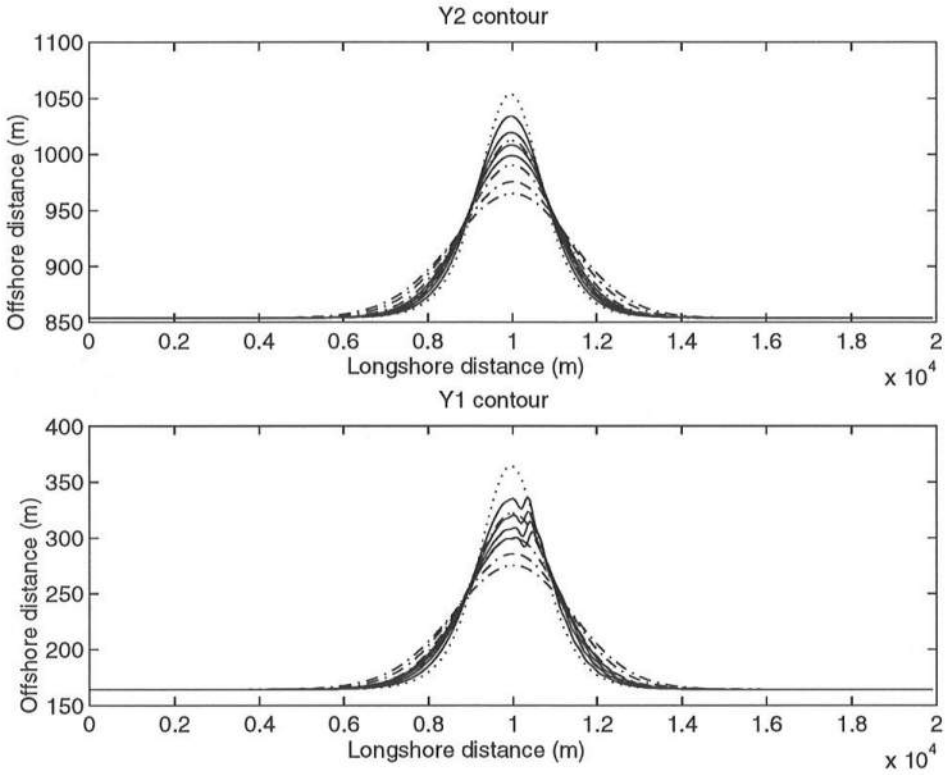

Figure 4.26: Evolution of y_1 and y_2 contours for incident wave angle 30^o on the regular slope ($A = 0.1$) at t=1, 2, 3, and 4 years. Solid line, nonlinear model; dash-dotted line, linear model; dotted line, initial contour (Solitary Wave).

4.2.3 Beach Fill

The model was next examined by using the beach fill shaped contours which are not as smooth as the solitary wave contour. The initial shape of the y_1 contour was a trapezoidal, approximately 5000 m long and 200 m wide. Both ends of the fill are tapered with a slope, 1 : 2. The y_2 contour has basically the same shape as the y_1 contour; however, the spacing between the y_1 and the y_2 contour is reduced by 100 m. As shown in Table 4.3, the results were compared in four cases in which sediment scale parameter, $A = 0.1, 0.01$ and the offshore depth $D_2 = 3\,m, 6\,m$. Each case has two kinds of incident wave angle, 0^o and 30^o.

Table 4.3: Input conditions for beach fill cases

Conditions	unit	Case 1	Case 2	Case3	Case 4
D_1	m	3.0	3.0	3.0	3.0
D_2	m	6.0	6.0	3.0	3.0
A	$m^{\frac{1}{3}}$	0.1	0.01	0.1	0.01
H_b	m	0.5	0.5	0.5	0.5
δ_o	$degree$	0, 30	0, 30	0, 30	0, 30
T	sec	10	10	10	10
$\mathcal{K}$	--	0.77	0.77	0.77	0.77
C_y	m/day	0.60	5.12×10^{-5}	0.27	1.8×10^{-4}
k_y	m^4/N	2.2×10^{-6}	2.2×10^{-6}	2.2×10^{-6}	2.2×10^{-6}
dx	m	50	50	50	50
dt	day	2	2	2	2

Figures 4.27 to 4.32 show the results from case 1. Since the linear and the nonlinear models use different cross-shore transport model, C_y values were estimated such that both models would give the same cross-shore transport at the beginning of the computation. Specifically, both formulas were equated then solved for C_y using the spacing between the two contours at the center of the fill as $(y_2 - y_1)$.

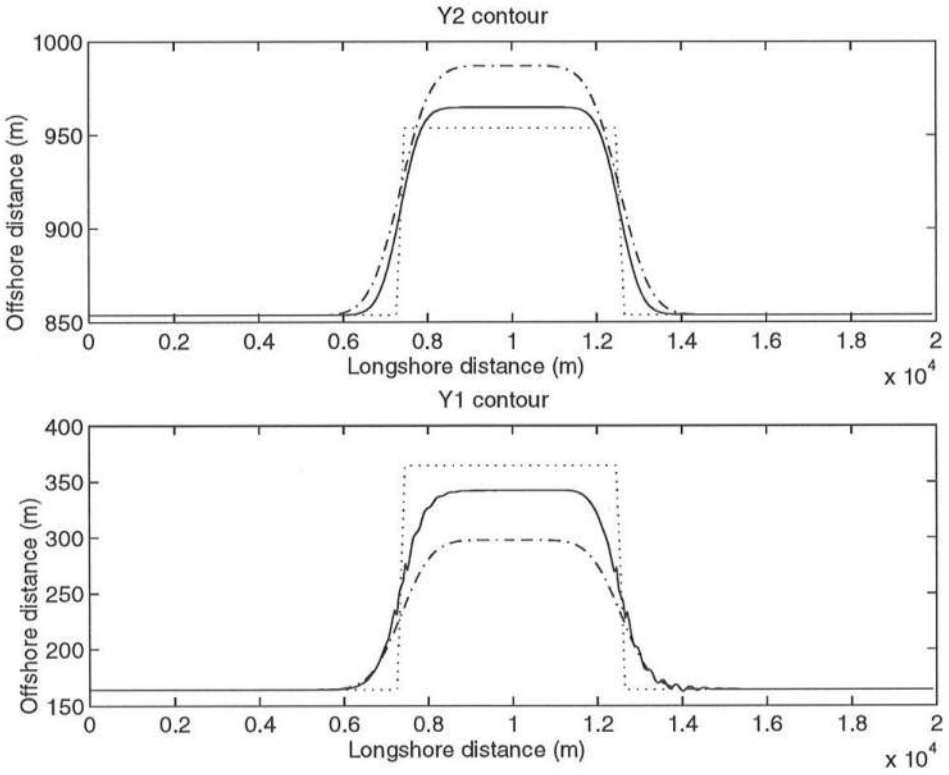

Figure 4.27: The position of y_1 and y_2 contours for incident wave angle 0^o on the regular slope ($A = 0.1$) at t=1 year. Solid line, nonlinear model; dash-dotted line, linear model; dotted line, initial contour (Beach Fill ; Case 1).

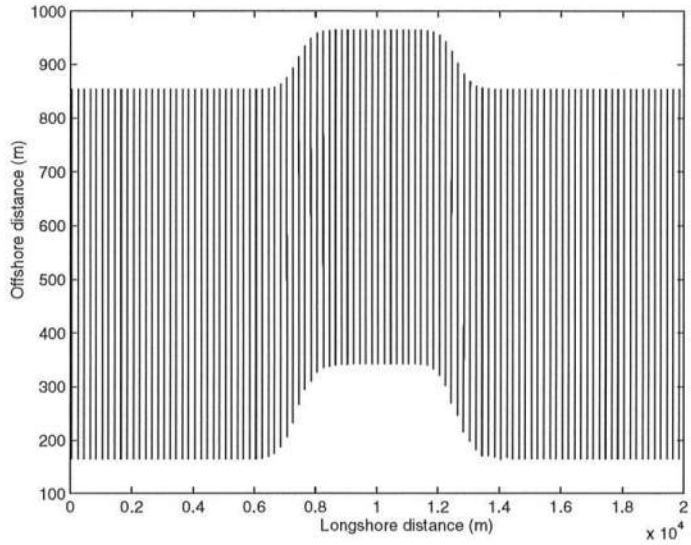

Figure 4.28: Approximated straight wave rays for incident wave angle 0^o on the mild slope ($A = 0.1$) at t=1 year (Beach Fill ; Case 1).

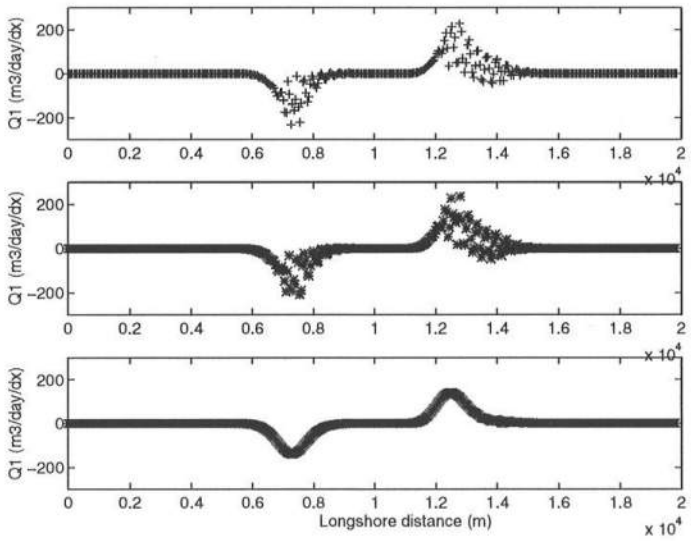

Figure 4.29: Approximation of longshore transport at y_1 contour for incident wave angle 0^o on the regular slope ($A = 0.1$) at t=1 year. Upper, raw data; middle, after bin method; lower, final result after filtering (Beach Fill ; Case 1)

For the incident wave angle 30^o, the result from the nonlinear model shows an antisymmetric shape. This might be caused by a wave refraction effect. Both cases show that the nonlinear model tends to keep the initial shape more than the linear model; in other words, the nonlinear model tends to decay more slowly. In this case, the incident wave angle did not affect the results so much.

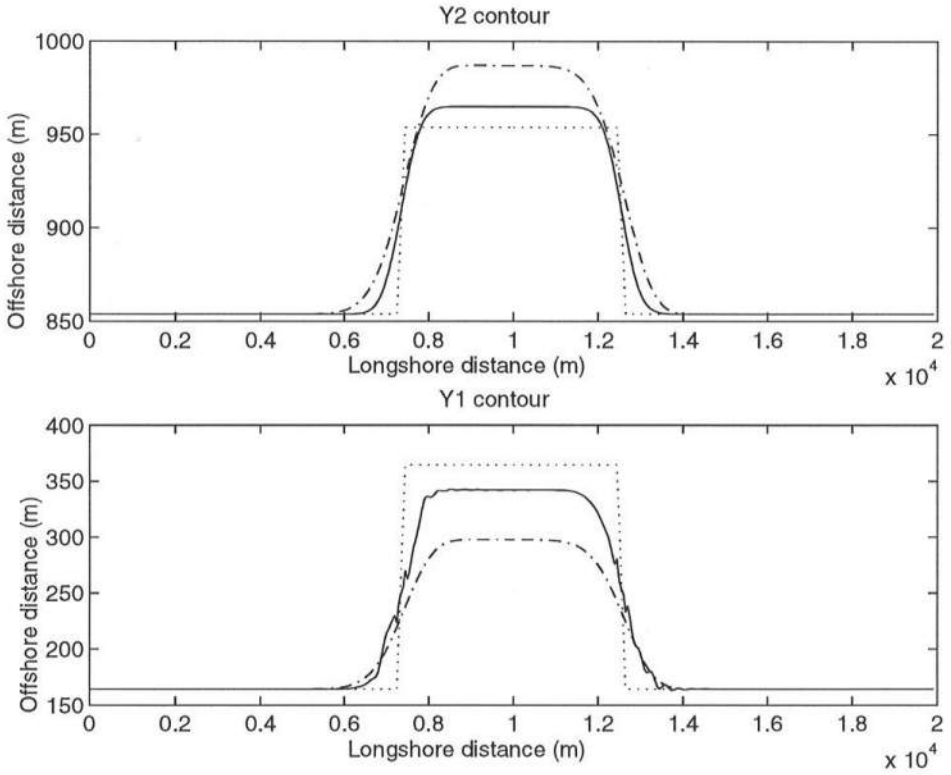

Figure 4.30: The position of y_1 and y_2 contours for incident wave angle 30^o on the regular slope ($A = 0.1$) at t=1 year. Solid line, nonlinear model; dash-dotted line, linear model; dotted line, initial contour (Beach Fill ; Case 1).

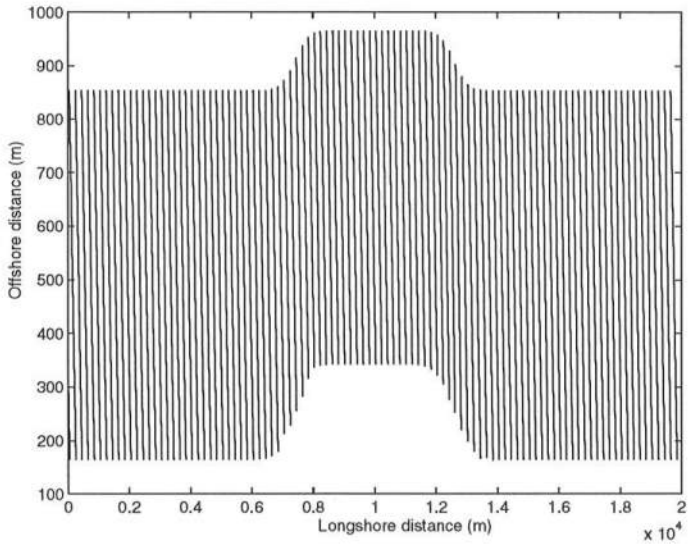

Figure 4.31: Approximated straight wave rays for incident wave angle 30^o on the regular slope ($A = 0.1$) at t=1 year (Beach Fill ; Case 1).

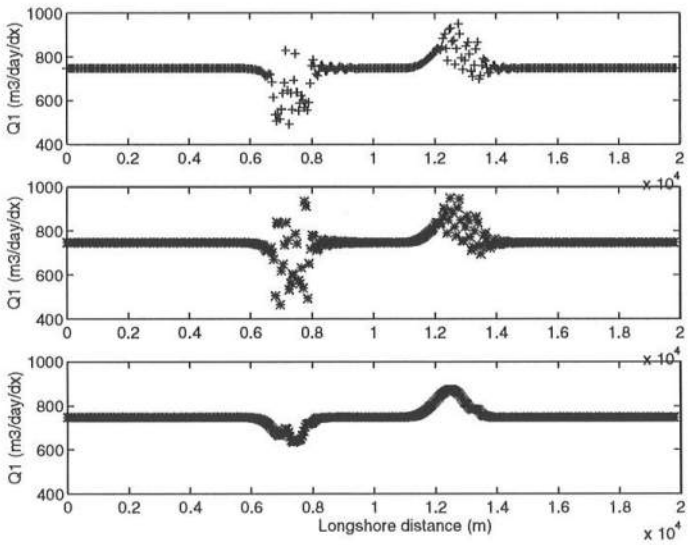

Figure 4.32: Approximation of longshore transport at the y_1 contour for incident wave angle 30^o on the regular slope ($A = 0.1$) at t=1 year. Upper, raw data; middle, after bin method; lower, final result after filtering (Beach Fill ; Case 1)

Figures 4.33 to 4.38 show the results from case 2. For the incident wave angle 0^o, the lifetime of the beach fill was much longer than case 1 for both the models. Surprisingly, both models give almost same results. For the nonlinear model, it is possible that longshore transport against the decay was produced by a focusing effect (see Figure 4.34). The nonlinear model showed a big focusing effect for the large incident wave angle 30^o, which clearly appeared on the downwave side of the beach fill in Figure 4.37, while the linear model showed an unusual shape that was difficult to interpret physically.

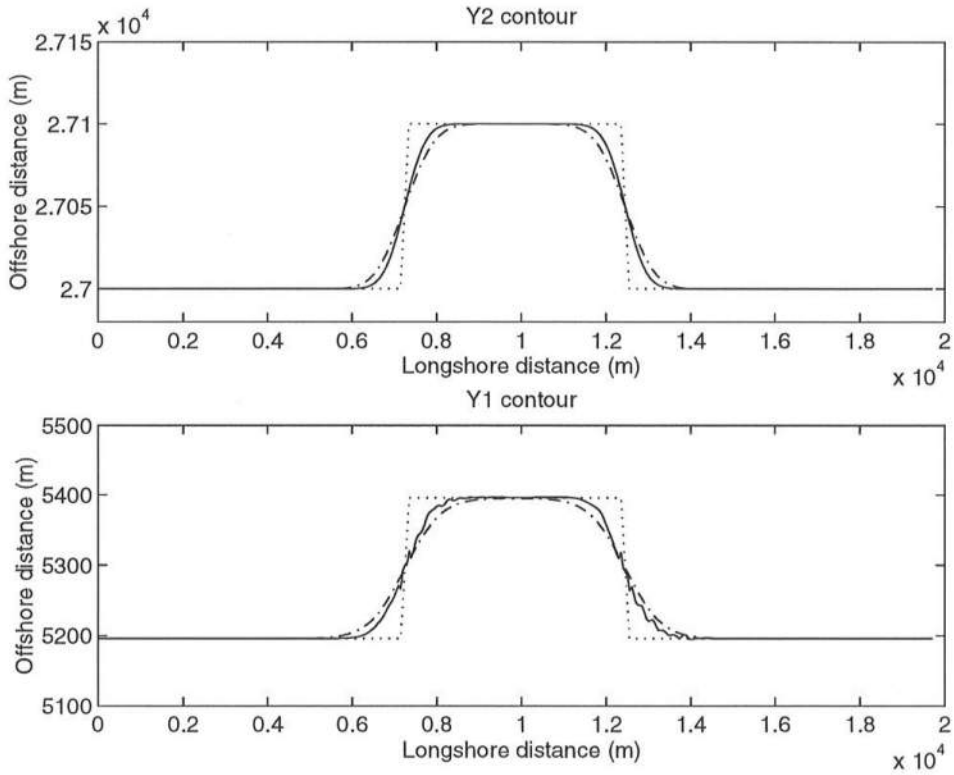

Figure 4.33: The position of y_1 and y_2 contours for incident wave angle 0^o on the mild slope ($A = 0.01$) at t=1 year. Solid line, nonlinear model; dash-dotted line, linear model; dotted line, initial contour (Beach Fill ; Case 2).

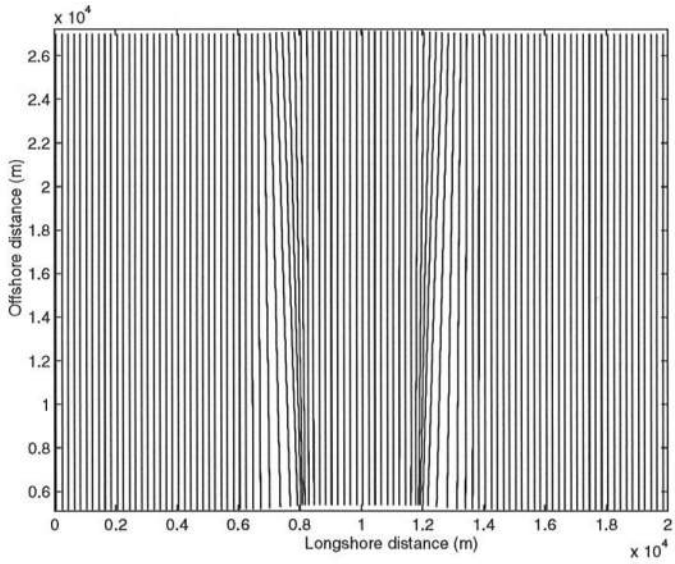

Figure 4.34: Approximated straight wave rays for incident wave angle 0^o on the mild slope ($A = 0.01$) at t=1 year (Beach Fill ; Case 2).

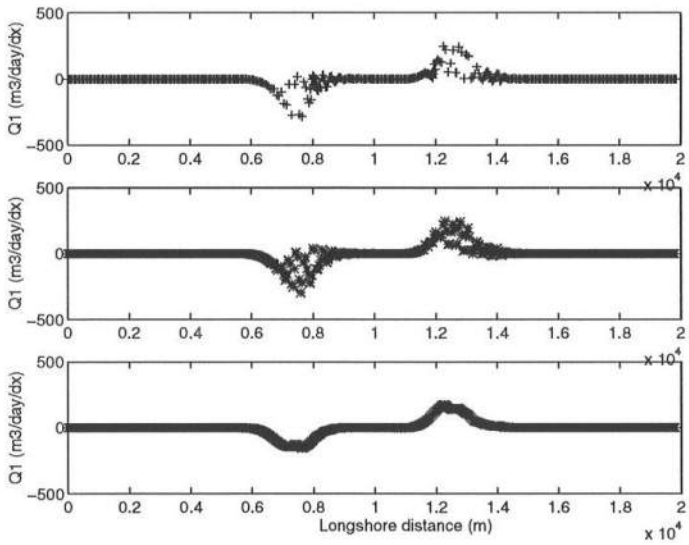

Figure 4.35: Approximation of longshore transport at y_1 contour for incident wave angle 0^o on the mild slope ($A = 0.01$) at t=1 year. Upper, raw data; middle, after bin method; lower, final result after filtering (Beach Fill ; Case 2)

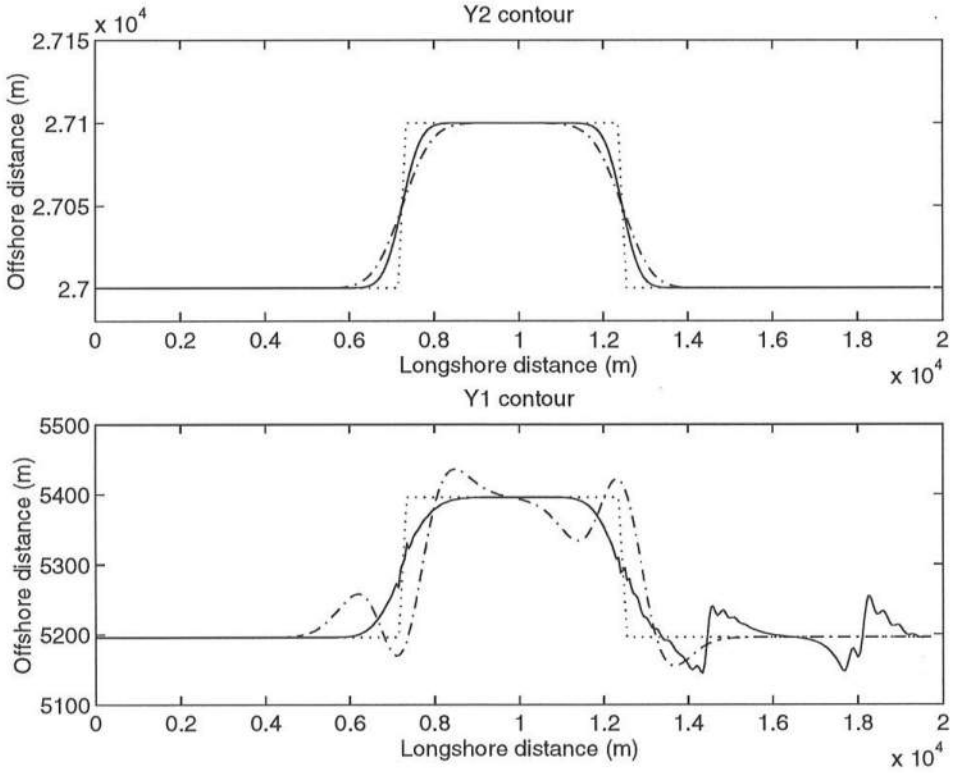

Figure 4.36: The position of y_1 and y_2 contours for incident wave angle 30^o on the mild slope ($A = 0.01$) at t=1 year. Solid line, nonlinear model; dash-dotted line, linear model; dotted line, initial contour (Beach Fill ; Case 2).

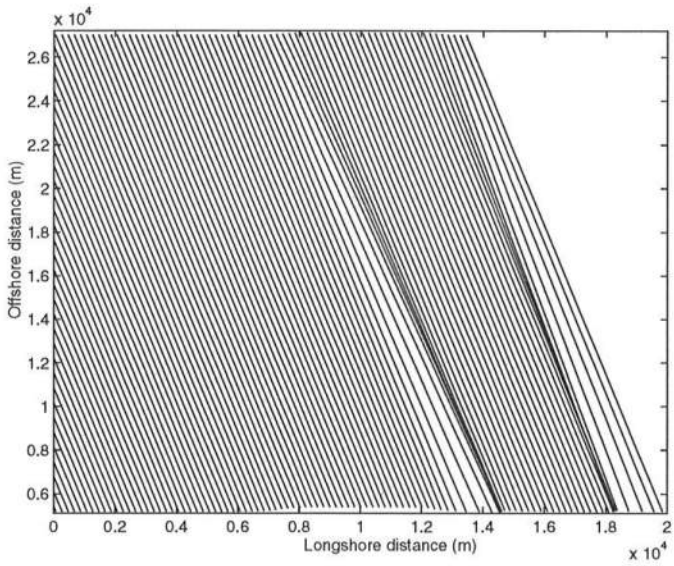

Figure 4.37: Approximated straight wave rays for incident wave angle 30^o on the mild slope ($A = 0.01$) at t=1 year (Beach Fill ; Case 2).

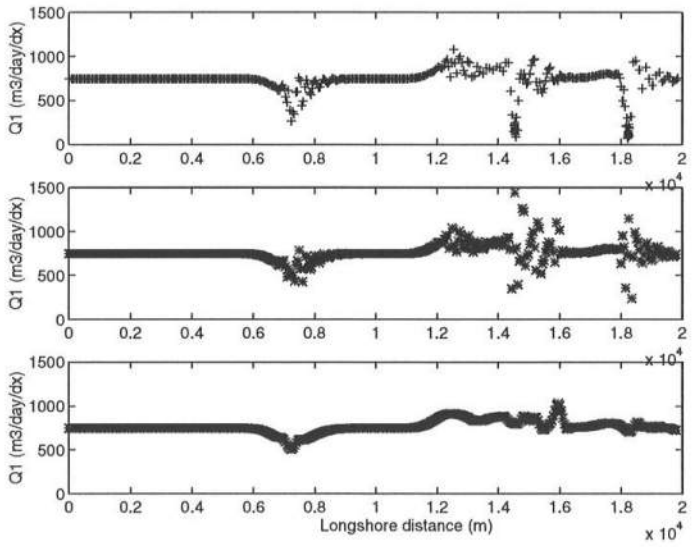

Figure 4.38: Approximation of longshore transport at y_1 contour for incident wave angle 30^o on the mild slope ($A = 0.01$) at t=1 year. Upper, raw data; middle, after bin method; lower, final result after filtering (Beach Fill ; Case 2)

Figures 4.39 to 4.44 show the results from case 3. In case 3, the shallower offshore depth $D_2 = 3\,m$ was used. Basically, this case showed same trends as case 1, although the difference between both results was smaller than that in case 1. The difference between results from the two incident wave angles was very small as in case 1.

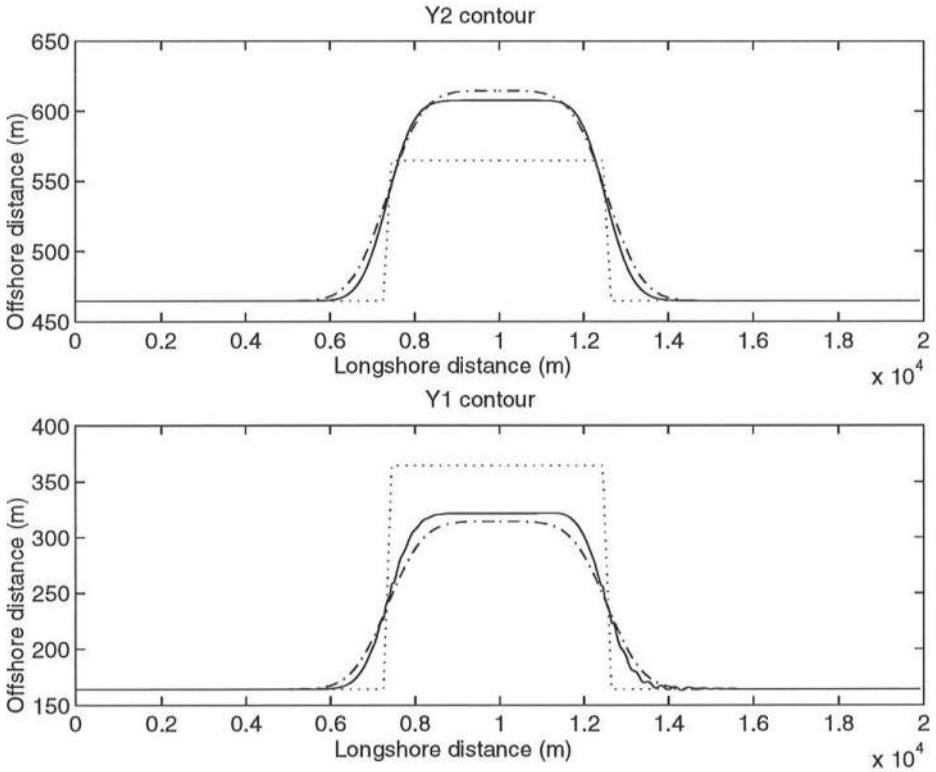

Figure 4.39: The position of y_1 and y_2 contours for incident wave angle 0^o on the regular slope ($A = 0.1$) at t=1 year. Solid line, nonlinear model; dash-dotted line, linear model; dotted line, initial contour (Beach Fill ; Case 3).

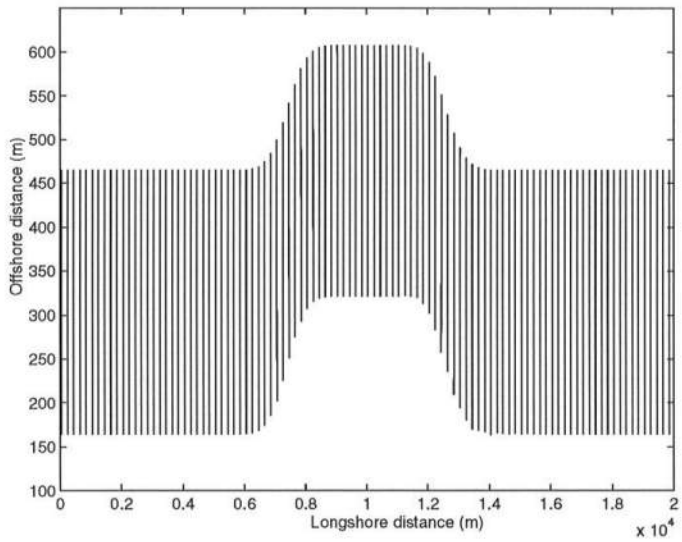

Figure 4.40: Approximated straight wave rays for incident wave angle 0^o on the regular slope ($A = 0.1$) at t=1 year (Beach Fill ; Case 3).

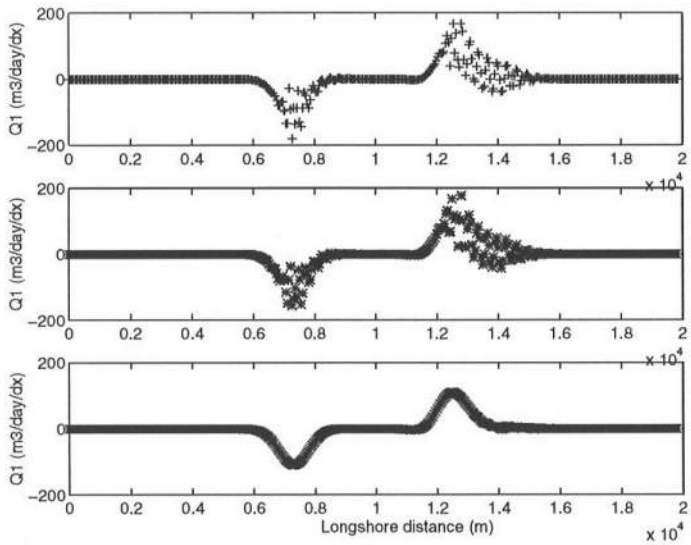

Figure 4.41: Approximation of longshore transport at y_1 contour for incident wave angle 0^o on the regular slope ($A = 0.1$) t=1 year. Upper, raw data; middle, after bin method; lower, final result after filtering (Beach Fill ; Case 3)

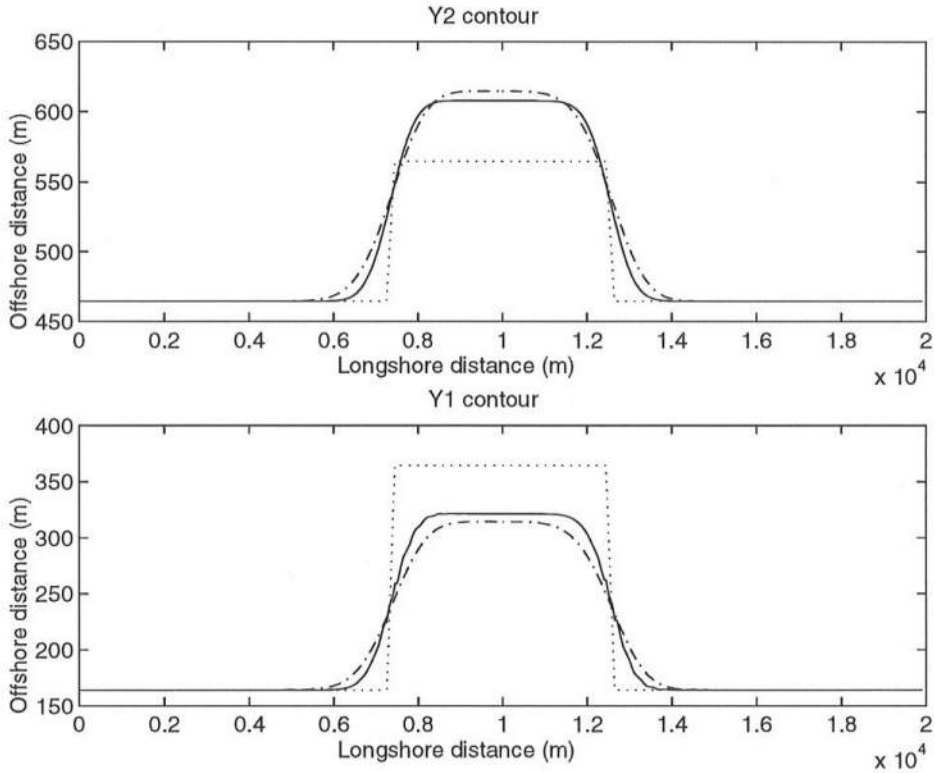

Figure 4.42: The position of y_1 and y_2 contours for incident wave angle 30^o on the regular slope ($A = 0.1$) at t=1 year. Solid line, nonlinear model; dash-dotted line, linear model; dotted line, initial contour (Beach Fill ; Case 3).

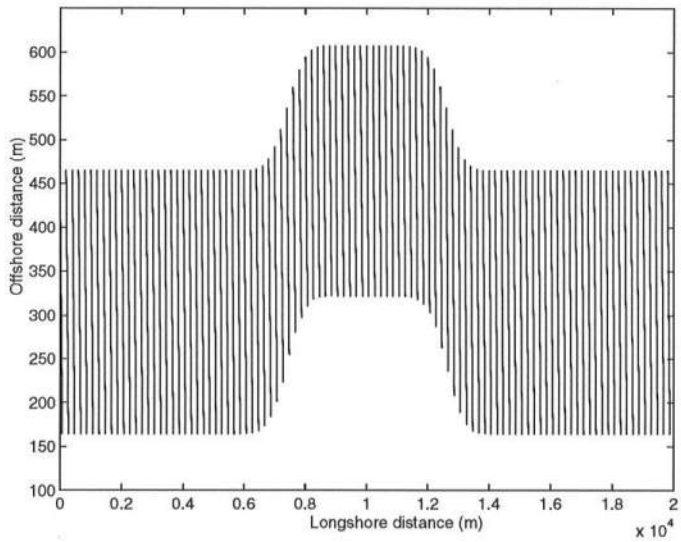

Figure 4.43: Approximated straight wave rays for incident wave angle 30^o on the regular slope ($A = 0.1$) at t=1 year (Beach Fill ; Case 3).

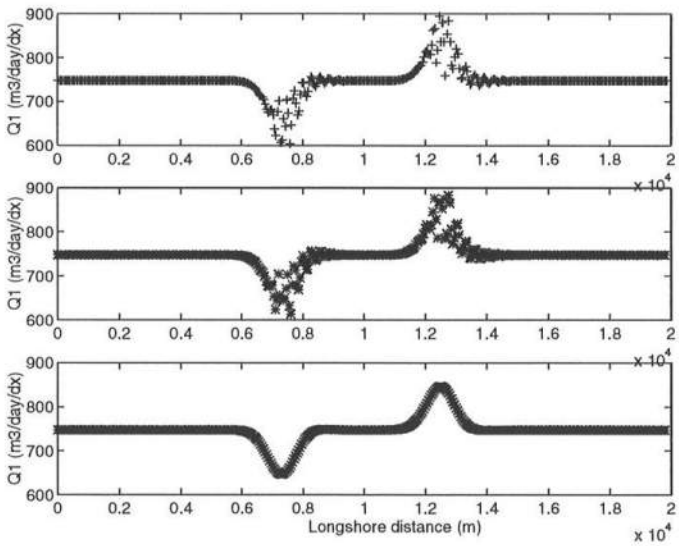

Figure 4.44: Approximation of longshore transport at y_1 contour for incident wave angle 30^o on the regular slope ($A = 0.1$) at t=1 year. Upper, raw data; middle, after bin method; lower, final result after filtering (Beach Fill ; Case 3)

Figures 4.45 to 4.50 show the results from case 4. In this case, since the spacing between two contours is smaller than case 2, the location of the focusing effect has been moved to the left. As in case 3, results in this case have similar trends as case 2, although the linear model did not show the unusual shape that was seen in case 2.

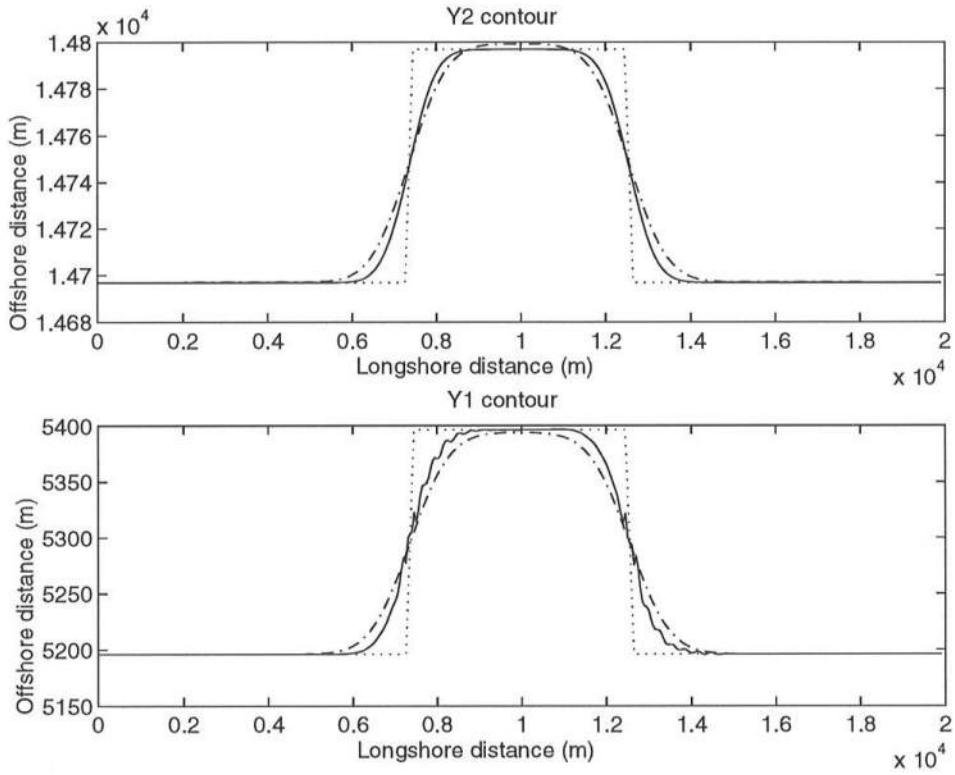

Figure 4.45: The position of y_1 and y_2 contours for incident wave angle 0^o on the mild slope ($A = 0.01$) at t=1 year. Solid line, nonlinear model; dash-dotted line, linear model; dotted line, initial contour (Beach Fill ; Case 4).

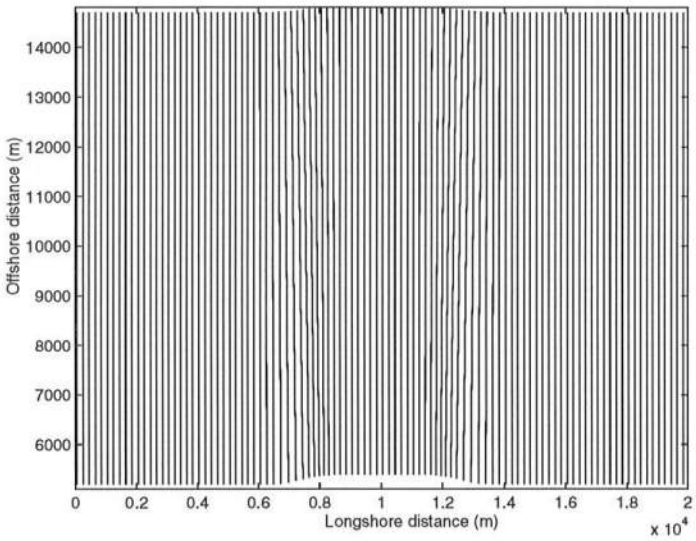

Figure 4.46: Approximated straight wave rays for incident wave angle 0^o on the mild slope ($A = 0.01$) at t=1 year (Beach Fill ; Case 4).

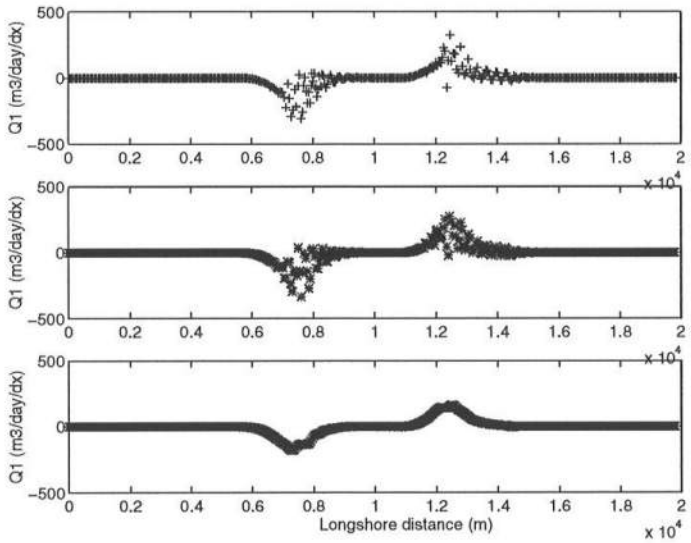

Figure 4.47: Approximation of longshore transport at y_1 contour for incident wave angle 0^o on the mild slope ($A = 0.01$) at t=1 year. Upper, raw data; middle, after bin method; lower, final result after filtering (Beach Fill ; Case 4)

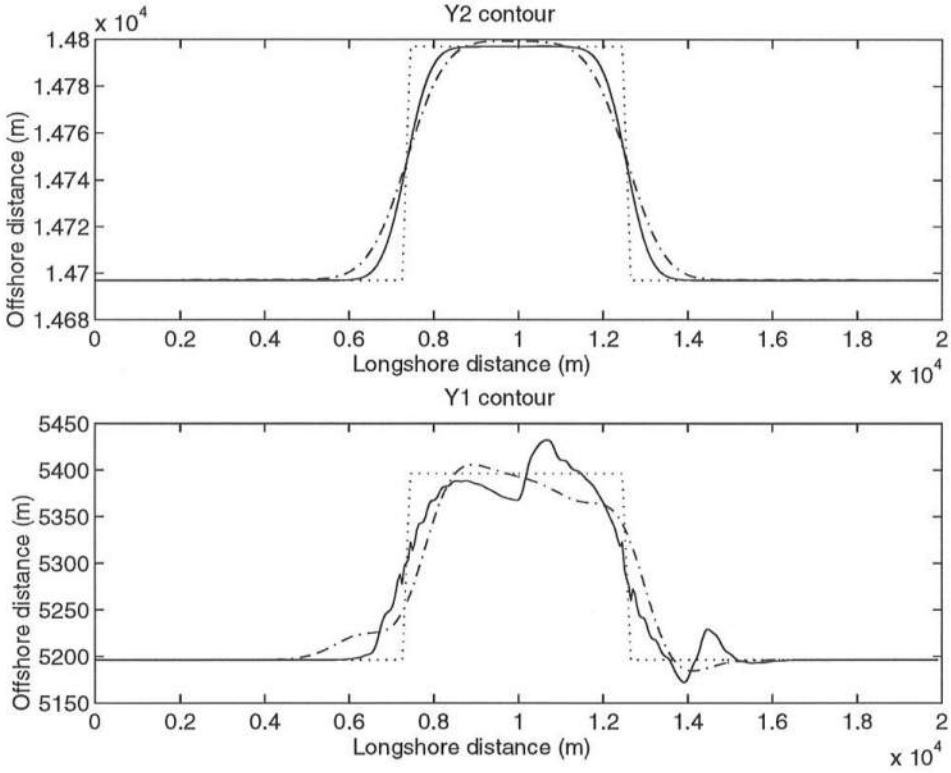

Figure 4.48: The position of y_1 and y_2 contours for incident wave angle 30^o on the mild slope ($A = 0.01$) at t=1 year. Solid line, nonlinear model; dash-dotted line, linear model; dotted line, initial contour (Beach Fill ; Case 4).

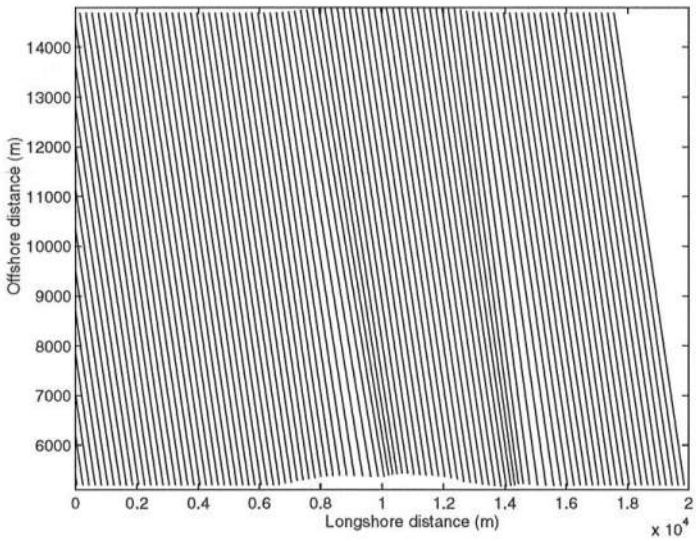

Figure 4.49: Approximated straight wave rays for incident wave angle 30^o on the mild slope ($A = 0.01$) at t=1 year (Beach Fill ; Case 4).

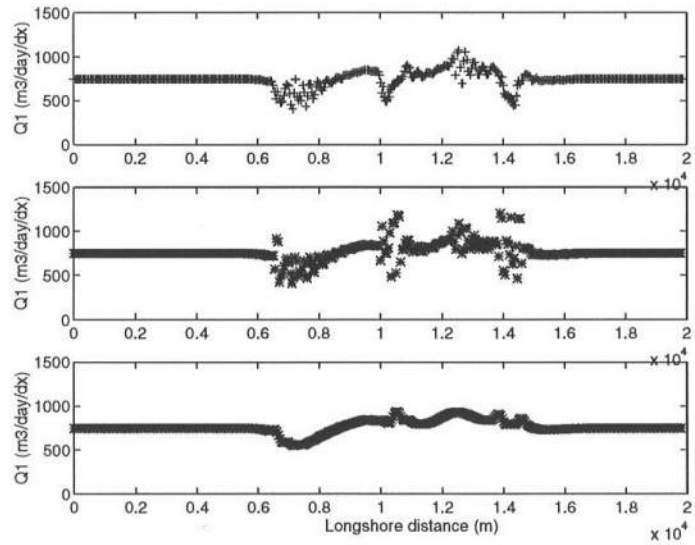

Figure 4.50: Approximation of longshore transport at y_1 contour for incident wave angle 30^o on the mild slope ($A = 0.01$) at t=1 year. Upper, raw data; middle, after bin method; lower, final result after filtering (Beach Fill ; Case 4)

4.2.4 Periodic Beach

Periodic beaches, which have sinosoidal wave shaped contours, were used for the following five cases. The amplitudes of periodic waves which describe the y_1 and y_2 contours were 200 m and 100 m, respectively, and their phase shift, $\Delta\phi$, was 0^o in case 1 to 4, varied from 0^o to 180^o every 90^o in case 5. There were five waves in the computational domain. As shown in Table 4.4, the results were compared in four cases, case 1 to case 4, depending on the sediment scale parameter, $A = 0.1,\ 0.01$ and the offshore depth $D_2 = 3\,m,\ 6\,m$. In case 5, the phase shift, $\Delta\phi$, was varied. The incident wave angle for these cases was 30^o for all cases.

Table 4.4: Input conditions for periodic beach cases

Conditions	unit	Case 1	Case 2	Case3	Case 4	case 5
D_1	m	3.0	3.0	3.0	3.0	3.0
D_2	m	6.0	6.0	3.0	3.0	3.0
A	$m^{\frac{1}{3}}$	0.1	0.01	0.1	0.01	0.01
H_b	m	0.3	0.3	0.3	0.3	0.3
δ_o	$degree$	30	30	30	30	30
T	sec	10	10	10	10	10
K	--	0.77	0.77	0.77	0.77	0.77
C_y	m/day	0.06	5.12×10^{-5}	0.27	1.8×10^{-4}	0.0001
k_y	m^4/N	2.2×10^{-6}	2.2×10^{-6}	2.2×10^{-6}	2.2×10^{-6}	2.2×10^{-6}
$\Delta\phi$	$degree$	0	0	0	0	180@90
dx	m	50	50	50	50	50
dt	day	10	10	8	8	8

Figure 4.51 to Figure 4.54 show the results from case 1. In this case, one can see relatively small focusing effect at the crest of each wave in the nonlinear model. Otherwise, the linear model decayed a little faster than the nonlinear model.

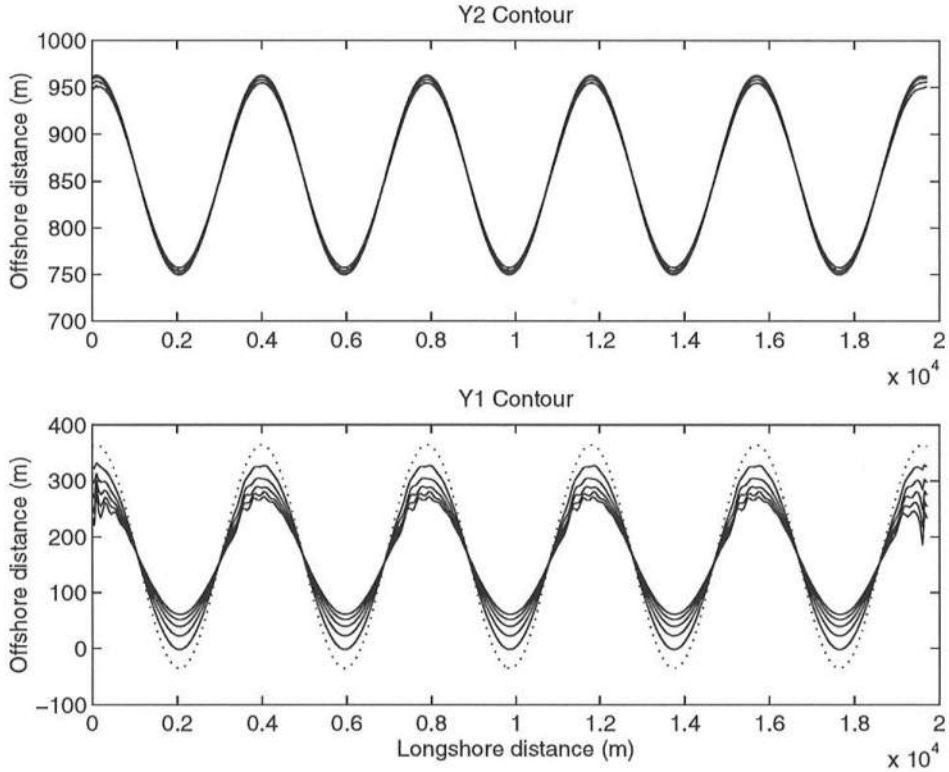

Figure 4.51: Evolution of y_1 and y_2 contours for incident wave angle 30^o on the regular slope ($A = 0.1$) at t=400, 800, 1200, 1600 and 2000 days. Solid line, nonlinear model; dotted line, initial contour (Periodic Beach ; Case 1).

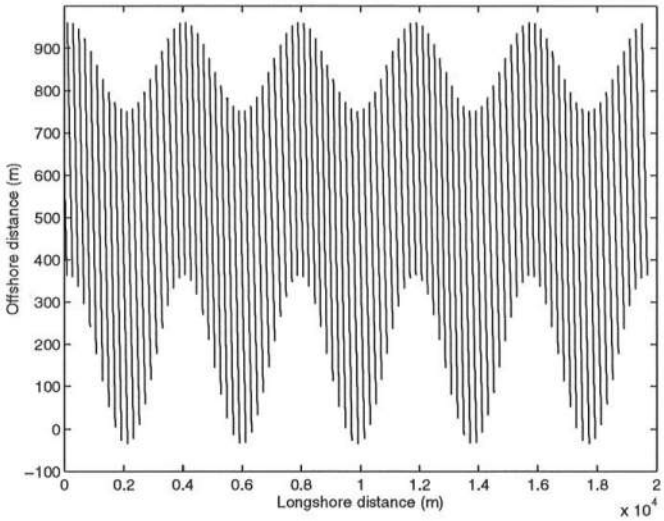

Figure 4.52: Approximated straight wave rays for incident wave angle 30^o on the regular slope ($A = 0.1$) at t=400 days (Periodic Beach ; Case 1).

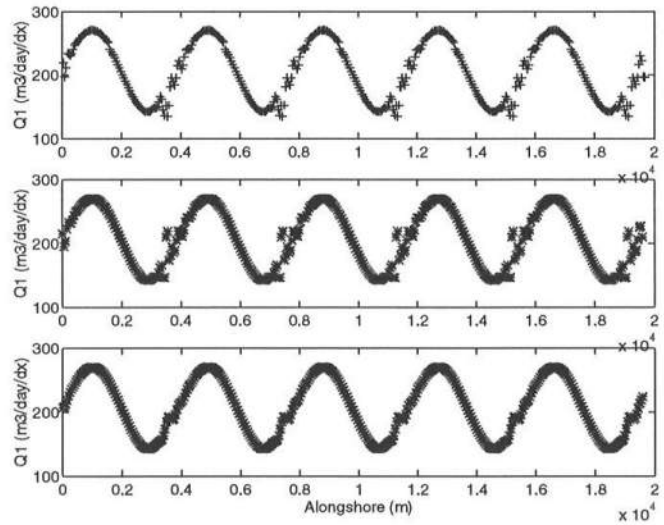

Figure 4.53: Approximation of longshore transport at y_1 contour for incident wave angle 30^o on the regular slope ($A = 0.1$) at t=400 days. Upper, raw data; middle, after bin method; lower, final result after filtering (Periodic Beach ; Case 1)

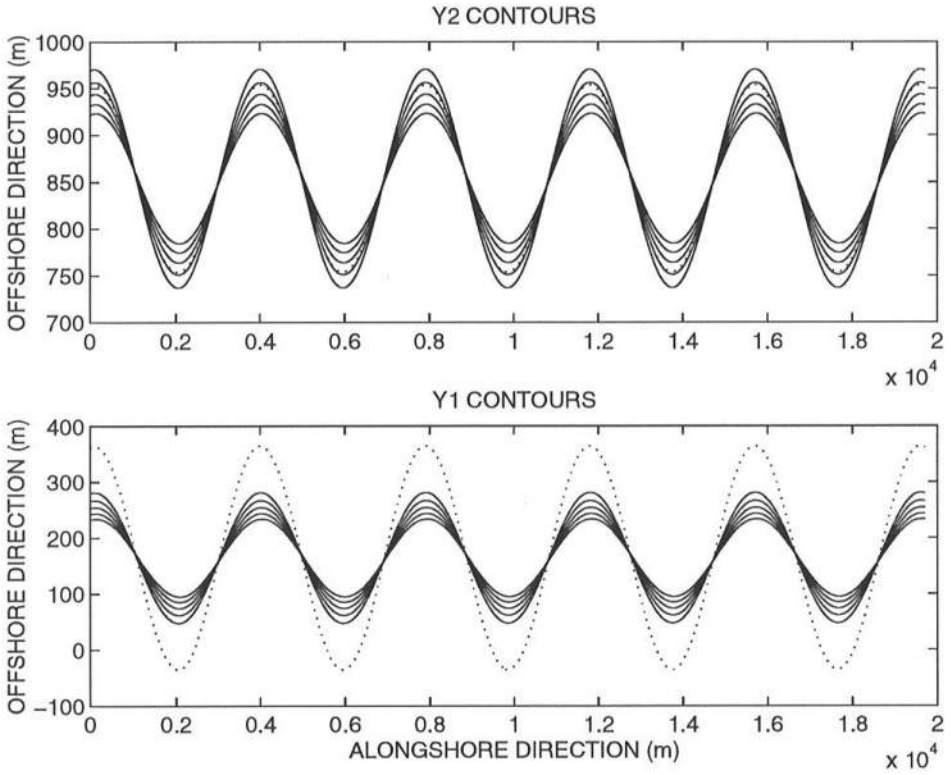

Figure 4.54: Evolution of y_1 and y_2 contours for incident wave angle 30^o on the regular slope ($A = 0.1$) at t=400, 800, 1200, 1600 and 2000 days. Solid line, linear model; dotted line, initial contour (Periodic Beach ; Case 1).

Figure 4.55 to Figure 4.58 show the results from case 2. In this case, there were strong focusing effect at the trough of waves in the nonlinear model. As shown in Figure 4.56, one can notice the very high density of the rays with strong focussing at those region. In fact, the result from the nonlinear model blowed up later. So, the contours after only 400 days are shown in Figure 4.55. On the other hand, the linear model showed some migration. The amplitude of the y_1 contours increased with the propagation.

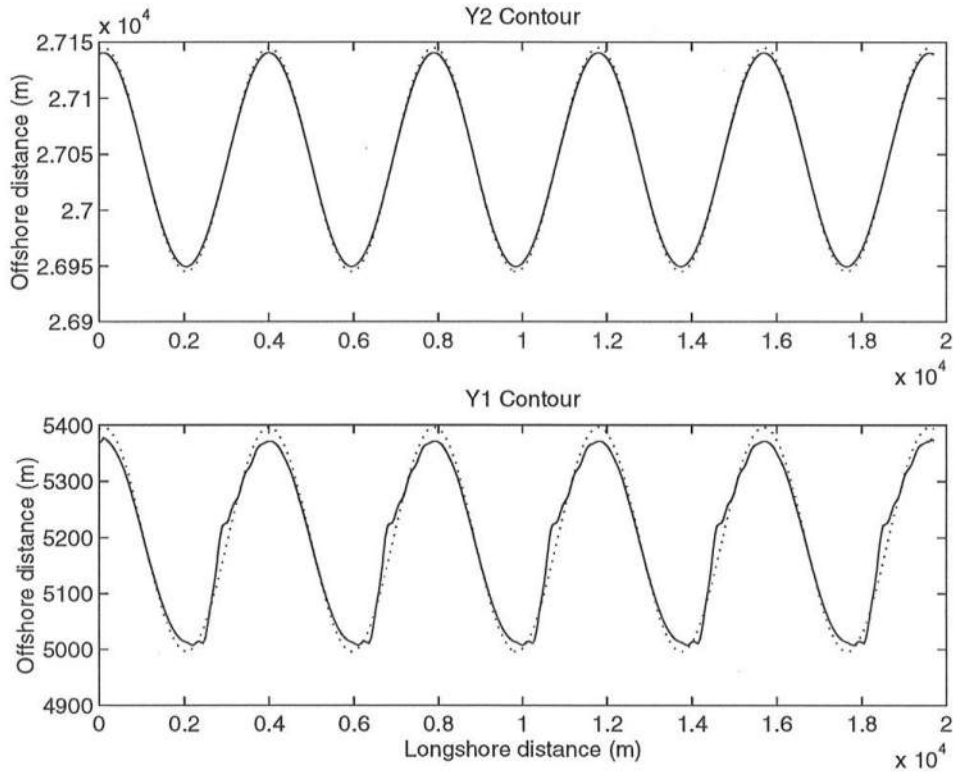

Figure 4.55: Evolution of y_1 and y_2 contours for incident wave angle 30^o on the mild slope ($A = 0.01$) at t=400 days. Solid line, nonlinear model; dotted line, initial contour (Periodic Beach ; Case 2).

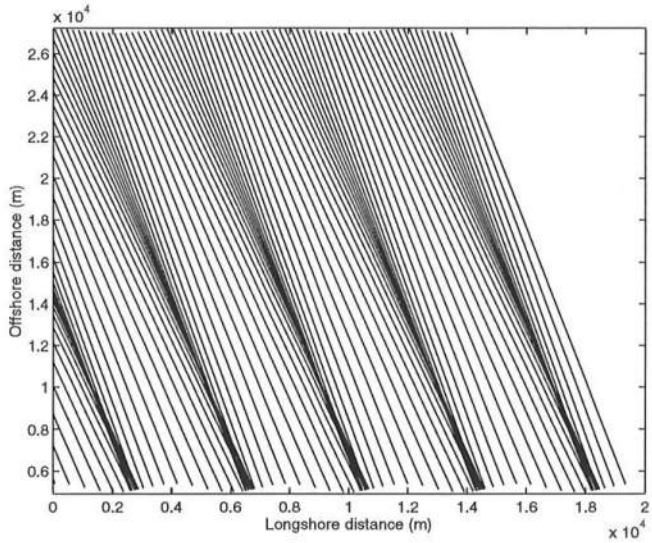

Figure 4.56: Approximated straight wave rays for incident wave angle 30^o on the mild slope ($A = 0.01$) at t=400 days (Periodic Beach ; Case 2).

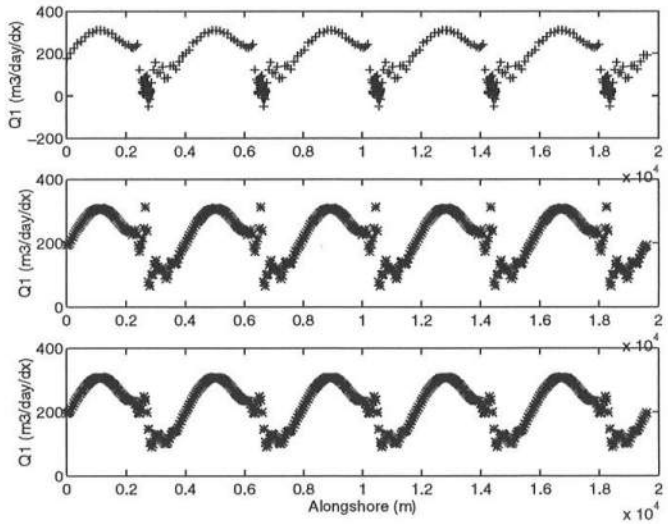

Figure 4.57: Approximation of longshore transport at y_1 contour for incident wave angle 30^o on the mild slope ($A = 0.01$) at t=400 days. Upper, raw data; middle, after bin method; lower, final result after filtering (Periodic Beach ; Case 2)

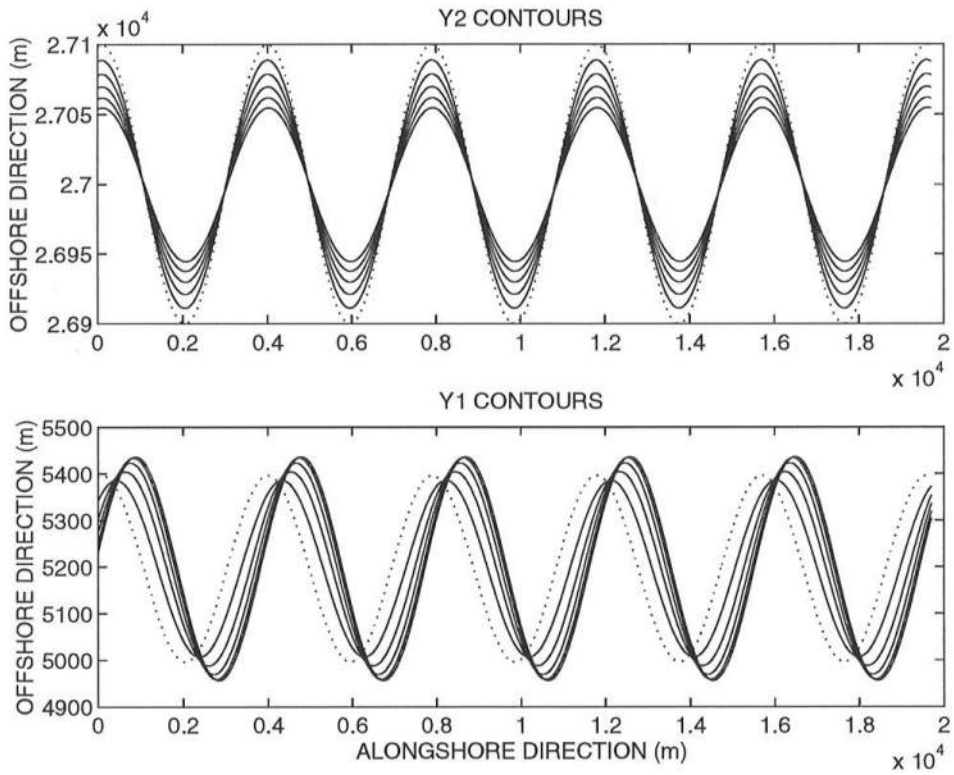

Figure 4.58: Evolution of y_1 and y_2 contours for incident wave angle 30^o on the mild slope ($A = 0.01$) at t=1, 2, 3, and 4 years. Solid line, linear model; dotted line, initial contour. (Periodic Beach ; Case 2).

Figure 4.59 to Figure 4.62 show the results from case 3. Due to the shollow offshore depth, there was not enough distance between two contours for wave rays to concentrate. As a result, the focusing effect in the nonlinear model was reduced. The linear model also gave the simply decaying result.

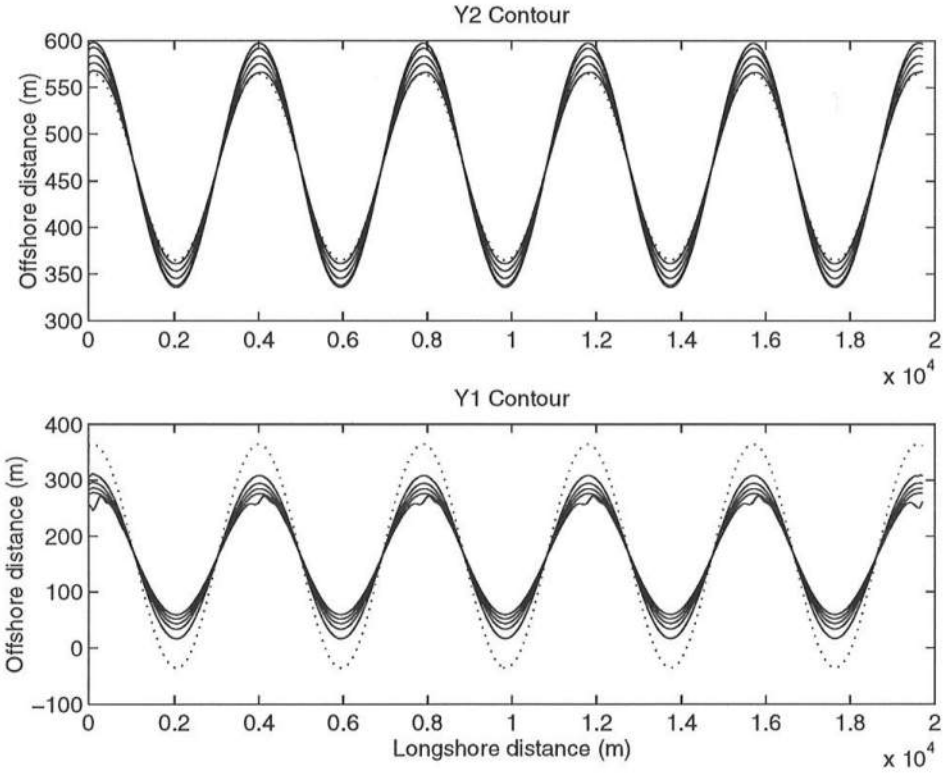

Figure 4.59: Evolution of y_1 and y_2 contours for incident wave angle 30^o on the regular slope ($A = 0.1$) at t=400, 800, 1200, 1600 and 2000 days. Solid line, nonlinear model; dotted line, initial contour (Periodic Beach ; Case 3).

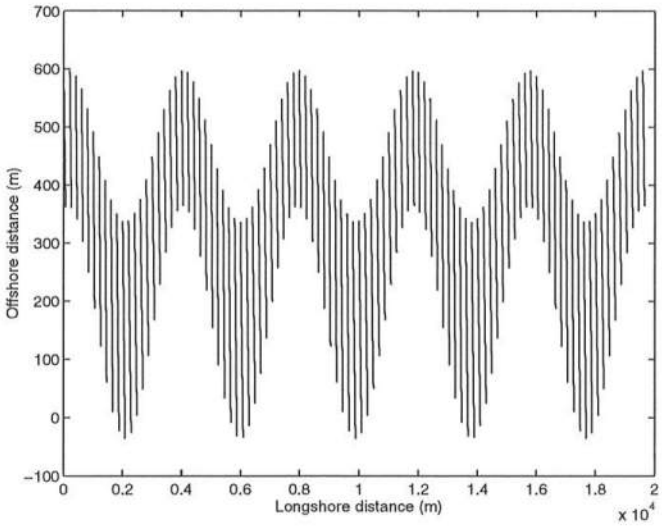

Figure 4.60: Approximated straight wave rays for incident wave angle 30^o on the regular slope ($A = 0.1$) at t=400 days (Periodic Beach ; Case 3).

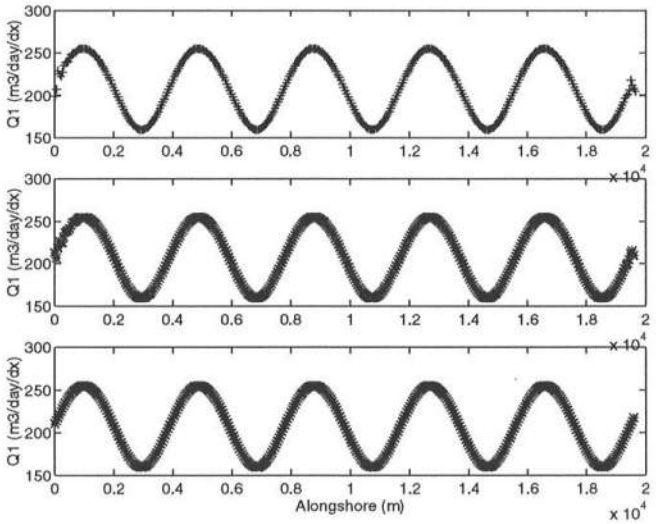

Figure 4.61: Approximation of longshore transport at y_1 contour for incident wave angle 30^o on the regular slope ($A = 0.1$) at t=400 days. Upper, raw data; middle, after bin method; lower, final result after filtering (Periodic Beach ; Case 3)

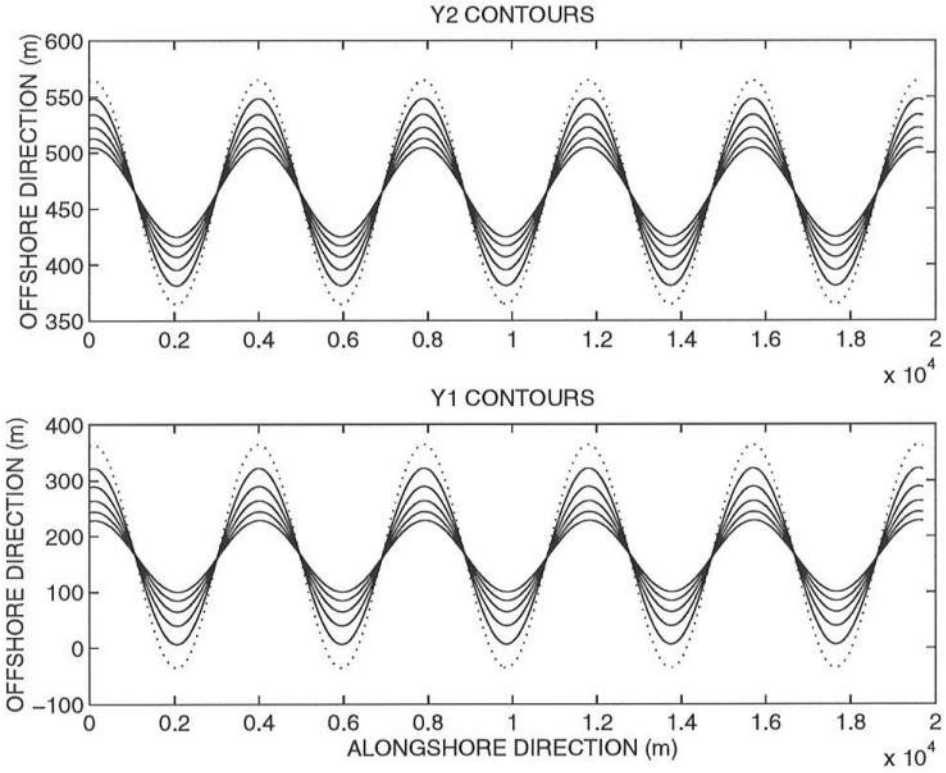

Figure 4.62: Evolution of y_1 and y_2 contours for incident wave angle 30^o on the regular slope ($A = 0.1$) at t=400, 800, 1200, 1600 and 2000 days. Solid line, linear model; dotted line, initial contour (Periodic Beach ; Case 3).

Figure 4.63 to Figure 4.66 show the results from case 4. As in case 2, the nonlinear model gave the focusing effect at the trough of waves, however, once again, the effect was reduced due to the shallow geometry. The linear model gave migration with decay of the amplitude, wihle the nonlinear model showed some movement, however, it moved upwave.

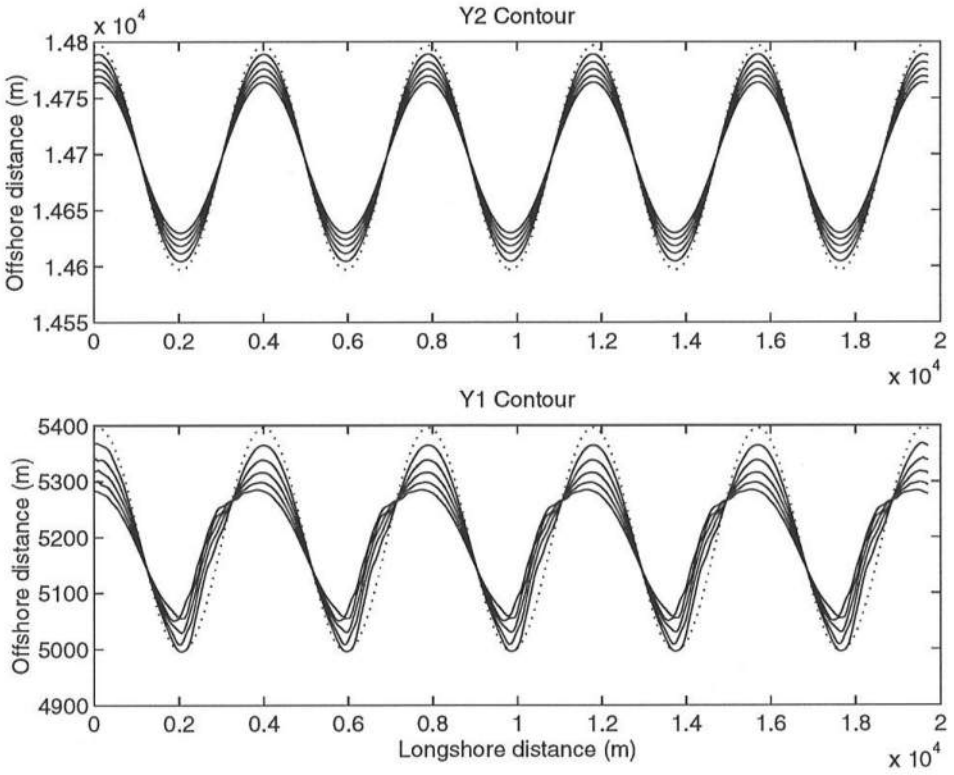

Figure 4.63: Evolution of y_1 and y_2 contours for incident wave angle 30^o on the mild slope ($A = 0.01$) at t=400, 800, 1200, 1600 and 2000 days. Solid line, nonlinear model; dotted line, initial contour (Periodic Beach ; Case 4).

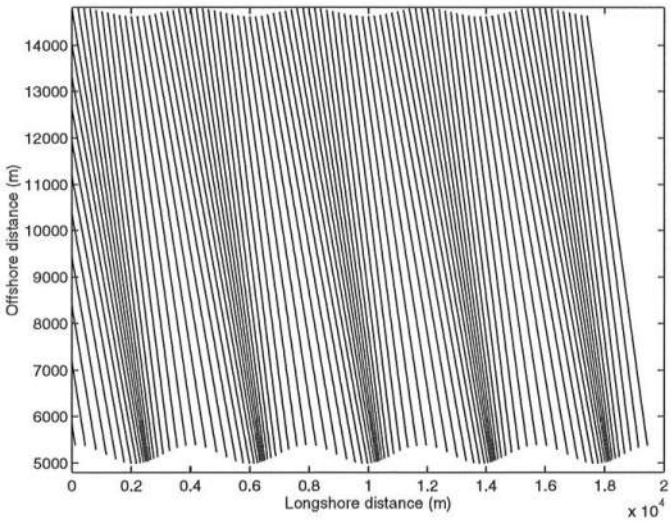

Figure 4.64: Approximated straight wave rays for incident wave angle 30^o on the mild slope ($A = 0.01$) at t=400 days (Periodic Beach ; Case 4).

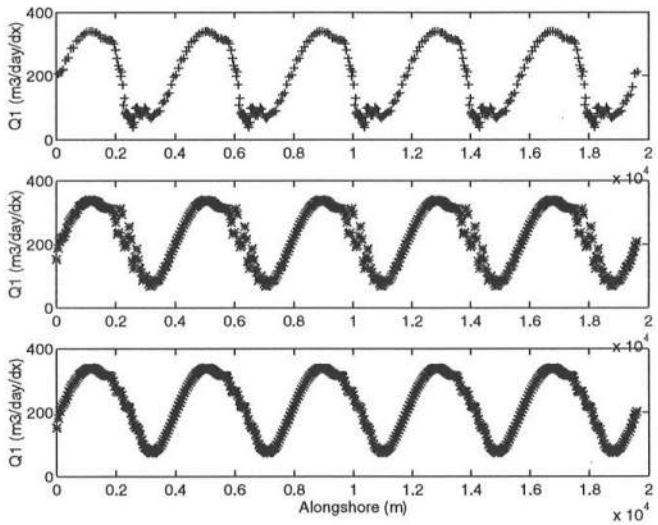

Figure 4.65: Approximation of longshore transport at y_1 contour for incident wave angle 30^o on the mild slope ($A = 0.01$) at t=400 days. Upper, raw data; middle, after bin method; lower, final result after filtering (Periodic Beach ; Case 4)

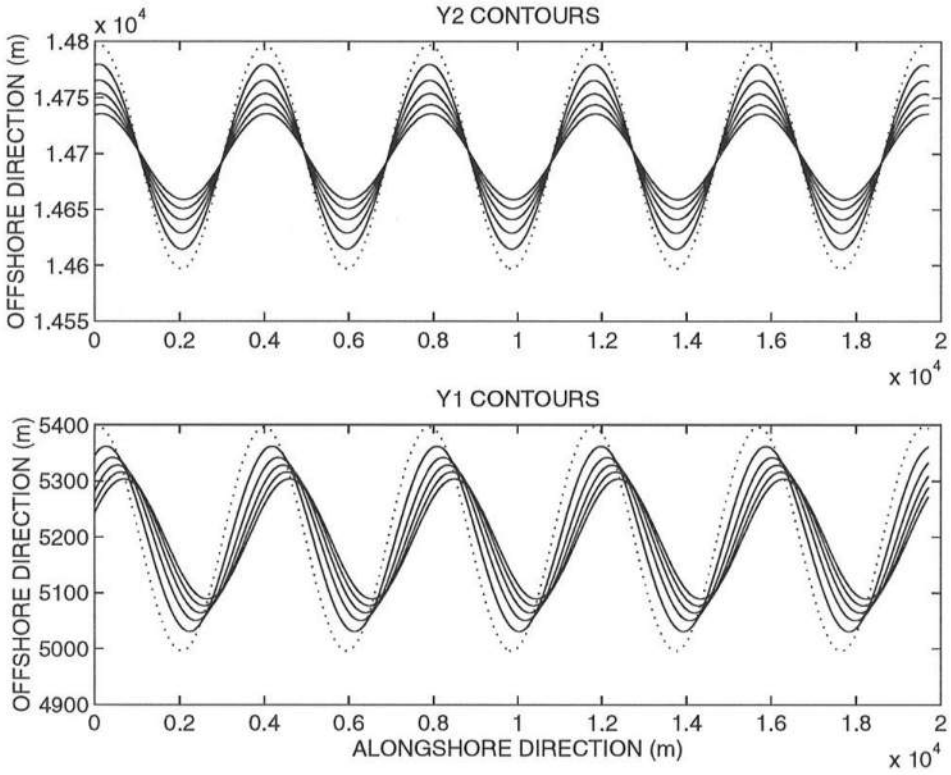

Figure 4.66: Evolution of y_1 and y_2 contours for incident wave angle 30^o on the mild slope ($A = 0.01$) at t=400, 800, 1200, 1600 and 2000 days. Solid line, linear model; dotted line, initial contour (Periodic Beach ; Case 4).

Figures 4.67 to 4.74 show the results from case 5. In this case, the offshore depth, $D_2 = 3\,m$, the sediment scale parameter, $A = 0.01$, were fixed and the breaking wave height, $H_b = 0.3\,m$, was used. The sensitivity analyses for the phase shift between two contours were made. Here, the phase shift was difined as the longshore distance between the crest of the y_1 and the y_2 contours. It can be expressed by using the phase of periodic waves, which describes the y_1 and the y_2 contours. For instance, if two contours are in phase, the distance between two crests are zero, and the phase shift is 0^o. In this study, the y_1 contour was shifted from the y_2 contour in the upwave direction 0^o, 90^o, 120^o, and 180^o. For the cross-shore transport coefficient in the linear model, $C_y = 0.0001\,m/day$ was used in this case. Here are some interesting phenomena. In the linear model, $\Delta\phi = 0^o$ gives the relatively fast migration to the downwave side, and $\Delta\phi = 180^o$ gives the relatively fast migration to the upwave side. Results from $\Delta\phi = 90^o$ and $\Delta\phi = 120^o$ show very small migration to the downwave and upwave side, respectively. Also, these waves decay much rapidly than those from $\Delta\phi = 0^o$ and $\Delta\phi = 180^o$. As for the nonlinear model, results showed opposite phenomena. $\Delta\phi = 0^o$ gives some kind of migration to the upwave side, and $\Delta\phi = 180^o$ creates antisymmetric contours which can be described as moving to the downwave side. Results from $\Delta\phi = 90^o$ and $\Delta\phi = 120^o$ show very small migration with slow decay. Further computation would be needed to confirm the following phenomena, however, for the nonlinear model, the results will become noisy because of its boundary effects. Figure 4.75 shows the example of the results after the long computation such as 1000 time steps. In addition, the number of waves in the computational domain has been changed in order to confirm if it affect the results. As a result, it did not affect the trend of the results.

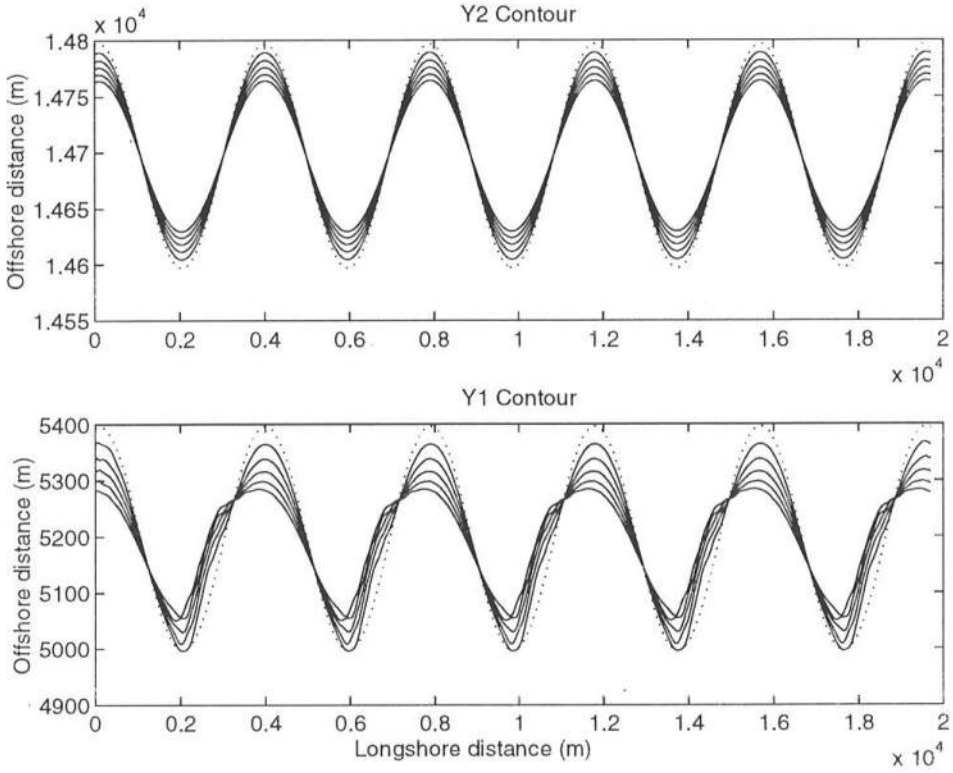

Figure 4.67: Evolution of y_1 and y_2 contours for the phase shift 0^o on the mild slope ($A = 0.01$) at t=400, 800, 1200, 1600 and 2000 days. Solid line, nonlinear model; dotted line, initial contour (Periodic Beach ; Case 5).

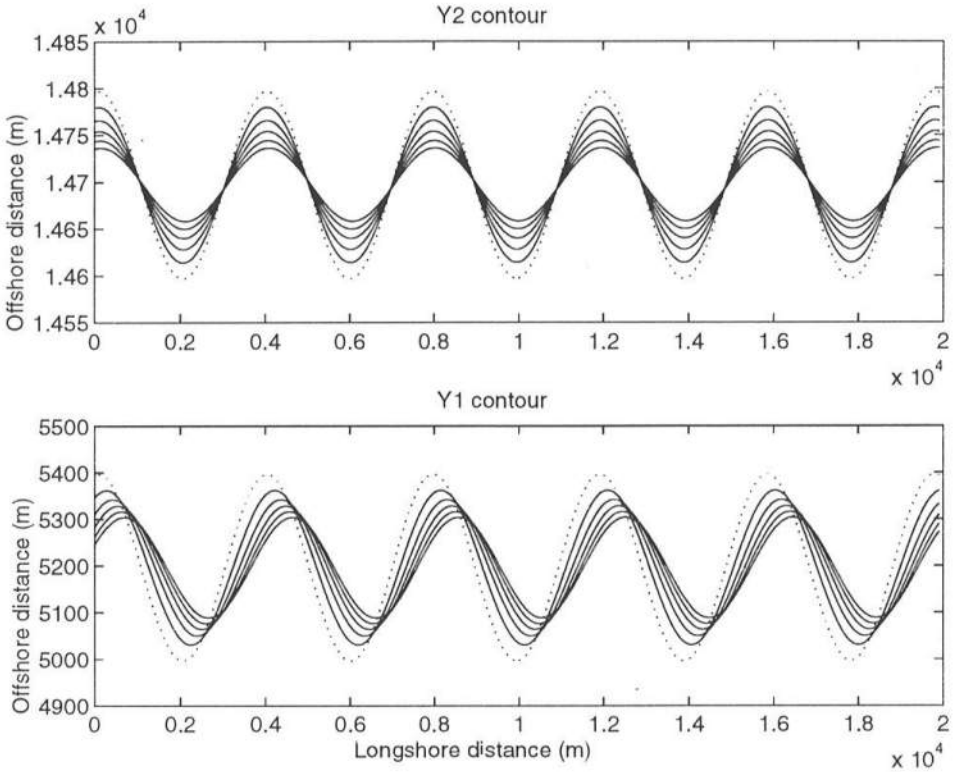

Figure 4.68: Evolution of y_1 and y_2 contours for the phase shift 0^o on the mild slope ($A = 0.01$) at t=400, 800, 1200, 1600 and 2000 days. Solid line, linear model; dotted line, initial contour (Periodic Beach ; Case 5).

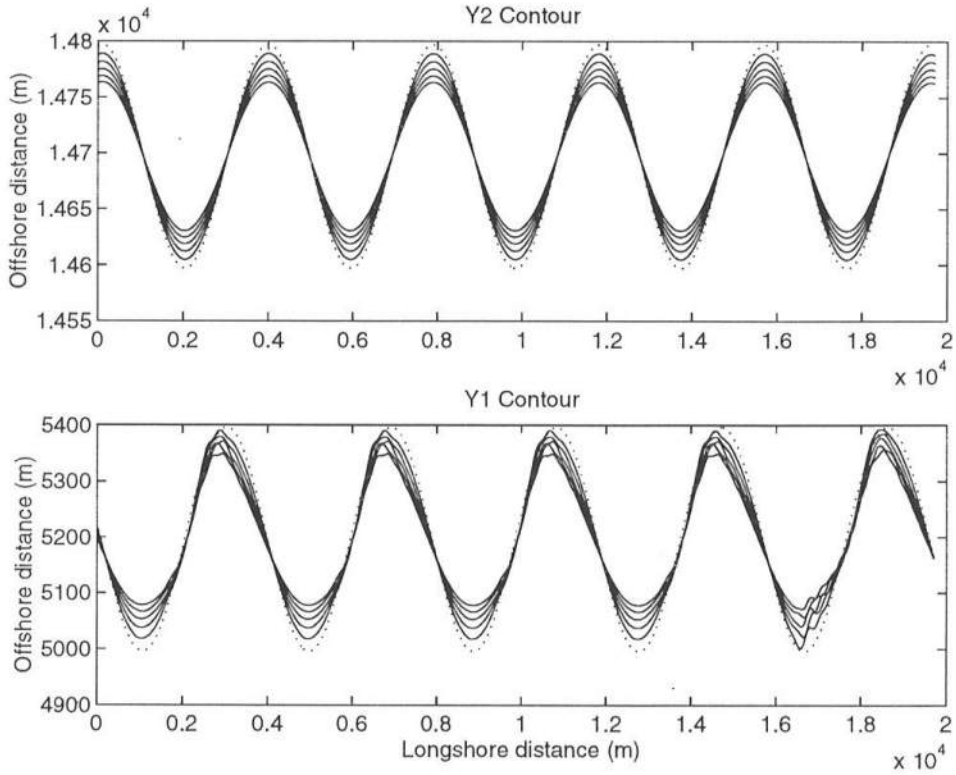

Figure 4.69: Evolution of y_1 and y_2 contours for the phase shift 90^o on the mild slope ($A = 0.01$) at t=400, 800, 1200, 1600 and 2000 days. Solid line, nonlinear model; dotted line, initial contour (Periodic Beach ; Case 5).

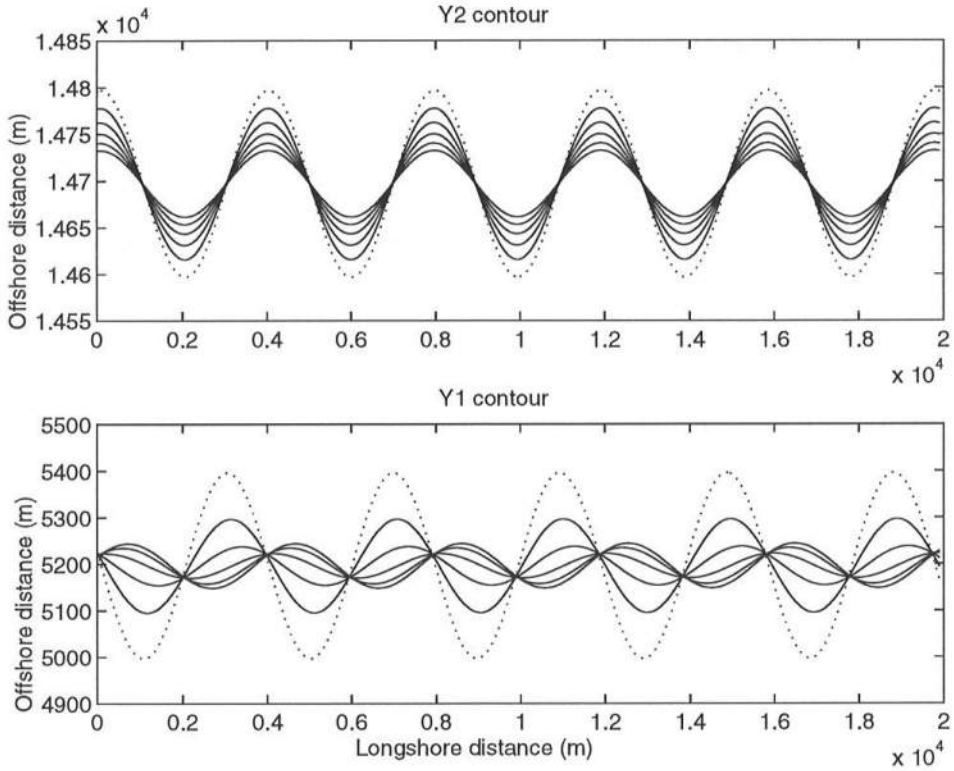

Figure 4.70: Evolution of y_1 and y_2 contours for the phase shift 90^o on the mild slope ($A = 0.01$) at t=400, 800, 1200, 1600 and 2000 days. Solid line, linear model; dotted line, initial contour (Periodic Beach ; Case 5).

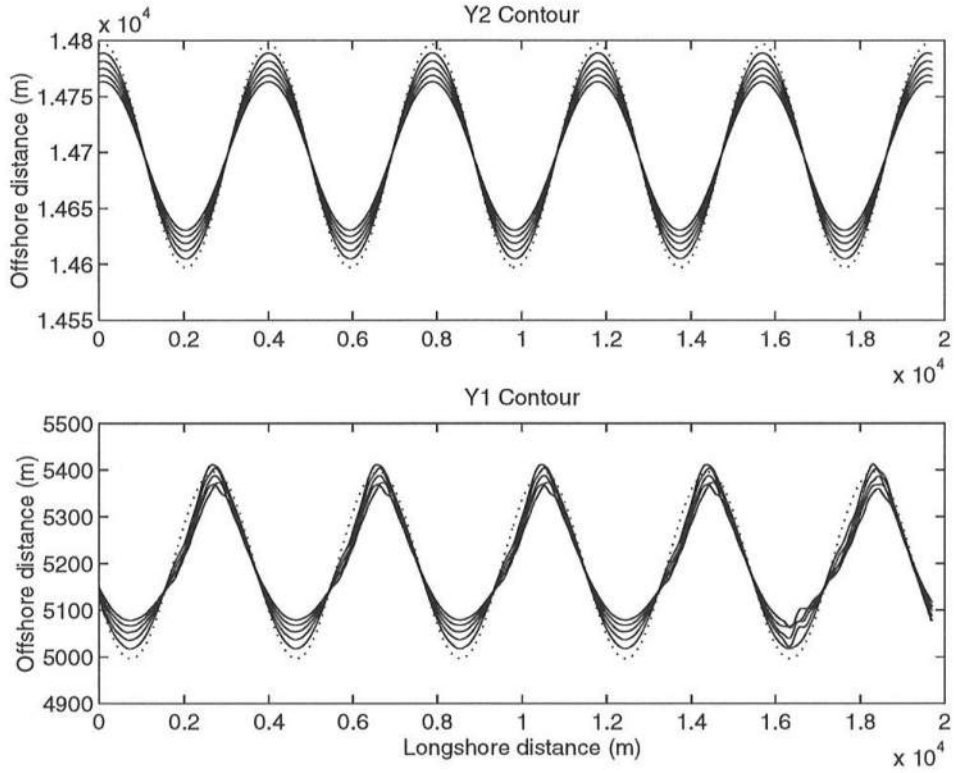

Figure 4.71: Evolution of y_1 and y_2 contours for the phase shift 120^o on the mild slope ($A = 0.01$) at t=400, 800, 1200, 1600 and 2000 days. Solid line, nonlinear model; dotted line, initial contour (Periodic Beach ; Case 5).

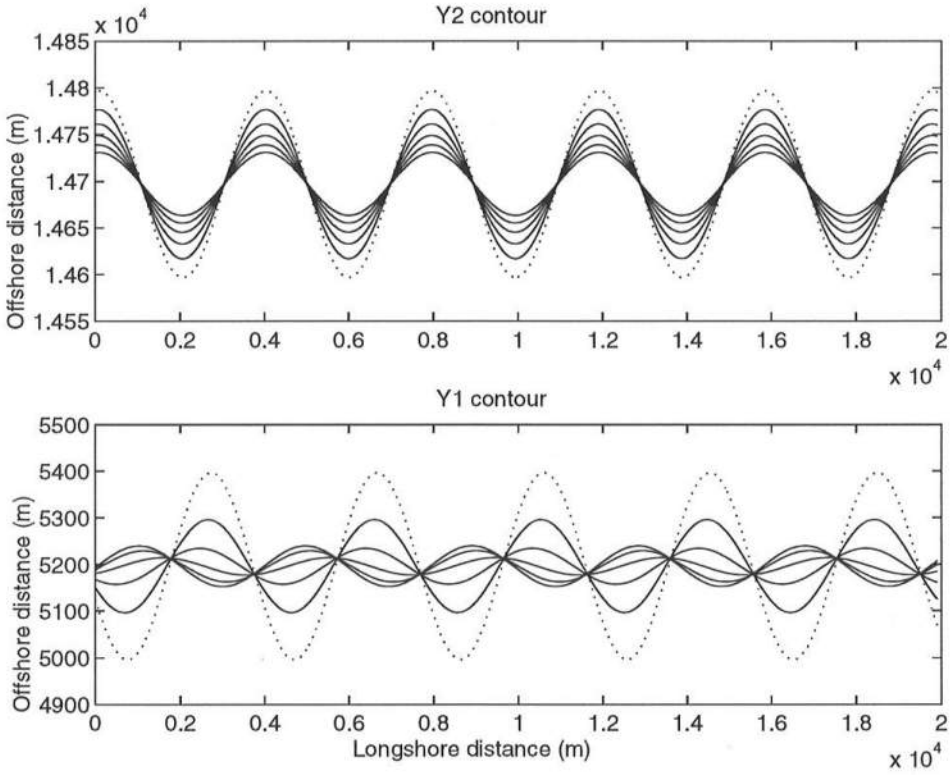

Figure 4.72: Evolution of y_1 and y_2 contours for the phase shift 120^o on the mild slope ($A = 0.01$) at t=400, 800, 1200, 1600 and 2000 days. Solid line, linear model; dotted line, initial contour (Periodic Beach ; Case 5).

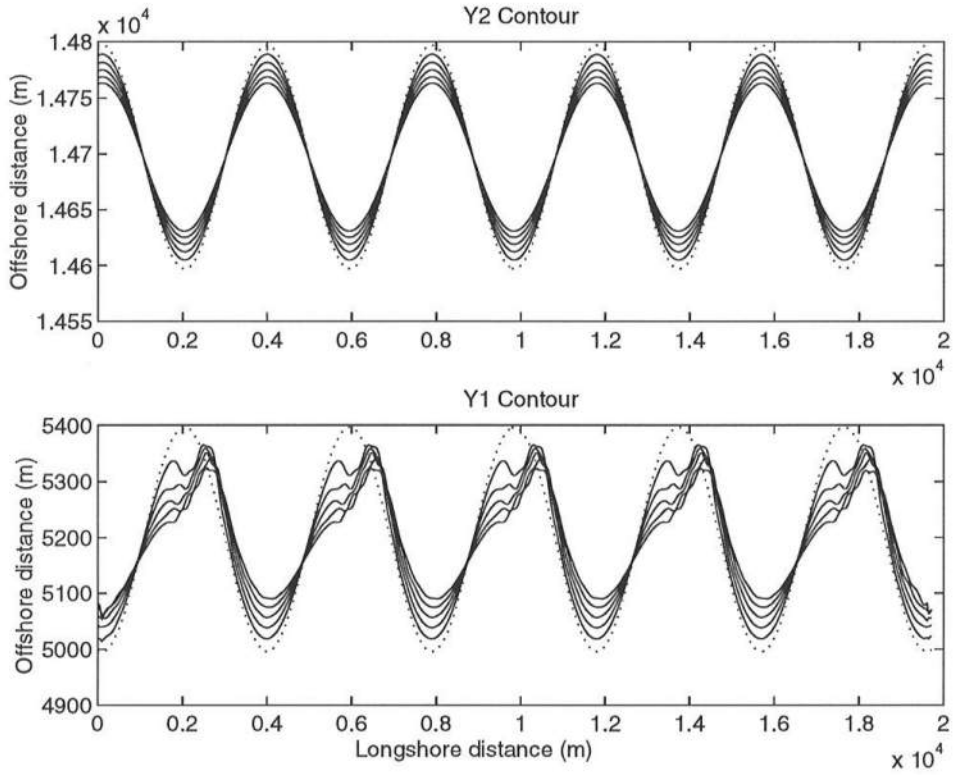

Figure 4.73: Evolution of y_1 and y_2 contours for the phase shift 180^o on the mild slope ($A = 0.01$) at t=400, 800, 1200, 1600 and 2000 days. Solid line, nonlinear model; dotted line, initial contour (Periodic Beach ; Case 5).

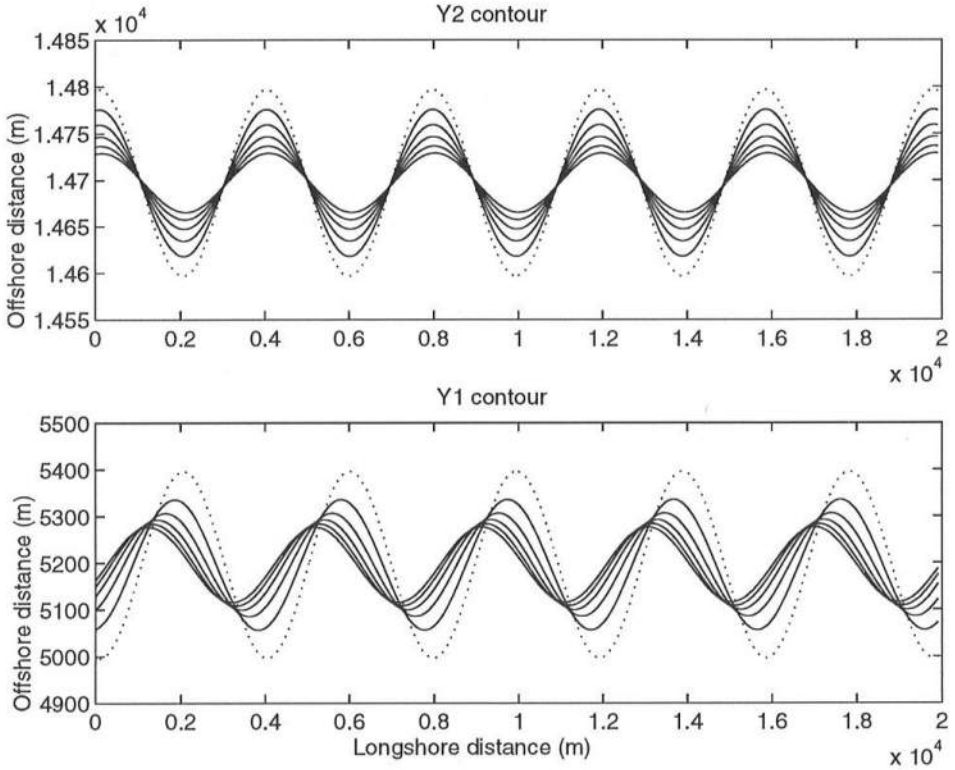

Figure 4.74: Evolution of y_1 and y_2 contours for the phase shift 180^o on the mild slope ($A = 0.01$) at t=400, 800, 1200, 1600 and 2000 days. Solid line, linear model; dotted line, initial contour (Periodic Beach ; Case 5).

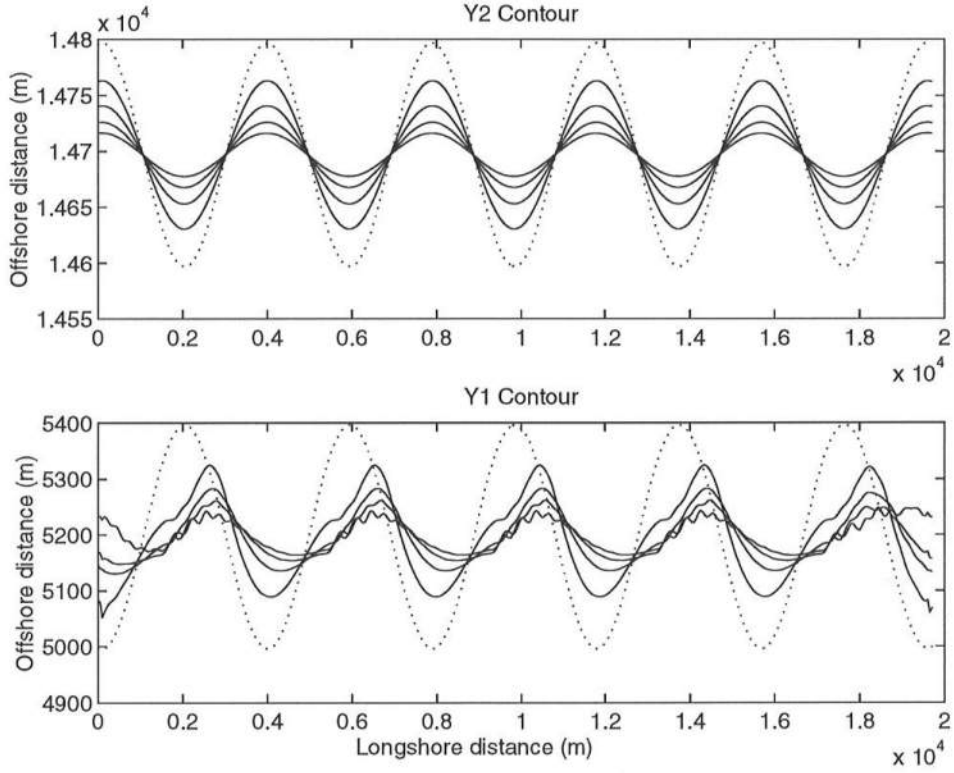

Figure 4.75: Evolution of y_1 and y_2 contours for the phase shift 180^o on the mild slope ($A = 0.01$) at t=2000, 4000, 6000, and 8000 days. Solid line, nonlinear model; dotted line, initial contour (Periodic Beach ; Case 5).

4.2.5 Field Data

Grove, Sonu and Dykstra (1987) observed the migration of a sand hump on the smooth coastline at San Onofre, California. They took surveys of the profiles at discrete survey points (denoted s-1, s-2, s-3, s-4, s-5, and s-6) for two years following the removal of the front pad of the land fill for the San Onofre Nuclear Generating Station in December 1984. They described the sand hump migration as downcoast with an extremely slow speed and a rapid decay. Figure 4.76 shows the survey results at the site. The initial volume of sand for the land fill was approximately 150,000 m^3. The initial shape of the land fill had about 300 m longshore length and 60 m width from the previously existing shoreline. According to their survey, the sediment scale parameter A at background beach was approximately 0.09. In spite of lack of data, one may simulate the shoreline change and the profile change assuming other parameters. Let's assume a plane beach with the uniform slope starting from the 30 m seaward from previous shoreline, the berm height was 3.5 m. Ignoring sand smoothed out to both side of the landfill by bulldozers and considering the conservation of the volume of sand, this slope will intersect with the background profile at 150 m from the shoreline, and its depth will be 2.5 m. Finally, adding appropriate taper to both sides, one may get the trapezoidal beach fill type initial contours. Rgarding the other parameters, it was assumed that the breaking wave height was 0.3 m, the incident wave angle at offshore with respect to the y axis was 30^o, the wave period was 10 sec, the spatial grid was 10 m, and computational time step was 0.1 days. Figure 4.77 shows results from the linear model and the nonlinear model after 60 days. The inshore depth D_1 was taken as 1.0 m, and the offshore depth D_2 was 1.5 m. The cross-shore transport coefficient C_y for the linear model was 1.19 m/day. Since the offshore contour was straight, initially there was no refraction effect. Both model gave similar results and these did not show any migration.

By changing the inshore depth D_1 and plotting contour positions after 60 days at specific point (s-1, s-4 and s-5), one can obtain Figure 4.78. The points s-1, s-4 and s-5 are located at 3000 m, 4250 m, and 5000 m, respectively, in Figure 4.77. Results shows small accretion at s-1, and s-4 and s-5 seemed to stay in the background profile. One can compare this results by looking at the survey results in Figure 4.76. At s-1, the survey result showed the significant shoreline proceeding, approximately 20 m at the mean water level in about 60 days, which is between survey number 1 and 2, meanwhile, the numerical results showed much smaller proceeding, about 10 m at depth 0.2 m. Also, the survey showed smaller accretion at s-4 approximately 20 months behind s-1. However, the numerical result did not showed this phenomenon. As a result, the numerical model could not explain the results from field data, although the data for this analysis was not sufficient.

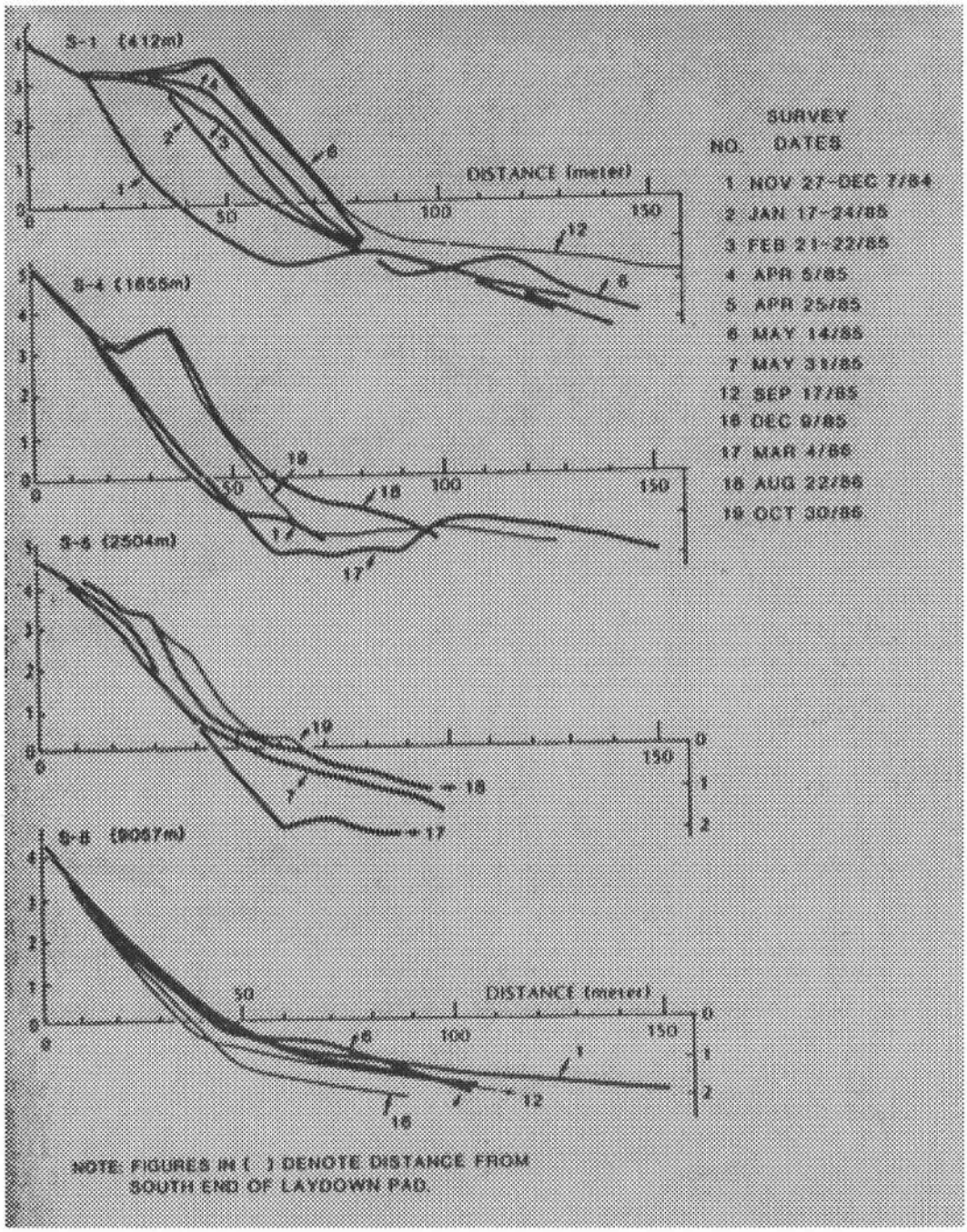

Figure 4.76: Survey results at the site

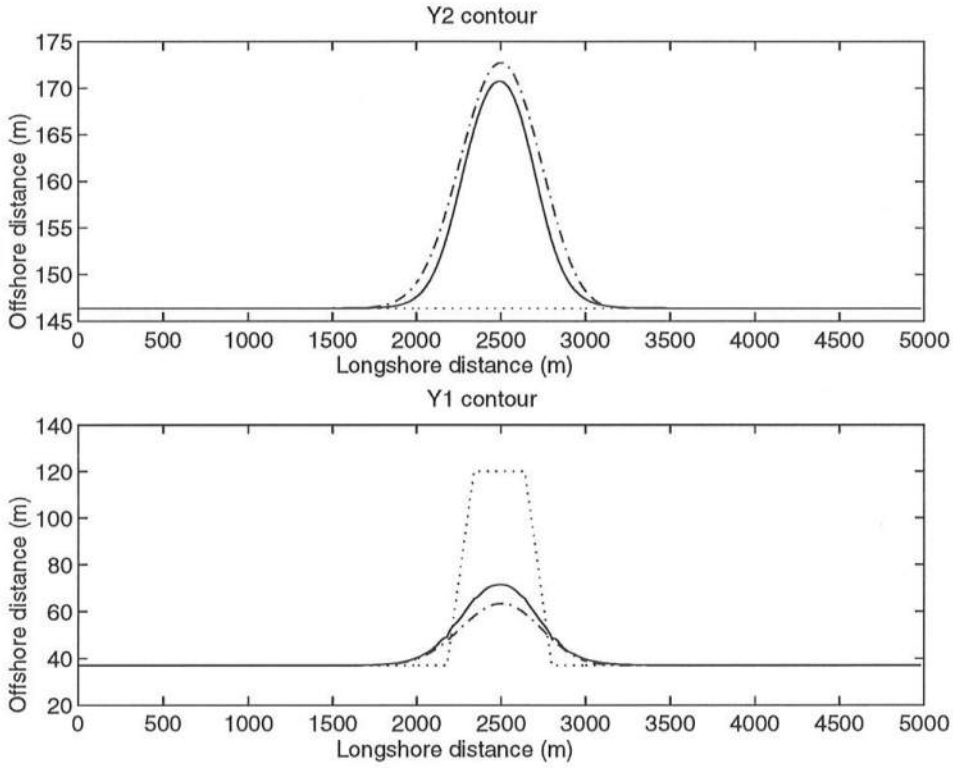

Figure 4.77: Predicted y_1 and y_2 contours at t=60 days. Solid line, nonlinear model; dashed-dotted line, linear model; dotted line, initial contour.

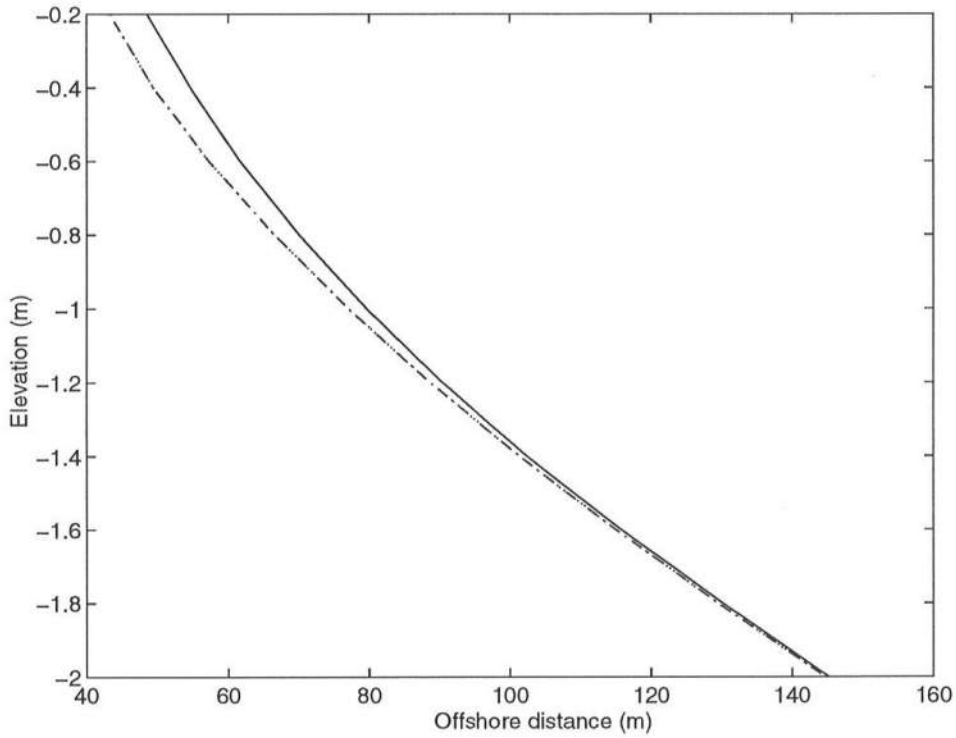

Figure 4.78: Profiles after 60 days. Solid line, s-1 (412 m); Dotted line, s-4 (1655 m); Dash-dotted line, s-5 (2504 m).

Chapter 5

CONCLUSIONS

5.1 Conclusions

The nonlinear two-line shoreline model with refraction was developed after the linear version introduced by Dalrymple (1997). The both models were based on the concept of the two-line model developed by Bakker (1968b). Several examples of the migration of sand waves have been observed in the field. However, existing contour models such as the one-line model and Bakker's two-line model were not able to provide satisfactory explanations for this phenomenon. The two-line model with refraction is expected to explain the physical mechanism behind these migrations of sand waves.

The governing equations of the two-line model with refraction were two mass conservation equations at the inshore and the offshore. These equations included longshore transport at the inshore and the offshore contours, and cross-shore transport. As in Bakker's two-line model, cross-shore transport played a role in coupling together these two equations. As for the cross-shore transport, the nonlinear model used an expression based on the difference between the actual energy dissipation rate and that for an equilibrium profile, which was first proposed by Moore (1982), while the linear model used the same expression as Bakker (1968b). The refraction effect showed up in the longshore transport terms

which were functions of the incident wave angles with respect to the shoreline normal. Also, it leads the spatial lag into the spatial argument of those incident wave angles. This is another relationship between two equations.

The finite difference scheme used for the nonlinear model was based on a forward-difference in time and the centered-difference in space. In order to carry out these computations, two extra points at both ends on each contour were needed. For determination of these points, two types of boundary conditions were used: fixed boundary and periodic boundary.

In the nonlinear model, the focusing effect was also considered under assumption of the straight wave rays from the offshore to the inshore contour. To include the focusing effect, the "bin method" was invented. For the bin size, the spatial grid size dx was specified by considering the computational resolution and the time consumption of the computation. It was found that signals after using the "bin method" tended to have some noise which should not have been there because the size of the noise was smaller than the wavelength of the water waves. Moreover, practically, wave crests would be expected to be smoothed out due to wave diffraction. To remove this noise, a numerical filtering technique, the five point Shapiro Filtering, was applied to the raw longshore transport data. That filtering was able to remove only high frequency noise components so that the signal could still retain most of the information of the original signal after filtering repetitions. After using these scheme, the model produced relatively smooth contours.

In order to verify the numerical results, extensive laboratory experiments were performed in a spiral wave basin. Two sets of surveys were conducted with different initial shapes of the contours: a single beach fill and three beach fills. Each set included surveys at t=0, 3, 10, and 20 minutes. Prior to these main

surveys, measurements of the rate of longshore transport were made by using the single groin method. It was found that the longshore transport coefficient $\mathcal{K}$ was approximately 1.01. Water wave measurements were made by using two wave gauges. It was determined that the wave period was 0.98 second and the wave angle with respect to the radial axis was 13.3 degree at 0.95 m from the center of the basin. The sediment scale parameter, A, was determined to be 0.1 by applying the two-thirds power law to all profiles in the test area in their equilibrium state.

Verification of the numerical results was performed by comparing results from both the nonlinear and the linear model with experimental data. Also, several other simulations were made for the numerical model using various input conditions. Comparisons between numerical results and experimental data were relatively good, although the linear model results showed faster decay than the experimental data in three beach fills case. Two kinds of inshore depth were used for the comparison, and the case of shallower depth showed better agreement.

Despite relatively good agreement with experimental data, it was not sufficient to explain migrations of sand waves because the experimental results themselves did not show any migration. In attempt to resolve this inconsistency, several sensitivity analyses were performed. In the first analysis, solitary wave-shaped contours were used for initial conditions, and the wave angle with respect to the y axis was varied with regular slope ($A = 0.1$), and mild slope ($A = 0.01$). In this analysis, the linear model showed some migration on the mild slope beach with large angles, while the nonlinear model did not show any migration, instead it showed remarkable focusing effects with the hot spot located downwave of the solitary wave shaped contour. In the second analysis, trapezoidal beach fills were used for the initial contours. In this case, two kinds of wave angles, beach slopes, and offshore depths were used. It was found that a wave angle of 0^o might be able

to extend the lifetime of the fill due to the focusing effect. It can be concluded that a shallow offshore depth definitely will reduce the focusing effect because the rays will not be able to concentrate enough over the short distance between two contours. In the third analysis, periodic contours were used with two kinds of beach slopes and offshore depths. The wave angle in this test was fixed at 30^o. As in the solitary wave case, the linear model showed some migrations on the mild slope beach; on the other hand, the nonlinear model rather generate antisymmetric shape by focusing effect.

Sensitivity analyses about the phase shift $\Delta\phi$ between the two initial contours were made. Results showed some interesting phenomena. For the linear model, the result from $\Delta\phi = 0^o$ shows the strong migration to the downwave side, and that from $\Delta\phi = 180^o$ shows the strong migration to the upwave side. Also, the results from $\Delta\phi = 90^o$ and $\Delta\phi = 120^o$ show the very little migration with extremely rapid decay to the downwave and upwave sides, respectively. Alternatively, the nonlinear model provides opposite results. It was unclear if the antisymmetric shape contours of the nonlinear results can be called as the migration of sand waves. As stated in the previous case, results strongly depend on geometry such as the offshore depth and the beach slope.

Finally, numerical results were applied to field observation data, which was the migration of a sand hump on the smooth coastline at San Onofre, California. Both the nonlinear and the linear model could not explain the observed data, although the data for input were not sufficient.

5.2 Suggestions for Future Work

First of all, further experiments will be needed in order to verify some of the numerical results that indicated sand wave migration. For instance, wave

refraction effects should be examined using larger scale geometry with very mild slope beach profiles and larger offshore wave angles. This is very important because there is not enough field data for migrating sand waves. Even though there is significant evidence for migration, information such as wave data and survey data have not been sufficient.

As for the nonlinear numerical model, there are still more possibility to improve both the water wave and the sediment transport problem. For example, assumption of the straight wave rays clearly induces errors under a large spacing of contours. Also the wave diffraction effect should be considered to produce more realistic wave rays. Since the present model depends on numerical filtering to reduce the noise caused by the bin method, a more physically reasonable scheme should be developed. For the numerical scheme itself, one could use a more sophisticated numerical technique, such as the Crank-Nicolson method, to carry out more accurate computations. Also, better boundary conditions for constant longshore transport should be developed as replacement for the fixed boundary used in the present model to express constant sand supply. If there is no cross-shore transport at the boundary, the present boundary conditions work well; however, in the presence of significant cross-shore transport, the present method was not sufficient.

Finally, in this report, the nonlinear two-line shoreline model with refraction could not explain the migrating sand waves, whereas the linear model showed some kind of migration. However, it should be mentioned here that the angle used for the linear model, which induced migration, was not small angle. This violates the assumption of small angle for the linear model.

REFERENCES

Bakker, W.T. (1968a), "Mathematical Theory About Sand Waves and its Application on the Dutch Wadden Isle of Vlieland," *Shore and Beach*, v. 36, n. 2, pp 5-14.

Bakker, W.T. (1968b), "The Dynamics of a Coast with a Groyne System," *Proc. 11th Intl. Conf. Coastal Engrg.*, London, pp 492-517.

Bendat, J.S. and A.G. Piersol, (1986), **Random Data, Analysis and Measurement Procedures**, New York, John Wiley and Sons, Inc.

Brunn, P. (1954), "Migrating Sand Waves or Sand Humps, with Special Reference to Investigations Carried Out on the Danish North Coast Sea," *Proc. 5th Coastal Engrg. Conf.*, New York, pp 531-538.

Dalrymple, R.A. and R.G. Dean, (1972), "The Spiral Wavemaker for Littoral Drift Studies," *Proc. 13th Intl. Conf. Coastal Engrg.*, ASCE, 1, pp 689-705.

Dean, R.G., (1977), "Equilibrium Beach Profiles: U.S. Atlantic and Gulf Coasts," *Department of Civil Engineering , Ocean Engineering Report No.12*, University of Delaware.

Dean, R.G. and R.A. Dalrymple, (1984), **Water Wave Mechanics for Engineers and Scientists**, New York, World Scientific.

Dean, R.G. and R.A. Dalrymple, (1997), **Coastal Processes with Engineering Applications**, (manuscript).

Dalrymple, R.A. (1997a), "Refraction and Two-line Models of Shoreline Change," *Proc. 10th Natl. Conf. on Beach Preservation Technology*, Florida Shore and Beach Preservation Association, St. Petersburg, pp 167-182.

De Boor, C., (1978), **A Practical Guide to Spiles**, New York, Springer-Verlag New York Inc.

Gerald, C.F., (1978), **Applied Numerical Analysis Second Edition**, Menlo Park, CA, Addison-Wesley Publishing Company.

Goda, Y., (1985), **Random Seas and Design of Maritime Structures**, University of Tokyo Press, Japan.

Grove, R.S., C.J. Sonu, and D.H. Dykstra, (1987), "Fate of Massive Sediment Injection on a Smooth Shoreline at San Onfore, California," *Proc. Coastal Sediments.*, ASCE, New york, pp 531-538.

Hoffman, J.D., (1992), **Numerical Methods for Engineers and Scientists**, New York, McGraw-Hill, Inc.

Hulsbergen, C.H., W.T. Bakker and G. Van Bochove, (1976), "Experimental Verification of Groyne Theory," *Proc. 15th Intl. Conf. Coastal Engrg.*, ASCE, Honolulu, pp 1439-1458.

Inman, D.L., (1987), "Accretion and Erosion Waves on Beaches," *Shore Beach*, v. 55, pp 61-66.

Komar, P.D. and D.L. Inman, (1970), "Longshore Sand Transport on Beaches," *J. Geophys.*, v. 75, n. 30, pp 5914-5927.

Kraus, N.C., M. Isobe, H. Igarashi, T.O. Sasaki and K. Horikawa, (1980), "Field Experiments on Longshore Sand Transport in the Surf Zone," *Proc. 18th Intl. Conf. Coastal Engrg.*, ASCE, Cape Town, pp 969-988.

Kriebel, D.L., (1983), "Beach and Dune Response to Hurricanes," MCE Thesis, University of Delaware, 163 pp.

Kriebel, D.L. and R.G. Dean, (1985), "Numerical Simulation of Time-dependent Beach and Dune Erosion," *Coastal Engrg.*, v. 9, n. 3, pp 221-245.

Mei, C.C., (1973), "Shoaling of Spiral Waves in a Circular Basin," *Journal of Geophysical Research*, v. 78, n. 6, pp 977-980.

Mei, C.C., (1983), **The Applied Dynamics of Ocean Surface Waves**, New York, World Scientific.

Moore, D.L., (1982), "Beach Profile Evolution in Response to Changes in Water Level and Wave Height," MCE Thesis, University of Delaware, 135 pp.

Pelnard-Considere, R., (1956), "Essai de theorie de l'evolution des forms de rivage en plages de sable et de galets," *Quatriemes Journees de l'Hydraulique, Les Energies de la Mer*, Question [III], Report 1, v. 1, pp 289-298.

Shapiro, R., (1970), "Smoothing, Filtering, and Boundary Effects," *Rivews of Geophysics and Space Physics*, v. 8, n. 2, pp 359-387.

Shu, K.D., (1986), "Modeling of Beach Erosion Control Measures in a Spiral Wave Basin," MCE Thesis, University of Delaware, pp 4-34.

Thevenot, M.M. and N.C. Kraus, (1995), "Longshore Sand Waves at Southampton Beach, New York: Observation and Numerical Simulation of their Movement," *Marine Geology*, v. 126, pp 249-269.

Verhagen, H.J., (1989), "Sand Waves Along the Dutch Coast," *Coastal Engineering*, v. 13, pp 129-147.